

10 World-line and Determinantal Quantum Monte Carlo Methods for Spins, Phonons and Electrons

F.F. Assaad¹ and H.G. Evertz²

¹ Institut für Theoretische Physik und Astrophysik, Universität Würzburg, 97074 Würzburg, Germany

² Institut für Theoretische Physik und Computational Physics, Technische Universität Graz, A-8010 Graz, Austria

In this chapter we will concentrate primarily on world-line methods with loop updates, for spins and also for spin-phonon systems, as well as on the auxiliary field quantum Monte Carlo (QMC) method. Both approaches are based on a path integral formulation of the partition function which maps a d -dimensional quantum system onto a $d + 1$ dimensional classical system. The additional dimension is nothing but the imaginary time. World-line based approaches for quantum spin systems offer a simple realization of the mapping from quantum to classical, and serve as a nice introduction to QMC methods for correlated systems. Auxiliary field QMC methods provide access to fermionic systems both at finite temperature and in the ground state. An important example is the Hirsch-Fye approach that allows for an efficient simulation of impurity models, such as the Kondo and Anderson models, and is widely used in the domain of dynamical mean field theories (DMFT).

10.1 Introduction

The correlated electron problem remains one of the central challenges in solid state physics. Given the complexity of the problem, numerical simulations provide an essential source of information to test ideas and develop intuition. In particular for a given model describing a particular material we would ultimately like to be able to carry out efficient numerical simulations so as to provide *exact* results on thermodynamic, dynamical, transport and ground-state properties. If the model shows a continuous quantum phase transition we would like to characterize it by computing the critical exponents. Without restriction on the type of model, this is an extremely challenging goal.

There are however a set of problems for which numerical techniques have provided invaluable insight and will continue to do so. Here we list a few which are exact, capable of reaching large system sizes (the computational effort scales as a power of the volume), and provide ground-state, dynamical as well as thermodynamic quantities: (i) Density matrix renormalization group applied to general one-dimensional (1D) systems [1, 2], (ii) world-line based QMC methods such as the loop algorithm [3, 4] or directed loops [5] applied to non-frustrated spin systems in arbitrary dimensions or to 1D electron-models on bipartite lattices, and (iii) auxiliary field QMC methods [6]. The latter method is capable of handling a class of

models with spin and charge degrees of freedom in dimensions larger than unity. This class contains fermionic lattice models with attractive interactions (e.g. attractive Hubbard model), models invariant under particle-hole transformation, as well as impurity problems modelled by Kondo or Anderson Hamiltonians.

In this lecture we first introduce the world-line approach, exemplarily for the 1D XXZ-chain, see Sect. 10.2. In Sect. 10.3, we discuss world-line representations of $\exp(-\beta H)$ without Trotter-time discretization errors (where $\beta = 1/(k_B T)$), including the stochastic series expansion (SSE). We emphasize that the issue of such a representation of $\exp(-\beta H)$ is largely independent of the Monte Carlo algorithm used to update the world lines. In Sect. 10.4 we explain the loop algorithm from an operator point of view, and discuss some applications and generalizations. Sect. 10.5 discusses ways to treat coupled systems of spins and phonons, exemplified for 1D spin-Peierls transitions. It includes a new method which allows the simulation of arbitrary bare phonon dispersions [7]. In Sect. 10.6 we describe the basic formulation of the auxiliary field QMC method. This includes the formulation of the partition function, the measurement of equal-time and time-displaced correlation functions as well as general conditions under which one can show the absence of negative sign problem. In Sect. 10.7 we concentrate on the implementation of the auxiliary field method for lattice problems. Here, the emphasis is placed on numerical stabilization of the algorithm. Sect. 10.8 concentrates on the Hirsch-Fye formulation of the algorithm. This formulation is appropriate for general impurity models, and is extensively used in the framework of dynamical mean-field theories and their generalization to cluster methods. Recently, more efficient continuous time algorithms for the impurity problem (diagrammatic determinantal QMC methods) have been introduced [8, 9]. Finally in Sect. 10.9 we briefly provide a short and necessarily biased overview of applications of auxiliary field methods.

10.2 Discrete Imaginary Time World Lines for the XXZ Spin Chain

The attractive feature of the world-line approach [10] is its simplicity. Here, we will concentrate on the 1D XXZ spin chain. The algorithm relies on a mapping of the 1D XXZ quantum spin chain to the six vertex model [11]. The classical model may then be solved exactly as in the case of the six vertex model [12] or simulated very efficiently by means of cluster Monte Carlo methods [3, 4]. The latter approach has proved to be extremely efficient for the investigation of non-frustrated quantum spin systems [13] in arbitrary dimensions. The efficiency lies in the fact that (i) the computational time scales as the volume of the classical system so that very large system sizes may be achieved, and (ii) the autocorrelation times are small.

A related method, applicable to more models, are directed loops [5, 14]. A short introduction is provided in [15]. For a general short overview of advanced world-line QMC methods see [16]. Longer reviews are provided in [4, 17].

Fermions can also be represented by world lines. For spinless fermions in any dimension the same representation as for the XXZ spin model results, albeit with

AU: We have shortened the Running head please check is this ok.

additional signs corresponding to the exchange of fermions. The world-line approach will allow us to acquire some insight into the resulting sign problem. This is a major open issue in QMC methods applied to correlated systems. When it occurs the computational effort scales exponentially with system size and inverse temperature. Recent attempts in the form of novel concepts to tackle correlated electron systems are reviewed in [18, 19].

Finally, at the end of this section, we will discuss extensions of the world-line approach to tackle the problem of the dynamics of a single-hole in non-frustrated quantum magnets.

10.2.1 Basic Formulation

To illustrate the world-line QMC method, we concentrate on the XXZ quantum spin chain. This model is defined as

$$H = J_x \sum_i (S_i^x S_{i+1}^x + S_i^y S_{i+1}^y) + J_z \sum_i S_i^z S_{i+1}^z, \quad (10.1)$$

where S_i are spin 1/2 operators on site i and hence satisfy the commutation rules

$$[S_i^\eta, S_j^\nu] = i\epsilon^{\eta,\nu,\gamma} S_i^\gamma \delta_{i,j}. \quad (10.2)$$

In the above, $\epsilon^{\eta,\nu,\gamma}$ is the antisymmetric tensor and the sum over repeated indices is understood. We impose periodic boundary conditions

$$S_{i+L} = S_i, \quad (10.3)$$

where L denotes the length of the chain.

A representation of the above commutation relations is achieved with the Pauli spin matrices. For a single spin-1/2 degree of freedom, we can set

$$S^x = \frac{1}{2} \begin{pmatrix} 0 & 1 \\ 1 & 0 \end{pmatrix}, \quad S^y = \frac{1}{2} \begin{pmatrix} 0 & -i \\ i & 0 \end{pmatrix}, \quad S^z = \frac{1}{2} \begin{pmatrix} 1 & 0 \\ 0 & -1 \end{pmatrix}, \quad (10.4)$$

and the corresponding Hilbert space $\mathcal{H}_{1/2}$ is spanned by the two state vectors

$$|\uparrow\rangle = \begin{pmatrix} 1 \\ 0 \end{pmatrix}, \quad |\downarrow\rangle = \begin{pmatrix} 0 \\ 1 \end{pmatrix}. \quad (10.5)$$

It is convenient to define the raising S^+ and lowering S^- operators

$$S^+ = S^x + iS^y, \quad S^- = S^x - iS^y, \quad (10.6)$$

such that

$$\begin{aligned} S^- |\downarrow\rangle &= S^+ |\uparrow\rangle = 0, \\ S^- |\uparrow\rangle &= |\downarrow\rangle, \\ S^+ |\downarrow\rangle &= |\uparrow\rangle. \end{aligned} \quad (10.7)$$

The Hilbert space of the L -site chain \mathcal{H}_L is given by the tensor product of L spin $1/2$ Hilbert spaces. \mathcal{H}_L contains 2^L state vectors which we will denote by

$$|\boldsymbol{\sigma}\rangle = |\sigma_1, \sigma_2, \dots, \sigma_L\rangle \quad (10.8)$$

with $\sigma_i = \uparrow$ or \downarrow . A representation of the unit operator in \mathcal{H}_L is given by

$$1 = \sum_{\boldsymbol{\sigma}} |\boldsymbol{\sigma}\rangle \langle \boldsymbol{\sigma}|. \quad (10.9)$$

We can easily solve the two-site problem

$$\begin{aligned} H_{\text{two sites}} &= J_x \underbrace{(S_1^x S_2^x + S_1^y S_2^y)} + J_z S_1^z S_2^z. \\ &\equiv \frac{1}{2}(S_1^+ S_2^- + S_1^- S_2^+) \end{aligned} \quad (10.10)$$

The eigenstates of the above Hamiltonian are nothing but the singlet and three triplet states

$$\begin{aligned} H_{\text{two sites}} \frac{1}{\sqrt{2}} (|\uparrow, \downarrow\rangle - |\downarrow, \uparrow\rangle) &= \left(-\frac{J_z}{4} - \frac{J_x}{2}\right) \frac{1}{\sqrt{2}} (|\uparrow, \downarrow\rangle - |\downarrow, \uparrow\rangle), \\ H_{\text{two sites}} \frac{1}{\sqrt{2}} (|\uparrow, \downarrow\rangle + |\downarrow, \uparrow\rangle) &= \left(-\frac{J_z}{4} + \frac{J_x}{2}\right) \frac{1}{\sqrt{2}} (|\uparrow, \downarrow\rangle + |\downarrow, \uparrow\rangle), \\ H_{\text{two sites}} |\uparrow, \uparrow\rangle &= \frac{J_z}{4} |\uparrow, \uparrow\rangle, \\ H_{\text{two sites}} |\downarrow, \downarrow\rangle &= \frac{J_z}{4} |\downarrow, \downarrow\rangle. \end{aligned} \quad (10.11)$$

The basic idea of this original world-line approach is to split the XXZ Hamiltonian into a set of independent two-site problems. The way to achieve this decoupling is with the use of a path integral and the Trotter decomposition. First we write

$$H = \underbrace{\sum_n H^{(2n+1)}}_{H_1} + \underbrace{\sum_n H^{(2n+2)}}_{H_2} \quad (10.12)$$

with $H^{(i)} = J_x (S_i^x S_{i+1}^x + S_i^y S_{i+1}^y) + J_z S_i^z S_{i+1}^z$. One may verify that H_1 and H_2 are sums of commuting (i.e. independent) two-site problems. Hence, on their own H_1 and H_2 are trivially solvable problems. However, H is not. To use this fact, we split the imaginary propagation $\exp(-\beta H)$ into successive infinitesimal propagations of H_1 and H_2 . Here β corresponds to the inverse temperature. This is achieved with the Trotter decomposition introduced in detail in Sect. 10.A. The partition function is then given by

$$\begin{aligned} \text{Tr} [e^{-\beta H}] &= \text{Tr} [(e^{-\Delta\tau H})^m] = \text{Tr} [(e^{-\Delta\tau H_1} e^{-\Delta\tau H_2})^m] + \mathcal{O}(\Delta\tau^2) \\ &= \sum_{\boldsymbol{\sigma}_1 \dots \boldsymbol{\sigma}_{2m}} \langle \boldsymbol{\sigma}_1 | e^{-\Delta\tau H_1} | \boldsymbol{\sigma}_{2m} \rangle \dots \langle \boldsymbol{\sigma}_3 | e^{-\Delta\tau H_1} | \boldsymbol{\sigma}_2 \rangle \langle \boldsymbol{\sigma}_2 | e^{-\Delta\tau H_2} | \boldsymbol{\sigma}_1 \rangle + \mathcal{O}(\Delta\tau^2), \end{aligned} \quad (10.13)$$

where $m\Delta\tau = \beta$. In the last equality we have inserted the unit operator between each infinitesimal imaginary time propagation. For each set of states $|\sigma_1\rangle \dots |\sigma_{2m}\rangle$ with non-vanishing contribution to the partition function we have a simple graphical representation in terms of world lines which track the evolution of the spins in space and imaginary time. An example of a world-line configuration is shown in Fig. 10.1.

Hence the partition function may be written as the sum of over all world-line configurations w , each world-line configuration having an appropriate weight $\Omega(w)$

$$Z = \sum_w \Omega(w)$$

$$\Omega(w) = \langle \sigma_1 | e^{-\Delta\tau H_1} | \sigma_{2m} \rangle \dots \langle \sigma_3 | e^{-\Delta\tau H_1} | \sigma_2 \rangle \langle \sigma_2 | e^{-\Delta\tau H_2} | \sigma_1 \rangle, \quad (10.14)$$

where w defines the states $|\sigma_1\rangle \dots |\sigma_{2m}\rangle$.

Our task is now to compute the weight $\Omega(w)$ for a given world-line configuration w . Let us concentrate on the matrix element $\langle \sigma_{\tau+1} | \exp(-\Delta\tau H_2) | \sigma_\tau \rangle$. Since H_2 is a sum of independent two site problems, we have

$$\langle \sigma_{\tau+1} | e^{-\Delta\tau H_2} | \sigma_\tau \rangle = \prod_{i=1}^{L/2} \langle \sigma_{2i,\tau+1}, \sigma_{2i+1,\tau+1} | e^{-\Delta\tau H^{(2i)}} | \sigma_{2i,\tau}, \sigma_{2i+1,\tau} \rangle. \quad (10.15)$$

Hence, the calculation of the weight reduces to solving the two-site problem, see (10.10). We can compute, for example, the spin-flip matrix element

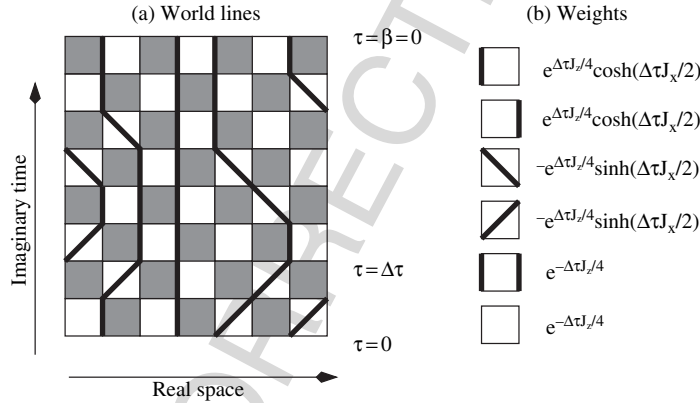


Fig. 10.1. (a) World-line configuration for the XXZ model of (10.1). Here, $m = 4$ and the system size is $L = 8$. The *bold lines* follow the time evolution of the up spins and empty sites, with respect to the world lines, correspond to the down spins. A full time step $\Delta\tau$ corresponds to the propagation with H_1 followed by H_2 . Periodic boundary conditions are chosen in the spatial direction. In the time direction, periodic boundary conditions follow from the fact that we are evaluating a trace. (b) The weights for a given world-line configuration is the product of the weights of plaquettes listed in the figure. Note that, although the spin-flip processes come with a minus sign, the overall weight for the world-line configuration is positive since each world-line configuration contains an even number of spin flips

$$\begin{aligned}
& \langle \downarrow, \uparrow | e^{-\Delta\tau H_{\text{two sites}}} | \uparrow, \downarrow \rangle \\
&= \frac{1}{\sqrt{2}} \langle \downarrow, \uparrow | e^{-\Delta\tau H_{\text{two sites}}} \left(\frac{1}{\sqrt{2}} (|\uparrow, \downarrow\rangle - |\downarrow, \uparrow\rangle) + \frac{1}{\sqrt{2}} (|\uparrow, \downarrow\rangle + |\downarrow, \uparrow\rangle) \right) \\
&= \frac{1}{\sqrt{2}} \langle \downarrow, \uparrow | \left(e^{-\Delta\tau(-J_z/4 - J_x/2)} \frac{1}{\sqrt{2}} (|\uparrow, \downarrow\rangle - |\downarrow, \uparrow\rangle) \right. \\
&\quad \left. + e^{-\Delta\tau(-J_z/4 + J_x/2)} \frac{1}{\sqrt{2}} (|\uparrow, \downarrow\rangle + |\downarrow, \uparrow\rangle) \right) \\
&= -e^{\Delta\tau J_z/4} \sinh\left(\frac{\Delta\tau J_x}{2}\right). \tag{10.16}
\end{aligned}$$

The other five matrix elements are listed in Fig. 10.1 and may be computed in the same manner.

We are now faced with a problem, namely that the spin-flip matrix elements are negative. However, for non-frustrated spin systems, we can show that the overall sign of the world-line configuration is positive. To prove this statement consider a bipartite lattice in arbitrary dimensions. A bipartite lattice may be split into two sub-lattices, A and B , such that the nearest neighbors of sub-lattice A belong to sub-lattice B and vice-versa. A non-frustrated spin system on a bipartite lattice has solely spin-spin interactions between two lattice sites belonging to different sub-lattices. For example, in our 1D case, the even sites correspond to say sub-lattice A and the odd sites to sub-lattice B . Under those conditions we can carry out the canonical transformation (i.e. the commutation rules remain invariant) $S_i^x \rightarrow f(i)S_i^x$, $S_i^y \rightarrow f(i)S_i^y$, and $S_i^z \rightarrow S_i^z$, where $f(i) = 1$ (-1) if i belongs to sublattice A (B). Under this transformation, the matrix element J_x in the Hamiltonian transforms to $-J_x$, which renders all matrix elements positive. The above canonical transformation just tells us that the spin-flip matrix element occurs an even number of times in any world-line configuration. The minus sign in the spin-flip matrix element may not be omitted in the case of frustrated spin systems. This negative sign leads to a sign problem which up to date inhibits large scale QMC simulations of frustrated spin systems.

10.2.2 Observables

In the previous section, we have shown how to write the partition function of a non-frustrated spin system as a sum over world-line configurations, each world-line configuration having a positive weight. Our task is now to compute observables

$$\langle O \rangle = \frac{\text{Tr} [e^{-\beta H} O]}{\text{Tr} [e^{-\beta H}]} = \frac{\sum_w \Omega(w) O(w)}{\sum_w \Omega(w)}, \tag{10.17}$$

where $\Omega(w)$ corresponds to the weight of a given world-line configuration as obtained through multiplication of the weights of the individual plaquettes listed in Fig. 10.1 and $O(w)$ corresponds to the value of the observable for the given world-line configuration.

One of the major drawbacks of the world-line algorithm used to be that one could not measure arbitrary observables. In particular, the correlation functions such as $S_i^+ S_j^-$ which introduce a cut in a world-line configuration are not accessible with continuous world lines and local updates. This problem disappears in the loop algorithm and also with worms and directed loops, as will be discussed later. Here we will concentrate on observables which locally conserve the z -component of spin, specifically the total energy as well as the spin-stiffness.

10.2.2.1 Energy and Spin-Spin Correlations

Neglecting the systematic error originating from the Trotter decomposition, the expectation value of the energy is given by

$$\begin{aligned} \langle H \rangle &= \frac{1}{Z} \text{Tr} \left[(e^{-\Delta\tau H_1} e^{-\Delta\tau H_2})^m (H_1 + H_2) \right] \\ &= \frac{1}{Z} \text{Tr} \left[(e^{-\Delta\tau H_1} e^{-\Delta\tau H_2})^{m-1} \left(e^{-\Delta\tau H_1} H_1 e^{-\Delta\tau H_2} \right. \right. \\ &\quad \left. \left. + e^{-\Delta\tau H_1} e^{-\Delta\tau H_2} H_2 \right) \right]. \end{aligned} \quad (10.18)$$

To obtain the last equation, we have used the cyclic properties of the trace: $\text{Tr}[AB] = \text{Tr}[BA]$. Inserting the unit operator $1 = \sum_{\sigma} |\sigma\rangle\langle\sigma|$ at each imaginary time interval yields

$$\begin{aligned} \langle H \rangle &= \frac{1}{Z} \sum_{\sigma_1, \dots, \sigma_{2m}} [\langle\sigma_1|e^{-\Delta\tau H_1}|\sigma_{2m}\rangle \dots \langle\sigma_3|e^{-\Delta\tau H_1}|\sigma_2\rangle \langle\sigma_2|e^{-\Delta\tau H_2} H_2|\sigma_1\rangle \\ &\quad + \langle\sigma_1|e^{-\Delta\tau H_1}|\sigma_{2m}\rangle \dots \langle\sigma_3|e^{-\Delta\tau H_1} H_1|\sigma_2\rangle \langle\sigma_2|e^{-\Delta\tau H_2}|\sigma_1\rangle] \\ &= \frac{1}{Z} \sum_{\sigma_1, \dots, \sigma_{2m}} \langle\sigma_1|e^{-\Delta\tau H_1}|\sigma_{2m}\rangle \dots \langle\sigma_3|e^{-\Delta\tau H_1}|\sigma_2\rangle \langle\sigma_2|e^{-\Delta\tau H_2}|\sigma_1\rangle \\ &\quad \times \left[\frac{\langle\sigma_3|e^{-\Delta\tau H_1} H_1|\sigma_2\rangle}{\langle\sigma_3|e^{-\Delta\tau H_1}|\sigma_2\rangle} + \frac{\langle\sigma_2|e^{-\Delta\tau H_2} H_2|\sigma_1\rangle}{\langle\sigma_2|e^{-\Delta\tau H_2}|\sigma_1\rangle} \right] \\ &= \frac{\sum_w \Omega(w) E(w)}{\sum_w \Omega(w)} \end{aligned} \quad (10.19)$$

with

$$E(w) = -\frac{\partial}{\partial \Delta\tau} [\ln \langle\sigma_2|e^{-\Delta\tau H_2}|\sigma_1\rangle + \ln \langle\sigma_3|e^{-\Delta\tau H_1}|\sigma_2\rangle]. \quad (10.20)$$

We can of course measure the energy on arbitrary time slices. Averaging over all the time slices to reduce the fluctuations yields the form

$$E(w) = -\frac{1}{m} \frac{\partial}{\partial \Delta\tau} \ln \Omega(w). \quad (10.21)$$

Hence the energy of a world-line configuration is nothing but the logarithmic derivative of its weight. This can also be obtained more directly by taking the derivative of (10.14).

Observables O which locally conserve the z -component of the spin are easy to compute. If we decide to measure on time slice τ then $O|\sigma_\tau\rangle = O(w)|\sigma_\tau\rangle$. An example of such an observable is the correlation function $O = S_i^z S_j^z$.

10.2.2.2 Spin Stiffness (Superfluid Density)

The spin stiffness probes the sensitivity of the system under a twist – in spin space – of the boundary condition along one lattice direction. If long-range spin order is present, the free energy in the thermodynamic limit will acquire a dependence on the twist. If on the other hand the system is disordered, the free energy is insensitive to the twist. The spin stiffness hence probes for long range or quasi long-range spin ordering. It is identical to the superfluid density when viewing spin systems in terms of hard-core bosons. To define the spin stiffness, we consider the Heisenberg model on a d -dimensional hyper-cubic lattice of linear length L :

$$H = J \sum_{\langle i,j \rangle} \tilde{\mathbf{S}}_i \cdot \tilde{\mathbf{S}}_j . \quad (10.22)$$

We impose twisted boundary condition in say the x -direction,

$$\tilde{\mathbf{S}}_{i+Le_x} = R(\mathbf{e}, \phi) \tilde{\mathbf{S}}_i . \quad (10.23)$$

where $R(\mathbf{e}, \phi)$ is an $SO(3)$ rotation around the axis \mathbf{e} with angle ϕ . In the other lattice directions, we consider periodic boundary conditions. The spin stiffness is then defined as

$$\rho_s = \frac{1}{L^{d-2}} \left. \frac{-1}{\beta} \ln Z(\phi) \right|_{\phi=0} , \quad (10.24)$$

where $Z(\phi)$ is the partition function in the presence of the twist in the boundary condition, and β corresponds to the inverse temperature.

Under the canonical transformation

$$\mathbf{S}_i = R(\mathbf{e}, -\frac{\phi}{L} \mathbf{i} \cdot \mathbf{e}_x) \tilde{\mathbf{S}}_i \quad (10.25)$$

the twist may be eliminated from the boundary condition

$$\begin{aligned} \mathbf{S}_{i+Le_x} &= R \left[\mathbf{e}, -\frac{\phi}{L} (\mathbf{i} + Le_x) \cdot \mathbf{e}_x \right] \tilde{\mathbf{S}}_{i+Le_x} \\ &= R \left[\mathbf{e}, -\frac{\phi}{L} (\mathbf{i} + Le_x) \cdot \mathbf{e}_x \right] R(\mathbf{e}, \phi) \tilde{\mathbf{S}}_i \\ &= R \left[\mathbf{e}, -\frac{\phi}{L} \mathbf{i} \cdot \mathbf{e}_x \right] \tilde{\mathbf{S}}_i = \mathbf{S}_i \end{aligned} \quad (10.26)$$

to appear explicitly in the Hamiltonian

$$\begin{aligned}
 H &= J \sum_{\langle i,j \rangle} \left[R(\mathbf{e}, -\frac{\phi}{L} \mathbf{i} \cdot \mathbf{e}_x) \mathbf{S}_i \right] \cdot \left[R(\mathbf{e}, -\frac{\phi}{L} \mathbf{j} \cdot \mathbf{e}_x) \mathbf{S}_j \right] \\
 &= J \sum_{\langle i,j \rangle} \mathbf{S}_i \cdot R \left[\mathbf{e}, \frac{\phi}{L} (\mathbf{i} - \mathbf{j}) \cdot \mathbf{e}_x \right] \mathbf{S}_j \\
 &= J \sum_i \mathbf{S}_i \cdot R(\mathbf{e}, -\frac{\phi a}{L}) \mathbf{S}_{i+\mathbf{a}_x} + J \sum_{i, \mathbf{a} \neq \mathbf{a}_x} \mathbf{S}_i \cdot \mathbf{S}_{i+\mathbf{a}}. \quad (10.27)
 \end{aligned}$$

Setting the rotation axis \mathbf{e} to \mathbf{e}_z such that

$$R \left(\mathbf{e}, -\frac{\phi a}{L} \right) = \begin{pmatrix} \cos(\phi a/L) & \sin(\phi a/L) & 0 \\ -\sin(\phi a/L) & \cos(\phi a/L) & 0 \\ 0 & 0 & 1 \end{pmatrix} \quad (10.28)$$

the Hamiltonian may be written as

$$\begin{aligned}
 H &= J \sum_i \left[S_i^z S_{i+\mathbf{a}_x}^z + \frac{1}{2} (e^{i\phi a/L} S_i^+ S_{i+\mathbf{a}_x}^- + e^{-i\phi a/L} S_i^- S_{i+\mathbf{a}_x}^+) \right] \\
 &+ J \sum_{i, \mathbf{a} \neq \mathbf{a}_x} \left[S_i^z S_{i+\mathbf{a}}^z + \frac{1}{2} (S_i^+ S_{i+\mathbf{a}}^- + S_i^- S_{i+\mathbf{a}}^+) \right]. \quad (10.29)
 \end{aligned}$$

In the spirit of the world-line algorithm, we write the partition function as

$$Z(\phi) = \sum_w \underbrace{\prod_p}_{\Omega(w, \phi)} W(S_p(w), \phi). \quad (10.30)$$

The sum runs over all world-line configurations w and the weight of the world-line configuration, $\Omega(w)$, is given by the product of the individual plaquette weights $W(S_p(w), \phi)$ in the space-time lattice. $S_p(w)$ denotes the spin configuration on plaquette p in the world-line configuration w .

Since at $\phi = 0$ time reversal symmetry holds, the spin current

$$j_s = -\frac{1}{\beta} \frac{\partial}{\partial \phi} \ln Z(\phi) \Big|_{\phi=0} \quad (10.31)$$

vanishes and the spin stiffness reads

$$\rho_s = \frac{1}{Z} \sum_w \Omega(w) \rho_s(w) \quad (10.32)$$

where

$$\begin{aligned} \rho_s(w) = & -\frac{1}{\beta L^{d-2}} \left(\sum_p \frac{\frac{\partial^2}{\partial \phi^2} W(S_p(w), \phi)|_{\phi=0}}{W(S_p(w))} \right. \\ & \left. + \sum_{p \neq q} \frac{\frac{\partial}{\partial \phi} W(S_p(w), \phi)|_{\phi=0}}{W(S_p(w))} \frac{\frac{\partial}{\partial \phi} W(S_q(w), \phi)|_{\phi=0}}{W(S_q(w))} \right) \end{aligned} \quad (10.33)$$

It is instructive to compute the spin stiffness in the limit $\Delta\tau \rightarrow 0$ since in this limit ρ_s is nothing but the average of the square of the total spatial winding number of the world lines. Let $\sigma_{1,p}, \sigma_{2,p}, \sigma_{3,p}$ and $\sigma_{4,p}$ correspond to the spin configuration S_p and $\mathbf{i}_p, \mathbf{j}_p$ to the two real space points associated to the plaquette p such that

$$\begin{aligned} & \lim_{\Delta\tau \rightarrow 0} \frac{\frac{\partial^2}{\partial \phi^2} W(S_p(w), \phi)|_{\phi=0}}{W(S_p(w))} \\ &= \lim_{\Delta\tau \rightarrow 0} -\frac{\Delta\tau J}{2} \left[\frac{\mathbf{i}e_x \cdot (\mathbf{j}_p - \mathbf{i}_p)}{L} \right]^2 \frac{\langle \sigma_{1,p}, \sigma_{2,p} | S_{\mathbf{i}_p}^+ S_{\mathbf{j}_p}^- + S_{\mathbf{i}_p}^- S_{\mathbf{j}_p}^+ | \sigma_{3,p}, \sigma_{4,p} \rangle}{\langle \sigma_{1,p}, \sigma_{2,p} | 1 - \Delta\tau H_{\mathbf{i}_p, \mathbf{j}_p} | \sigma_{3,p}, \sigma_{4,p} \rangle} \\ &= \left[\frac{\mathbf{i}e_x \cdot (\mathbf{j}_p - \mathbf{i}_p)}{L} \langle \sigma_{1,p}, \sigma_{2,p} | S_{\mathbf{i}_p}^+ S_{\mathbf{j}_p}^- + S_{\mathbf{i}_p}^- S_{\mathbf{j}_p}^+ | \sigma_{3,p}, \sigma_{4,p} \rangle \right]^2. \end{aligned} \quad (10.34)$$

In the last line have used the fact $\langle \sigma_{1,p}, \sigma_{2,p} | S_{\mathbf{i}_p}^+ S_{\mathbf{j}_p}^- + S_{\mathbf{i}_p}^- S_{\mathbf{j}_p}^+ | \sigma_{3,p}, \sigma_{4,p} \rangle = 1$ if there is a spin-flip process on plaquette p and zero otherwise. Similarly, we have:

$$\begin{aligned} & \lim_{\Delta\tau \rightarrow 0} \frac{\frac{\partial}{\partial \phi} W(S_p(w), \phi)|_{\phi=0}}{W(S_p(w))} \\ &= \lim_{\Delta\tau \rightarrow 0} -\frac{\Delta\tau J}{2} \frac{\mathbf{i}e_x \cdot (\mathbf{j}_p - \mathbf{i}_p)}{L} \frac{\langle \sigma_{1,p}, \sigma_{2,p} | (S_{\mathbf{i}_p}^+ S_{\mathbf{j}_p}^- - S_{\mathbf{i}_p}^- S_{\mathbf{j}_p}^+) | \sigma_{3,p}, \sigma_{4,p} \rangle}{\langle \sigma_{1,p}, \sigma_{2,p} | 1 - \Delta\tau H_{\mathbf{i}_p, \mathbf{j}_p} | \sigma_{3,p}, \sigma_{4,p} \rangle} \\ &= \frac{\mathbf{i}e_x \cdot (\mathbf{j}_p - \mathbf{i}_p)}{L} \langle \sigma_{1,p}, \sigma_{2,p} | S_{\mathbf{i}_p}^+ S_{\mathbf{j}_p}^- - S_{\mathbf{i}_p}^- S_{\mathbf{j}_p}^+ | \sigma_{3,p}, \sigma_{4,p} \rangle. \end{aligned} \quad (10.35)$$

Since $\langle \sigma_{1,p}, \sigma_{2,p} | S_{\mathbf{i}_p}^+ S_{\mathbf{j}_p}^- - S_{\mathbf{i}_p}^- S_{\mathbf{j}_p}^+ | \sigma_{3,p}, \sigma_{4,p} \rangle = \pm 1$ if there is a spin-flip process on plaquette p and zero otherwise the identity

$$\lim_{\Delta\tau \rightarrow 0} \frac{\frac{\partial^2}{\partial \phi^2} W(S_p(w), \phi)|_{\phi=0}}{W(S_p(w))} = \left(\lim_{\Delta\tau \rightarrow 0} \frac{\frac{\partial}{\partial \phi} W(S_p(w), \phi)|_{\phi=0}}{W(S_p(w))} \right)^2 \quad (10.36)$$

holds. Hence, one can rewrite the spin stiffness as

$$\rho_s(w) = \frac{1}{\beta L^d} (W_x(w))^2, \quad (10.37)$$

where the winding number along the x -lattice direction W_x is given by

$$W_x(w) = \sum_p e_x \cdot (\mathbf{j}_p - \mathbf{i}_p) \langle \sigma_{1,p}, \sigma_{2,p} | S_{i_p}^+ S_{j_p}^- - S_{i_p}^- S_{j_p}^+ | \sigma_{3,p}, \sigma_{4,p} \rangle . \quad (10.38)$$

10.2.3 Updating Schemes

The problem is now cast into one which may be solved with classical Monte Carlo methods where we need to generate a Markov chain through the space of world-line configurations. Along the chain the world-line configuration w , occurs on average with normalized probability $\Omega(w)$. There are many ways of generating the Markov chain. Here we will first discuss a local updating scheme and its limitations. We will then turn our attention to a more powerful updating scheme which is known under the name of loop algorithm.

10.2.3.1 Local Updates

Local updates deform a world-line configuration locally. As shown in Fig. 10.2 one randomly chooses a shaded plaquette and, if possible, shifts a world line from one side of the shaded plaquette to the other. This move is local and only involves the four plaquettes surrounding the shaded one. It is then easy to calculate the ratio of weights of the new to old world-line configurations and accept the move according to a Metropolis criterion. As it stands, the above described local move is not ergodic. For example, the z -component of spin is conserved. This problem can be circumvented by considering a move which changes a single down world line into an up one and vice-versa. However, such a global move will have very low acceptance probability at large β .

Combined, both types of moves are ergodic but only in the case of open boundary conditions in space. The algorithm is not ergodic if periodic or anti-periodic boundary conditions are chosen. Consider a starting configuration with zero winding (i.e. $W_x(w) = 0$). The reader will readily convince himself that with local updates, it will never be possible to generate a configuration with $W_x(w) \neq 0$. Hence, for example, a spin stiffness may not be measured within the world-line algorithm with local updates. However, one should note that violation of ergodicity lies in

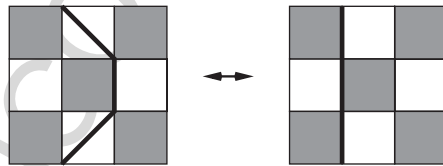


Fig. 10.2. Local updates. A shaded plaquette is chosen randomly and a World Line is shifted from left to right or vice versa across the shaded plaquette

the choice of the boundary condition. Since bulk properties are boundary independent in the thermodynamic limit, the algorithm will yield the correct results in the thermodynamic limit [20].

Different local updates without such problems have been invented in recent years, namely *worms* and *directed loops*. They work by allowing a partial world line, and iteratively changing the position of its ends until it closes again. They will be discussed in Sect. 10.4.5.

10.2.3.2 Loop Updates

To introduce loop updates, it is useful to first map the XXZ model onto the six vertex model of statistical mechanics.

10.2.3.2.1 Equivalence to the Six Vertex Model

That the XXZ quantum spin chain is equivalent to the classical 2D six vertex model follows from a one to one mapping of a world-line configuration to one of the six vertex model. The identification of single plaquettes is shown in Fig. 10.3(a). The world-line configuration of Fig. 10.1 is plotted in the language of the six vertex model in Fig. 10.3(b). The vertex model lies on a 45 degrees rotated lattice denoted by bullets in Fig. 10.3(b). At each vertex (bullets in Fig. 10.3) the number of incoming arrows equals the number of outgoing arrows. In the case of the XYZ chain, source and drain terms have to be added, yielding the eight vertex model.

The identification of the XXZ model to the six vertex model gives us an intuitive picture of loop updates [3]. Consider the world-line configuration in Fig. 10.4(a) and it's corresponding vertex formulation (Fig. 10.4(b)). One can pick a site at random and follow the arrows of the vertex configuration. At each plaquette there are two possible arrow paths to follow. One is chosen, appropriately, and one follows the arrows to arrive to the next plaquette. The procedure is then repeated until one returns to the starting point. Such a loop is shown in Fig. 10.4(c). Along the loop,

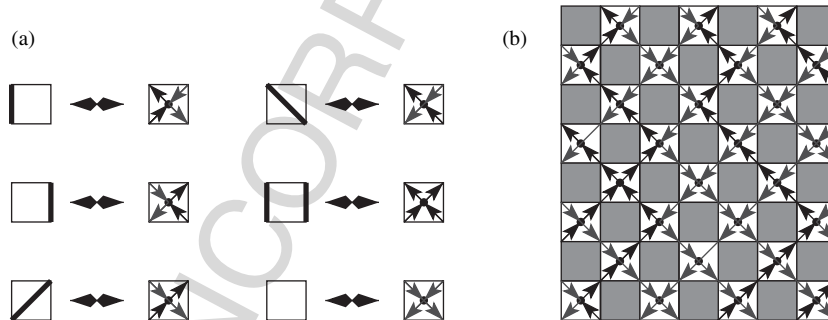


Fig. 10.3. (a) Identification of world-line configurations on plaquettes with the vertices of the six vertex model. (b) The world-line configuration of Fig. 10.1 in the language of the six vertex model

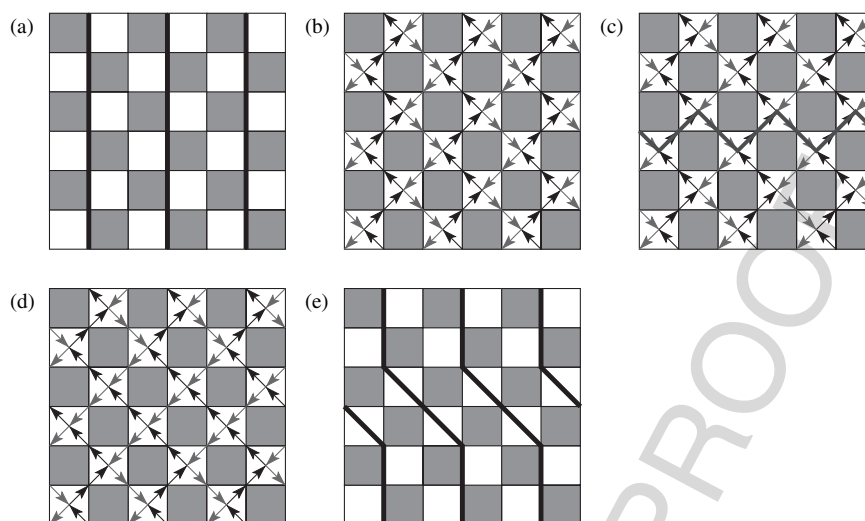


Fig. 10.4. Example of a loop update

changing the direction of the arrows generates another valid vertex configuration, see Fig. 10.4(d). The corresponding world-line configuration (after flipping the loop) is shown in Fig. 10.4(e). As apparent, this is a global update which in this example changes the winding number. This was not achievable with local moves.

10.2.3.2.2 Loop Updates

In the previous paragraph we have seen how to build a loop. Flipping the loop has the potential of generating large-scale changes in the world-line configuration and hence allows us to move quickly in the space of world lines. There is however a potential problem. If the loops were constructed at random, then the acceptance rate for flipping a loop would be extremely small and loop updates would not lead to an efficient algorithm. The loop algorithm sets up rules to build the loop such that it can be flipped without any additional acceptance step for the XXZ model.

To do so, additional variables are introduced, which specify for each plaquette the direction which a loop should take there, Fig. 10.5. These specifications, called breakups or plaquette-graphs, are completely analogous to the Fortuin-Kasteleyn bond-variables of the Swendsen-Wang cluster algorithm, discussed in Chap. 4. They can also be thought of as parts of the Hamilton operator, as discussed in Sect. 10.4. Note that when a breakup has been specified for every plaquette, this then graphically determines a complete decomposition of the vertex-lattice into a set of loops (see also below). The loop algorithm is a cluster algorithm mapping from such sets of loops to world-line configurations and back to new sets of loops. In contrast, directed loops are a local method not associated with such graphs.

Which plaquette-graphs are possible? For each plaquette and associated vertex (spin-configuration) there are several possible choices of plaquette-graphs which

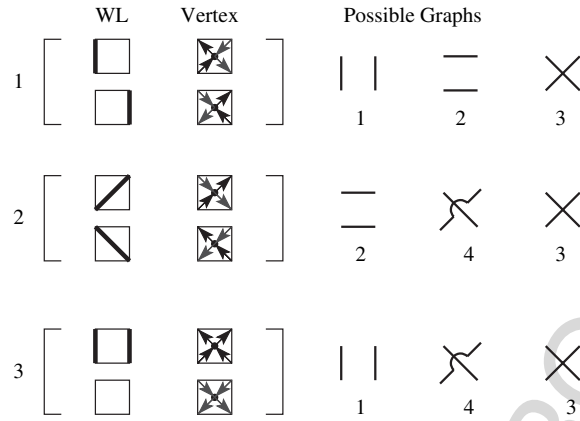


Fig. 10.5. Possible plaquette-graphs for vertex configurations. Graph one is a vertical breakup, graph two a horizontal one, graph four is diagonal. Plaquette-graph three is called frozen; it corresponds to the combined flip of all four arrows

are compatible with the fact that the arrow direction may not change in the construction of the loop. Figure 10.5 illustrates this. Given the vertex configurations one in Fig. 10.5 one can follow the arrows vertically (graph one) or horizontally (graph two). There is also the possibility to flip all the spins of the vertex. This corresponds to graph three in Fig. 10.5. The plaquette-graph configuration defines the loops along which one will propose to flip the orientation of the arrows of the vertex model.

In order to find appropriate probabilities for choosing the breakups, we need to find weights $W(S, G)$ for each of the combinations of spin configuration S on a plaquette and plaquette-graph G shown in Fig. 10.5. We require that

$$\sum_G W(S, G) = W(S) , \tag{10.39}$$

where $W(S)$ is the weight of the vertex S , i.e. we subdivide the weight of each spin-configuration on a vertex onto the possible graphs, for example graphs one, four and three if $S = 3$, see Fig. 10.5.

Starting from a vertex configuration S on a plaquette we choose an allowed plaquette-graph with probability

$$P(S \rightarrow (S, G)) = \frac{W(S, G)}{W(S)} . \tag{10.40}$$

for every vertex-plaquette of the lattice. We then have a configuration of vertices and plaquette-graphs. When a plaquette-graph has been chosen for every plaquette, the combined lines subdivide the lattice into a set of loops. To achieve a constant acceptance rate for the flip of each loop, we require that for a given plaquette-graph G

$$W(S, G) = W(S', G) , \tag{10.41}$$

where S' is obtained from S by flipping the arrows of the vertex configuration according the rules of the graph G . That is for $G = 1$ in Fig. 10.5 we require $W(S = 1, G = 1) = W(S = 3, G = 1)$. This equation can be satisfied with weights $W(S, G) = V(G)$ when S and G are compatible and $W(S, G) = 0$ otherwise.

When choosing the heat-bath algorithm for flipping, the probability of flipping the arrows along the loop is given by

$$P((S, G) \rightarrow (S', G)) = \frac{W(S', G)/(W(S, G))}{1 + W(S', G)/(W(S, G))} = \frac{1}{2}. \quad (10.42)$$

Thus each loop is flipped with probability 1/2. This generates a new, highly independent, world-line configuration. The previous plaquette-graphs are then discarded, and another update starts with the choice of new plaquette-graphs according to (10.40).

With (10.41) and (10.42) the detailed balance in the space of graphs and spins

$$W(S, G)P[(S, G) \rightarrow (S', G)] = W(S', G)P[(S', G) \rightarrow (S, G)] \quad (10.43)$$

is trivially satisfied. Detailed balance in the space of spins follows from:

$$\begin{aligned} & W(S)P(S \rightarrow S') \\ &= W(S) \sum_G P[S \rightarrow (S, G)]P[(S, G) \rightarrow (S', G)] \\ &= \sum_G W(S) \frac{W(S, G)}{W(S)} P[(S, G) \rightarrow (S', G)] \\ &= \sum_G W(S') \frac{W(S', G)}{W(S')} P[(S', G) \rightarrow (S, G)] = W(S')P(S' \rightarrow S). \end{aligned} \quad (10.44)$$

This completes the formal description of the algorithm. We will now illustrate the algorithm in the case of the isotropic Heisenberg model ($J = J_x = J_z$) since this turns out to be a particularly simple case. Equations (10.39) and (10.41) lead to

$$\begin{aligned} e^{\Delta\tau J/4} \cosh(\Delta\tau J/2) &\equiv W_1 = W_{1,1} + W_{1,2} + W_{1,3} \\ e^{\Delta\tau J/4} \sinh(\Delta\tau J/2) &\equiv W_2 = W_{2,2} + W_{2,4} + W_{2,3} \\ e^{-\Delta\tau J/4} &\equiv W_3 = W_{3,1} + W_{3,4} + W_{3,3} \end{aligned} \quad (10.45)$$

with $W_{3,1} = W_{1,1}$, $W_{1,2} = W_{2,2}$ and $W_{2,4} = W_{3,4}$. Here we adopt the notation $W_{i,j} = W(S = i, G = j)$ and $W_i = W(S = i)$. To satisfy the above equations for the special case of the Heisenberg model, we can set $W_{\bullet,3} = W_{\bullet,4} = 0$ and thereby consider only the graphs $G = 1$ and $G = 2$. The reader will readily verify that the equations

$$\begin{aligned} e^{\Delta\tau J/4} \cosh(\Delta\tau J/2) &\equiv W_1 = W_{1,1} + W_{1,2} \\ e^{\Delta\tau J/4} \sinh(\Delta\tau J/2) &\equiv W_2 = W_{2,2} = W_{1,2} \\ e^{-\Delta\tau J/4} &\equiv W_3 = W_{1,1} = W_{3,1} \end{aligned} \quad (10.46)$$

are satisfied. We will then only have vertical and horizontal breakups. The probability of choosing a horizontal breakup is $\tanh(\Delta\tau J/2)$ on an antiferromagnetic plaquette (i.e. type one), it is unity on type two, and zero on a ferromagnetic plaquette (type three).

Further aspects of the loop algorithm will be discussed in Sect. 10.3.

10.2.4 The Sign Problem in the World-Line Approach

The QMC approach is often plagued by the so-called sign problem. Since the origin of this problem is easily understood in the framework of the world-line algorithm we will briefly discuss it in this section on a specific model. Consider spinless electrons on an L -site linear chain

$$H = -t \sum_i c_i^\dagger (c_{i+1} + c_{i+2}) + \text{H.c.} \quad (10.47)$$

with $\{c_i^\dagger, c_j^\dagger\} = \{c_i, c_j\} = 0$, $\{c_i^\dagger, c_j\} = \delta_{i,j}$. Here, we consider periodic boundary conditions, $c_{i+L} = c_i$ and $t > 0$.

The world-line representation of spinless fermions is basically the same as that of spin-1/2 degrees of freedom (which themselves are equivalent to so-called hardcore bosons) on any lattice. For fermions, world lines stand for occupied locations in space-time. Additional signs occur when fermion world lines wind around each other, as we will now discuss.

For the above Hamiltonian it is convenient to split it into a set of independent four site problems

$$H = \underbrace{\sum_{n=0}^{L/4-1} H^{(4n+1)}}_{H_1} + \underbrace{\sum_{n=0}^{L/4-1} H^{(4n+3)}}_{H_2} \quad (10.48)$$

with $H^{(i)} = -tc_i^\dagger(c_{i+1}/2 + c_{i+2}) - tc_{i+1}^\dagger(c_{i+2} + c_{i+3}) - tc_{i+2}^\dagger c_{i+3}/2 + \text{H.c.}$. With this decomposition one obtains the graphical representation of Fig. 10.6 [21].

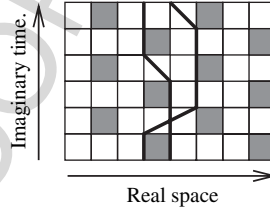


Fig. 10.6. World-line configuration for the model of (10.47). Here $m = 3$. Since the two electrons exchange their positions during the imaginary time propagation, this world-line configuration has a negative weight

The sign problem occurs due to the fact that the weights $\Omega(w)$ are not necessarily positive. An example is shown in Fig. 10.6. In this case the origin of negative signs lies in Fermi statistics. Negative weights cannot be interpreted as probabilities. To circumvent the problem, one decides to carry out the sampling with an auxiliary probability distribution

$$\overline{Pr}(w) = \frac{|\Omega(w)|}{\sum_w |\Omega(w)|}, \quad (10.49)$$

which in the limit of small values of $\Delta\tau$ corresponds to the partition function of the Hamiltonian of (10.47) but with fermions replaced by hard-core bosons. Thus, we can now evaluate (10.17) with

$$\langle O \rangle = \frac{\sum_w \overline{Pr}(w) \text{sign}(w) O(w)}{\sum_w \overline{Pr}(w) \text{sign}(w)}, \quad (10.50)$$

where both the numerator and denominator are evaluated with MC methods. Let us first consider the denominator

$$\langle \text{sign} \rangle = \sum_w \overline{Pr}(w) \text{sign}(w) = \frac{\sum_w \Omega(w)}{\sum_w |\Omega(w)|} = \frac{\text{Tr} [e^{-\beta H}]}{\text{Tr} [e^{-\beta H_B}]}. \quad (10.51)$$

Here, H_B corresponds to the Hamiltonian of (10.47) but with fermions replaced by hard-core bosons. In the limit of large inverse temperatures β the partition functions is dominated by the ground state. Thus in this limit

$$\langle \text{sign} \rangle \sim e^{-\beta(E_0 - E_0^B)} = e^{-\beta L \Delta}, \quad (10.52)$$

where $\Delta = (E_0 - E_0^B) / L$ is an intensive, in general positive, quantity. The above equation corresponds to the sign problem. When the temperature is small or system size large, the average sign becomes exponentially small. Hence, the observable $\langle O \rangle$ is given by the quotient of two exponentially small values which are determined stochastically. Since $\langle \text{sign} \rangle$ is the average of values ± 1 , its variance is extremely large. When the error-bars become comparable to the average sign, uncontrolled fluctuations in the evaluation of $\langle O \rangle$ will occur. Two comments are in order:

- (i) In this simple example the sign problem occurs due to Fermi statistics. However, sign problems occur equally in frustrated spin-1/2 systems which are nothing but hard-core boson models. Note that replacing the fermions by hard-core bosons in (10.47) and considering hopping matrix elements of different signs between nearest and next-nearest neighbors will generate a sign problem in the above formulation.
- (ii) The sign problem is formulation dependent.

In the world-line algorithm, we decide to work in real space. Had we chosen Fourier space, the Hamiltonian would have been diagonal and hence no sign problem would have occurred. In the auxiliary field approach discussed in the next section the sign

problem would not occur for this non-interacting problem since one body operators are treated exactly. That is, the sum over all world lines is carried out exactly in that approach.

10.2.5 Single-Hole Dynamics in non Frustrated Quantum Magnets

In this section we describe generalizations of the loop algorithm which allow one to investigate the physics of single-hole motion in non-frustrated quantum magnets [22, 23, 24].

The Hamiltonian we will consider is the t - J model defined as

$$H_{t-J} = \mathcal{P} \left(-t \sum_{\langle i,j \rangle, \sigma} c_{i,\sigma}^\dagger c_{j,\sigma} + \text{H.c.} + J \sum_{\langle i,j \rangle} \mathbf{S}_i \cdot \mathbf{S}_j - \frac{1}{4} n_i n_j \right) \mathcal{P}. \quad (10.53)$$

The t - J model lives a Hilbert space where double occupancy on a site is excluded. In the above, this constraint is taken care of by the projection

$$\mathcal{P} = \prod_i (1 - n_{i,\uparrow} n_{i,\downarrow}), \quad (10.54)$$

which filters out all states with double occupancy.

To access the single-hole problem, we carry out a canonical transformation to rewrite the fermionic operators, $c_{i,\sigma}^\dagger$, in terms of spinless fermions and spin 1/2 degrees of freedom. On a given site the product space of a spinless fermion and a spin 1/2 degree of freedom consists of four states

$$|n, \sigma\rangle \equiv |n\rangle \otimes |\sigma\rangle \quad (10.55)$$

with $n = 0, 1$ and $\sigma = \uparrow, \downarrow$, on which the fermionic

$$\{f^\dagger, f\} = 1, \{f^\dagger, f^\dagger\} = \{f, f\} = 0, \quad (10.56)$$

and spin 1/2 operators,

$$[\sigma^\alpha, \sigma^\beta] = 2i \sum_\gamma \epsilon^{\alpha,\beta,\gamma} \sigma^\gamma \quad (10.57)$$

act.

We can identify the four fermionic states on a given site to the four states in the product space of spinless fermions and spins as:

$$\begin{aligned} |\uparrow\rangle &= c_\uparrow^\dagger |0\rangle \leftrightarrow |1, \uparrow\rangle = |\text{vac}\rangle, \\ |\downarrow\rangle &= c_\downarrow^\dagger |0\rangle \leftrightarrow |1, \downarrow\rangle = \sigma^- |\text{vac}\rangle, \\ |0\rangle &\leftrightarrow |0, \uparrow\rangle = f^\dagger |\text{vac}\rangle, \\ |\downarrow\uparrow\rangle &= c_\downarrow^\dagger c_\uparrow^\dagger |0\rangle \leftrightarrow |0, \downarrow\rangle = f^\dagger \sigma^- |\text{vac}\rangle. \end{aligned} \quad (10.58)$$

Here $\sigma^- = (\sigma^x - i\sigma^y)/2$ and $\sigma^+ = (\sigma^x + i\sigma^y)/2$. The fermionic operators (c_σ^\dagger) are identified as

$$\begin{aligned} c_\uparrow^\dagger &\leftrightarrow \sigma^{z,+} f - \sigma^{z,-} f^\dagger, \\ c_\downarrow^\dagger &\leftrightarrow \sigma^- (f^\dagger + f). \end{aligned} \quad (10.59)$$

with $\sigma^{z,\pm} = (1 \pm \sigma^z)/2$. Under the above canonical transformation the t - J model reads

$$\begin{aligned} \tilde{H}_{t-J} &= \tilde{\mathcal{P}} \left(t \sum_{\langle i,j \rangle} [f_j^\dagger f_i \tilde{P}_{i,j} + \text{H.c.}] + \frac{J}{2} \sum_{\langle i,j \rangle} (\tilde{P}_{i,j} - 1) \tilde{\Delta}_{i,j} \right) \tilde{\mathcal{P}}, \\ \tilde{P}_{i,j} &= \frac{1}{2} (\boldsymbol{\sigma}_i \cdot \boldsymbol{\sigma}_j + 1), \\ \tilde{\Delta}_{i,j} &= 1 - f_i^\dagger f_i - f_j^\dagger f_j, \\ \tilde{\mathcal{P}} &= \prod_i \left(1 - f_i^\dagger f_i \sigma_i^- \sigma_i^+ \right). \end{aligned} \quad (10.60)$$

We can check the validity of the above expression by considering the two-site problem $H_{t-J}^{(i,j)}$. Applying the Hamiltonian on the four states in the projected Hilbert space with two electrons gives

$$\begin{aligned} H_{t-J}^{(i,j)} |\uparrow\rangle_i \otimes |\uparrow\rangle_j &= 0, \\ H_{t-J}^{(i,j)} |\downarrow\rangle_i \otimes |\downarrow\rangle_j &= 0, \\ H_{t-J}^{(i,j)} |\uparrow\rangle_i \otimes |\downarrow\rangle_j &= \mathcal{P} \left(-t |0\rangle_i \otimes |\uparrow\downarrow\rangle_j - t |\uparrow\downarrow\rangle_i \otimes |0\rangle_j \right. \\ &\quad \left. - \frac{J}{2} |\uparrow\rangle_i \otimes |\downarrow\rangle_j + \frac{J}{2} |\downarrow\rangle_i \otimes |\uparrow\rangle_j \right) \\ &= -\frac{J}{2} |\uparrow\rangle_i \otimes |\downarrow\rangle_j + \frac{J}{2} |\downarrow\rangle_i \otimes |\uparrow\rangle_j, \\ H_{t-J}^{(i,j)} |\downarrow\rangle_i \otimes |\uparrow\rangle_j &= \mathcal{P} \left(-t |0\rangle_i \otimes |\downarrow\uparrow\rangle_j - t |\downarrow\uparrow\rangle_i \otimes |0\rangle_j \right. \\ &\quad \left. - \frac{J}{2} |\downarrow\rangle_i \otimes |\uparrow\rangle_j + \frac{J}{2} |\uparrow\rangle_i \otimes |\downarrow\rangle_j \right) \\ &= -\frac{J}{2} |\downarrow\rangle_i \otimes |\uparrow\rangle_j + \frac{J}{2} |\uparrow\rangle_i \otimes |\downarrow\rangle_j. \end{aligned} \quad (10.61)$$

As apparent, starting from a state in the projected Hilbert space the kinetic energy term generates states with double occupancy which have to be projected out. In other words the projection operator does not commute with the kinetic energy. We can now check that one obtains the same result in the representation in terms of spinless fermions and spins. The above equations respectively read

$$\begin{aligned}
\tilde{H}_{t-J}^{(i,j)} |1, \uparrow\rangle_i \otimes |1, \uparrow\rangle_j &= 0, \\
\tilde{H}_{t-J}^{(i,j)} |1, \downarrow\rangle_i \otimes |1, \downarrow\rangle_j &= 0, \\
\tilde{H}_{t-J}^{(i,j)} |1, \uparrow\rangle_i \otimes |1, \downarrow\rangle_j &= \tilde{\mathcal{P}} \left(-\frac{J}{2} |1, \uparrow\rangle_i \otimes |1, \downarrow\rangle_j + \frac{J}{2} |1, \downarrow\rangle_i \otimes |1, \uparrow\rangle_j \right) \\
&= -\frac{J}{2} |1, \uparrow\rangle_i \otimes |1, \downarrow\rangle_j + \frac{J}{2} |1, \downarrow\rangle_i \otimes |1, \uparrow\rangle_j, \\
\tilde{H}_{t-J}^{(i,j)} |1, \downarrow\rangle_i \otimes |1, \uparrow\rangle_j &= \tilde{\mathcal{P}} \left(-\frac{J}{2} |1, \downarrow\rangle_i \otimes |1, \uparrow\rangle_j + \frac{J}{2} |1, \uparrow\rangle_i \otimes |1, \downarrow\rangle_j \right) \\
&= -\frac{J}{2} |1, \downarrow\rangle_i \otimes |1, \uparrow\rangle_j + \frac{J}{2} |1, \uparrow\rangle_i \otimes |1, \downarrow\rangle_j,
\end{aligned} \tag{10.62}$$

which confirms that the matrix elements of $\tilde{H}_{t-J}^{(i,j)}$ are identical to those of $H_{t-J}^{(i,j)}$. The reader can readily carry out the calculation in the one and zero particle Hilbert spaces to see that: $\langle \eta | H_{t-J}^{(i,j)} | \nu \rangle = \langle \tilde{\eta} | \tilde{H}_{t-J}^{(i,j)} | \tilde{\nu} \rangle$, where $|\nu\rangle$ ($|\eta\rangle$) and $|\tilde{\nu}\rangle$ ($|\tilde{\eta}\rangle$) correspond to the same states but in the two different representations. Since the t - J model may be written as a sum of two-sites terms, the above is equivalent to

$$\langle \eta | H_{t-J} | \nu \rangle = \langle \tilde{\eta} | \tilde{H}_{t-J} | \tilde{\nu} \rangle. \tag{10.63}$$

In the representation of (10.61) the t - J model has two important properties which facilitate numerical simulations:

- (i) As apparent from (10.62) the application of the Hamiltonian (without projection) on a state in the projected Hilbert space does not generate states with double occupancy. Hence, the projection operation commutes with the Hamiltonian in this representation. The reader can confirm that this is a statement which holds in the full Hilbert space. This leads to the relation

$$\left[t \sum_{\langle i,j \rangle} [f_j^\dagger f_i \tilde{P}_{i,j} + \text{H.c.}] + \frac{J}{2} \sum_{\langle i,j \rangle} (\tilde{P}_{i,j} - 1) \tilde{\Delta}_{i,j}, \tilde{P} \right] = 0, \tag{10.64}$$

which states that the projection operator is a conserved quantity.

- (ii) The Hamiltonian is bilinear in the spinless fermion operators. This has the consequence that for a fixed spin configuration the spinless fermion may be integrated out.

We now use those two properties to study the problem of single-hole dynamics in un-frustrated quantum magnets. Single-hole dynamics is determined by the Green function. In this section we will define it as

$$G(i-j, \tau) = \langle c_{i,\uparrow}^\dagger(\tau) c_{j,\uparrow} \rangle = \frac{1}{Z} \text{Tr} \left[e^{-(\beta-\tau)H} c_{i,\uparrow}^\dagger e^{-\tau H} c_{j,\uparrow} \right], \tag{10.65}$$

where the trace runs over the Hilbert space with no holes. In the representation of (10.61) the above equation reads

$$G(\mathbf{r}, \tau) = \langle \sigma_i^{z,+}(\tau) f_i(\tau) \sigma_j^{z,+} f_j^\dagger \rangle. \tag{10.66}$$

To use the world-line formulation to the present problem, we introduce the unit operator in the Hilbert space with no holes

$$1 = \sum_{\sigma} |\mathbf{v}, \sigma\rangle \langle \mathbf{v}, \sigma|, \quad |\mathbf{v}, \sigma\rangle = |1, \sigma_1\rangle_1 \otimes |1, \sigma_2\rangle_2 \otimes \dots \otimes |1, \sigma_N\rangle_N, \quad (10.67)$$

as well as the unit operator in the Hilbert space with a single hole

$$1 = \sum_{\mathbf{r}, \sigma} |\mathbf{r}, \sigma\rangle \langle \mathbf{v}, \mathbf{r}|, \quad |\mathbf{r}, \sigma\rangle = \sigma_{\mathbf{r}}^{z,+} f_{\mathbf{r}}^{\dagger} |\mathbf{v}, \sigma\rangle. \quad (10.68)$$

In the above, \mathbf{r} denotes a lattice site and N corresponds to the number of lattice sites. In the definition of the single hole-states, the operator $\sigma_{\mathbf{r}}^{z,+}$ guarantees that we will never generate a doubly occupied state on site \mathbf{r} (i.e. $|0, \downarrow\rangle$).

The Green function may now be written as

$$\begin{aligned} G(\mathbf{i} - \mathbf{j}, \tau) &= \frac{1}{Z} \sum_{\sigma_1} \langle \mathbf{v}, \sigma_1 | (e^{-\Delta\tau H_1} e^{-\Delta\tau H_2})^{m-n\tau} \sigma_{\mathbf{i}}^{z,+} f_{\mathbf{i}} \\ &\quad \times (e^{-\Delta\tau H_1} e^{-\Delta\tau H_2})^{n\tau} \sigma_{\mathbf{j}}^{z,+} f_{\mathbf{j}}^{\dagger} | \mathbf{v}, \sigma_1 \rangle \\ &= \frac{1}{Z} \sum_{\substack{\sigma_1 \dots \sigma_{2m} \\ \mathbf{r}_2 \dots \mathbf{r}_{2n\tau}}} \langle \mathbf{v}, \sigma_1 | e^{-\Delta\tau H_1} | \mathbf{v}, \sigma_{2m} \rangle \\ &\quad \times \langle \mathbf{v}, \sigma_{2m-1} | e^{-\Delta\tau H_2} | \mathbf{v}, \sigma_{2m-2} \rangle \dots \langle \mathbf{v}, \sigma_{2n\tau+1} | \sigma_{\mathbf{i}}^{z,+} f_{\mathbf{i}} e^{-\Delta\tau H_1} | \mathbf{r}_{2n\tau}, \sigma_{2n\tau} \rangle \\ &\quad \times \langle \mathbf{r}_{2n\tau}, \sigma_{2n\tau} | x e^{-\Delta\tau H_2} | \mathbf{r}_{2n\tau-1}, \sigma_{2n\tau-1} \rangle \dots \langle \mathbf{r}_2, \sigma_2 | e^{-\Delta\tau H_2} \sigma_{\mathbf{j}}^{z,+} f_{\mathbf{j}}^{\dagger} | \mathbf{v}, \sigma_1 \rangle \\ &= \frac{\sum_w \Omega(w) G_w(\mathbf{i} - \mathbf{j}, \tau)}{\sum_w \Omega(w)}. \end{aligned} \quad (10.69)$$

The following comments are in order:

- (i) We have neglected the controlled systematic error of order $(\Delta\tau)^2$.
- (ii) $n\tau\Delta\tau = \tau$ and $m\Delta\tau = \beta$.
- (iii) w denotes a world-line configuration defined by the set of spin states $|\sigma_1\rangle \dots |\sigma_{2m}\rangle$. The Boltzmann weight of this state is given by

$$\Omega(w) = \langle \mathbf{v}, \sigma_1 | e^{-\Delta\tau H_1} | \mathbf{v}, \sigma_{2m} \rangle \dots \langle \mathbf{v}, \sigma_2 | e^{-\Delta\tau H_2} | \mathbf{v}, \sigma_1 \rangle \quad (10.70)$$

such that $Z = \sum_w \Omega(w)$ in the partition function of the Heisenberg model.

- (iv) The Green function for a given world-line configuration (w) reads

$$\begin{aligned} G_w(\mathbf{i} - \mathbf{j}, \tau) &= \sum_{\mathbf{r}_{2n\tau} \dots \mathbf{r}_2} \frac{\langle \mathbf{v}, \sigma_{2n\tau+1} | \sigma_{\mathbf{i}}^{z,+} f_{\mathbf{i}} e^{-\Delta\tau H_1} | \mathbf{r}_{2n\tau}, \sigma_{2n\tau} \rangle \dots \\ &\quad \langle \mathbf{v}, \sigma_{2n\tau+1} | e^{-\Delta\tau H_1} | \mathbf{v}, \sigma_{2n\tau} \rangle \dots \\ &\quad \times \frac{\dots \langle \mathbf{r}_2, \sigma_2 | e^{-\Delta\tau H_2} \sigma_{\mathbf{j}}^{z,+} f_{\mathbf{j}}^{\dagger} | \mathbf{v}, \sigma_1 \rangle}{\dots \langle \mathbf{v}, \sigma_2 | e^{-\Delta\tau H_2} | \mathbf{v}, \sigma_1 \rangle}. \end{aligned} \quad (10.71)$$

Defining

$$\begin{aligned} [A_1(\sigma_2, \sigma_1)]_{\mathbf{r}, \mathbf{j}} &= \frac{\langle v, \sigma_2 | f_{\mathbf{r}} \sigma_{\mathbf{r}}^{z,+} e^{-\Delta\tau H_1} \sigma_{\mathbf{j}}^{z,+} f_{\mathbf{j}}^\dagger | v, \sigma_1 \rangle}{\langle v, \sigma_2 | e^{-\Delta\tau H_1} | v, \sigma_1 \rangle}, \\ [A_2(\sigma_2, \sigma_1)]_{\mathbf{r}, \mathbf{j}} &= \frac{\langle v, \sigma_2 | f_{\mathbf{r}} \sigma_{\mathbf{r}}^{z,+} e^{-\Delta\tau H_2} \sigma_{\mathbf{j}}^{z,+} f_{\mathbf{j}}^\dagger | v, \sigma_1 \rangle}{\langle v, \sigma_2 | e^{-\Delta\tau H_2} | v, \sigma_1 \rangle} \end{aligned} \quad (10.72)$$

and since the single-hole states are given by $|\mathbf{r}, \boldsymbol{\sigma}\rangle = \sigma_{\mathbf{r}}^{z,+} f_{\mathbf{r}}^\dagger |v, \boldsymbol{\sigma}\rangle$, the Green function for a given world-line configuration is given by

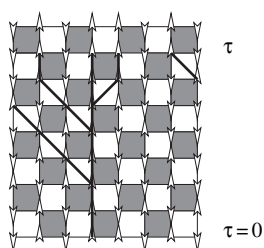
$$G_w(\mathbf{i} - \mathbf{j}, \tau) = [A_1(\sigma_{2n_\tau+1}, \sigma_{2n_\tau}) A_2(\sigma_{2n_\tau}, \sigma_{2n_\tau+1}) \cdots \cdots A_1(\sigma_3, \sigma_2) A_2(\sigma_2, \sigma_1)]_{\mathbf{i}, \mathbf{j}}. \quad (10.73)$$

We are now left with the task of computing the matrix A . Since H_2 is a sum of commuting bond Hamiltonians (H_b) $[A_1(\boldsymbol{\sigma}_3, \boldsymbol{\sigma}_2)]_{\mathbf{i}, \mathbf{j}}$ does not vanish only if \mathbf{i} and \mathbf{j} belong to the same bond \tilde{b} . In particular, denoting the two-spin configuration on bond b by $\boldsymbol{\sigma}_{1,b}, \boldsymbol{\sigma}_{2,b}$ we have

$$\begin{aligned} &A_2(\boldsymbol{\sigma}_2, \boldsymbol{\sigma}_1)_{\mathbf{i}, \mathbf{j}} \\ &= \frac{\left[\prod_{b \neq \tilde{b}} \langle v, \boldsymbol{\sigma}_{2,b} | e^{-\Delta\tau H_b} | v, \boldsymbol{\sigma}_{1,b} \rangle \right] \langle v, \boldsymbol{\sigma}_{2,\tilde{b}} | \sigma_{\mathbf{i}}^{z,+} f_{\mathbf{i}} e^{-\Delta\tau H_{\tilde{b}}} \sigma_{\mathbf{j}}^{z,+} f_{\mathbf{j}}^\dagger | v, \boldsymbol{\sigma}_{1,\tilde{b}} \rangle}{\prod_b \langle v, \boldsymbol{\sigma}_{b,2} | e^{-\Delta\tau H_b} | v, \boldsymbol{\sigma}_{b,1} \rangle} \\ &= \frac{\langle v, \boldsymbol{\sigma}_{2,\tilde{b}} | \sigma_{\mathbf{i}}^{z,+} f_{\mathbf{i}} e^{-\Delta\tau H_{\tilde{b}}} \sigma_{\mathbf{j}}^{z,+} f_{\mathbf{j}}^\dagger | v, \boldsymbol{\sigma}_{1,\tilde{b}} \rangle}{\langle v, \boldsymbol{\sigma}_{2,\tilde{b}} | e^{-\Delta\tau H_{\tilde{b}}} | v, \boldsymbol{\sigma}_{1,\tilde{b}} \rangle}. \end{aligned} \quad (10.74)$$

Omitting the bond index, the above quantity is given by

$$\begin{aligned} A(\boldsymbol{\sigma}_2 = \uparrow_{\mathbf{i}}, \uparrow_{\mathbf{j}}, \boldsymbol{\sigma}_1 = \uparrow_{\mathbf{i}}, \uparrow_{\mathbf{j}}) &= \begin{pmatrix} \cosh(-\Delta\tau t) & \sinh(-\Delta\tau t) \\ \sinh(-\Delta\tau t) & \cosh(-\Delta\tau t) \end{pmatrix}_{ij} \\ A(\boldsymbol{\sigma}_2 = \downarrow_{\mathbf{i}}, \downarrow_{\mathbf{j}}, \boldsymbol{\sigma}_1 = \downarrow_{\mathbf{i}}, \downarrow_{\mathbf{j}}) &= \begin{pmatrix} 0 & 0 \\ 0 & 0 \end{pmatrix}_{ij} \\ A(\boldsymbol{\sigma}_2 = \downarrow_{\mathbf{i}}, \uparrow_{\mathbf{j}}, \boldsymbol{\sigma}_1 = \downarrow_{\mathbf{i}}, \uparrow_{\mathbf{j}}) &= \begin{pmatrix} 0 & 0 \\ 0 & \frac{\cosh(-\Delta\tau t)}{e^{\Delta\tau J/2} \cosh(\Delta\tau J/2)} \end{pmatrix}_{ij} \\ A(\boldsymbol{\sigma}_2 = \uparrow_{\mathbf{i}}, \downarrow_{\mathbf{j}}, \boldsymbol{\sigma}_1 = \uparrow_{\mathbf{i}}, \downarrow_{\mathbf{j}}) &= \begin{pmatrix} \frac{\cosh(-\Delta\tau t)}{e^{\Delta\tau J/2} \cosh(\Delta\tau J/2)} & 0 \\ 0 & 0 \end{pmatrix}_{ij} \\ A(\boldsymbol{\sigma}_2 = \downarrow_{\mathbf{i}}, \uparrow_{\mathbf{j}}, \boldsymbol{\sigma}_1 = \uparrow_{\mathbf{i}}, \downarrow_{\mathbf{j}}) &= \begin{pmatrix} 0 & 0 \\ \frac{\sinh(-\Delta\tau t)}{-e^{\Delta\tau J/2} \sinh(\Delta\tau J/2)} & 0 \end{pmatrix}_{ij} \\ A(\boldsymbol{\sigma}_2 = \uparrow_{\mathbf{i}}, \downarrow_{\mathbf{j}}, \boldsymbol{\sigma}_1 = \downarrow_{\mathbf{i}}, \uparrow_{\mathbf{j}}) &= \begin{pmatrix} 0 & \frac{\sinh(-\Delta\tau t)}{-e^{\Delta\tau J/2} \sinh(\Delta\tau J/2)} \\ 0 & 0 \end{pmatrix}_{ij} \end{aligned} \quad (10.75)$$



AU: Please provide citation for Fig. 10.7.

Fig. 10.7. Graphical representation of the propagation of a hole in a given world-line or spin configuration. The *solid lines* denotes the possible routes taken by the hole through the spin configuration. One will notice that due to the constraint which inhibits the states $|0, \downarrow\rangle$ the hole motion tracks the up spins

With the above construction, a loop algorithm for a given non-frustrated spin system in arbitrary dimensions may be quickly generalized to tackle the important problem of single-hole dynamics in quantum magnets.

10.3 World-Line Representations without Discretization Error

The Trotter discretization of imaginary time which was used in the preceding section is conceptually easy. It was historically the first approach, but has some notable disadvantages:

- In order to obtain reliable results, one has to perform calculations at several different small values of $\Delta\tau$ and to extrapolate to $\Delta\tau = 0$.
- In practice, this extrapolation is often skipped, and instead a *small* value like $\Delta\tau = 1/32$ or $1/20$ (or even larger) is used, which implies unknown systematic discretization errors.
- Small values of $\Delta\tau$ imply a large number $L = \beta/\Delta\tau$ of time slices, so that the computer time needed for each sweep through the lattice increases like $1/\Delta\tau$. In addition, the correlation length in imaginary time, measured in time slices, grows like $1/\Delta\tau$, so that autocorrelation times for local algorithms typically grow with another factor of $(1/\Delta\tau)^2$.

Fortunately, it has been found in recent years, independently by a number of authors, that one can overcome the Trotter discretization error entirely. We will describe the most common representations: Continuous imaginary time and the stochastic series expansion.

Note that such representations of $\exp(-\beta H)$ are all world-line like. They are almost independent of the algorithm used to update the world-line configurations! That is, there are local and loop-updates both in imaginary time and in the SSE representation.

A number of other methods without time discretization errors have been developed in recent years in different contexts. See for example [8, 9, 19, 25, 26, 27, 28, 29] and Chaps. 12 and 11.

10.3.1 Limit of Continuous Time

In the context of QMC, it was first realized by Beard and Wiese [30] that the limit $\Delta\tau \rightarrow 0$ can be explicitly taken within the loop algorithm. Actually this applies to any model with a discrete state space, see Sect. 10.3.3. Let us look again at the isotropic Heisenberg AF, (10.1) with $J = J_z = J_x$. There are then only vertical and horizontal breakups in the loop algorithm.

To lowest order in $\Delta\tau$, the probability for a horizontal breakup is $J\Delta\tau/2$, proportional to $\Delta\tau$, and the probability for a vertical breakup is $1 - J\Delta\tau/2$. This is like a discrete Poisson process: The event of a horizontal breakup occurs with probability $J\Delta\tau/2$. Note that the vertical breakup does not change the world-line configuration; it is equivalent to the identity operator, see also Sect. 10.4. In the limit $\Delta\tau \rightarrow 0$ the Poisson process becomes a Poisson distribution in continuous imaginary time, with probability density $J/2$ for a horizontal breakup.

In continuous imaginary time there are no plaquettes anymore. Instead, configurations are specified by the space and time coordinates of the events, together with the local spin values. On average, there will be about one event per unit of βJ on each lattice bond. Therefore the storage requirements are reduced by $O(1/\Delta\tau)$! The events are best stored as linked lists, i.e. for each event on a bond there should be pointers to the events closest in imaginary time, for both sites of the bond.

Monte Carlo Loop updates are implemented quite differently for the multi-loop and for the single-loop variant, respectively. For multi-loop updates, i.e. the construction and flip of loops for every space-time site of the lattice, one first constructs a stochastic loop decomposition of the world-line configuration. To do so, horizontal breakups are put on the lattice with constant probability density in imaginary time for each bond, but only in time regions where they are compatible with the world-line configuration, i.e. where the spins are antiferromagnetic. Horizontal breakups must also be put wherever a world-line jumps to another site. The linked list has to be updated or reconstructed. The configuration of breakups is equivalent to a configuration of loops, obtained by vertically connecting the horizontal breakups (see Sect. 10.4). These implicitly given loops then have to be flipped with some constant probability, usually $1/2$. To do so, one can for example go to each stored event (breakup) and find, and possibly flip, the one or two loops through this breakup, unless these loop(s) have already been treated.

In single-loop-updates only one single loop is constructed and then always flipped. Here it is better to make the breakup-decisions during loop construction, see also Sect. 10.4.1). One starts at a randomly chosen space-time site (i, t_0) . The loop is constructed piece by piece. It thus has a tail and a moving head. The partial loop can be called a worm (cf. Sect. 10.4.5). The loop points into the present spin-direction, say upwards in time.

For each lattice bond $\langle ij \rangle$ at the present site, the smallest of the following times is determined:

- (i) The time at which the neighboring spin changes;
- (ii) If the bond is antiferromagnetic, the present time t_0 plus a decay time generated with uniform probability density;
- (iii) The time at which the spin at site i changes.

The loop head is moved to the smallest of all these times, t_1 . Existing breakups between t_0 and t_1 are removed. If t_1 corresponds to case (ii) or (i), a breakup is inserted there, and the loop head follows it, i.e. it moves to the neighboring site and changes direction in imaginary time. Then the construction described in the present paragraph repeats.

It finishes when the loop has closed. All spins along the loop can then be flipped.

10.3.2 Stochastic Series Expansion (SSE)

The stochastic series expansion (SSE), invented by A. Sandvik [31, 32, 33] is another representation of $\exp(-\beta H)$ without discretization error. Note that it is *not* directly connected to any particular MC-update. Any update method can (with some adjustments) be applied either in imaginary time or in the SSE representation.

Let the Hamiltonian be a sum of operators defined on lattice bonds

$$H = - \sum_b^{m_b} H_b \quad (10.76)$$

like in the nearest-neighbor Heisenberg model. The operators H_b need to be non-branching, in some basis, i.e. for each basis state $|i\rangle$, $H_b|i\rangle$ is proportional to a single basis state. All diagonal matrix elements of these operators need to be positive in order to avoid a sign problem. For the XXZ Heisenberg model one can for example use the bond operators $(S_i^+ S_j^- + S_i^- S_j^+)/2$ and $1/4 - S_i^z S_j^z$ for each bond $\langle ij \rangle$. We write the series expansion

$$\begin{aligned} \exp(-\beta H) &= \sum_n \frac{\beta^n}{n!} (-H)^n \\ &= \sum_n \frac{\beta^n}{n!} (H_1 + H_2 + \dots)(H_1 + H_2 + \dots) \dots \\ &= \sum_n \frac{\beta^n}{n!} \sum_{S_n} H_{i_1} H_{i_2} H_{i_3} \dots, \end{aligned}$$

where \sum_{S_n} extends over all sequences (i_1, i_2, \dots, i_n) of indices $i_\alpha \in \{1, 2, \dots, m_b\}$ labelling the operators H_b . When we compute the trace $\text{Tr}[\exp(-\beta H)] = \sum_i \langle i | \exp(-\beta H) | i \rangle$, the initial state $|i\rangle$ is modified in turn by each of the H_b , each time resulting in another basis state. For the XXZ-model and spin- S^z basis states, a world-line like configuration results again, but with a discrete timelike index

$\alpha = 1, 2, \dots, n$, and only one event per value of the index. The remaining matrix elements can be evaluated easily. With suitable normalizations of the operators H_b , they can usually be made to be one. They are zero for operator configurations which are not possible, e.g. not compatible with periodic world lines, which will thus not be produced in the Monte Carlo. Spins at sites not connected by any operator to other sites can be summed immediately.

Note that, in contrast to imaginary time, now *diagonal* operators $S_i^z S_j^z$ occur explicitly, since the exponential factor weighing neighboring world lines has also been expanded in a power series. Thus, SSE needs more operators on average than imaginary time for a given accuracy.

The average length $\langle n \rangle$ of the operator sequence is β times the average total energy (as can be seen from $\partial \log Z / \partial \beta$) and its variance is related to the specific heat. Therefore in any finite length simulation, only a finite value of n of order $\beta \langle -H \rangle$ will occur, so that we get results without discretization error, despite the finiteness of n .

It is convenient to pad the sum in (10.77) with unit operators $\mathbf{1}$ in order to have an operator string of constant length N . For details see [31, 32, 33].

Updates in the SSE representation usually proceed in two steps. First, a diagonal update is performed, for which a switch between diagonal parts of the Hamiltonian, e.g. $S_i^z S_j^z$, and unit operators $\mathbf{1}$ is proposed. This kind of update does not change the shape of world lines. Second, non-diagonal updates are proposed, e.g. local updates analogous to the local updates of world lines in imaginary time, see Sect. 10.2. Loop updates are somewhat different, see Sect. 10.4.

10.3.3 Unified Picture: Interaction Representation

All previous representations, namely discrete and continuous imaginary time, as well as SSE, follow easily from the interaction representation of $\exp(-\beta H)$ [5, 16, 34, 35, 36, 37].

Let $H = H_0 - V$ with H_0 diagonal in the chosen basis. Then the interaction representation is

$$Z = \text{Tr} \sum_{n=0}^{\infty} e^{(-\beta H_0)} \int_0^{\beta} d\tau_n \dots \int_0^{\tau_3} d\tau_2 \int_0^{\tau_2} d\tau_1 V(\tau_1) \dots V(\tau_n), \quad (10.77)$$

where $V(\tau) = \exp(H_0 \tau) V \exp(-H_0 \tau)$. When the system size and β are finite, this is a convergent expansion.

Indeed, in the form of (10.77), this is already the continuous imaginary time representation of $\exp(-\beta H)$! When the time integrals are approximated by discrete sums, then the discrete time representation results.

The SSE representation can be obtained in the special case that one chooses $H_0 = 0$ and $V = -H = \sum_b^{m_b} H_b$. Then $H(\tau)$ does not depend on τ and the time integrals can be performed

$$\int_0^\beta d\tau_n \dots \int_0^{\tau_2} d\tau_1 = \frac{\beta^n}{n!} \quad (10.78)$$

and we end up with the *ordered* sequence of operators $H_1 \dots H_n$ of the SSE representation.

This unified picture has turned out to be very useful [7], by providing a stochastic mapping between SSE and continuous time. Starting with a continuous time configuration, one can just drop the specific times of operators to get to an SSE configuration. Starting with an SSE configuration of n ordered operators, one can draw n times between zero and β uniformly at random, sort them, and assign them to the operators, keeping their order intact. This mapping is useful in order to measure dynamical Greens functions during a simulation that uses the SSE representation. In SSE such a measurement is very costly [38], while in imaginary time it can be done efficiently with FFT.

Interestingly, for the usual representation of the Heisenberg model (10.10)

$$H_{ij} = \frac{1}{2} (S_i^+ S_j^- + S_i^- S_j^+) + S_i^z S_j^z, \quad (10.79)$$

the interaction representation immediately provides the continuous time limit of the discrete time world-line representation, independently of any loops.

One can see the essence of the continuous time limit by looking at the exponential of some operator O with a finite discrete spectrum (state space)

$$\begin{aligned} e^{-\beta(1-JO)} &= \left(e^{(JO-1)\Delta\tau} \right)^{\beta/\Delta\tau} \\ &= \lim_{\Delta\tau \rightarrow 0} \left((1 - \Delta\tau)\mathbf{1} + \Delta\tau JO \right)^{\beta/\Delta\tau} \end{aligned} \quad (10.80)$$

The term in brackets can be interpreted as a Poisson process: With probability $\Delta\tau J$ choose O , else choose $\mathbf{1}$. Its limit $\Delta\tau \rightarrow 0$ is a Poisson distribution in continuous imaginary time, i.e. the operator O occurs with a constant probability density J in imaginary time.

10.4 Loop Operator Representation of the Heisenberg Model

At the root of the loop algorithm there is a representation of the model in terms of loop-operators [4], akin to the Fortuin-Kasteleyn representation of the Ising model [39, 40], and analogous to the Swendsen-Wang algorithm [41, 42], see also Chap. 4. The bond operator of the spin 1/2 Heisenberg antiferromagnet, with a suitable constant added, is a singlet projection operator

$$-S_i S_j + \frac{1}{4} = \frac{1}{\sqrt{2}} (|\uparrow\downarrow\rangle - |\downarrow\uparrow\rangle) \frac{1}{\sqrt{2}} (\langle\uparrow\downarrow| - \langle\downarrow\uparrow|). \quad (10.81)$$

On a bipartite lattice, the minus signs can be removed by rotating $S^{x,y} \rightarrow -S^{x,y}$ on one of the two sublattices. We now denote the operator (10.81) pictorially in terms of

contributing spin-configurations, as an operator acting towards a spin configuration at the bottom and producing a new spin configuration on the top. There are four contributing configurations

$$\begin{aligned}
 -S_i S_j + \frac{1}{4} &= \frac{1}{2} \left(\begin{array}{c} \frown \\ \smile \end{array} + \begin{array}{c} \smile \\ \frown \end{array} + \begin{array}{c} \frown \\ \frown \end{array} + \begin{array}{c} \smile \\ \smile \end{array} \right) \\
 &=: \frac{1}{2} \begin{array}{c} \smile \\ \frown \end{array} .
 \end{aligned}
 \tag{10.82}$$

These are just the configurations compatible with the horizontal breakup of the loop algorithm. The horizontal breakup can thus be interpreted as an operator projecting onto a spin singlet. The partition function of the Heisenberg model is then

$$Z = \text{Tr} e^{-\beta H} \sim \text{Tr} e^{\beta J \sum_{\langle ij \rangle} \frac{1}{2}} . \tag{10.82}$$

From (10.77) or (10.80) we see that $\exp(-\beta H)$ then corresponds to a Poisson distribution of horizontal breakups (singlet projection operators) with density $J/2$ in imaginary time, on each lattice bond. One instance of such a distribution is shown in Fig. 10.8 on the left.

Taking the trace means to sum over all spin states on the bottom, with periodic boundary conditions in imaginary time. Between operators, the spin states cannot change. The operators can therefore be connected by lines, on which the spin direction does not change. The operator configuration, see Fig. 10.8 (left), therefore implies a configuration of loops, Fig. 10.8 (middle left). A horizontal breakup stands for a sum over two spin directions on each of its half-circles. On each loop the spin direction stays constant along the lines. Thus each loop contributes two states to the partition function. We arrive at the loop representation of the Heisenberg antiferromagnet [4, 43, 44]

$$Z = \int_0^\beta \left(\text{Poisson distribution of horizontal breakups with density } J/2 \right)^{\text{number of loops}} . \tag{10.83}$$

The loop-algorithm moves back and forth between the world-line representation and the operator representation. From a loop (-operator) configuration we get to a

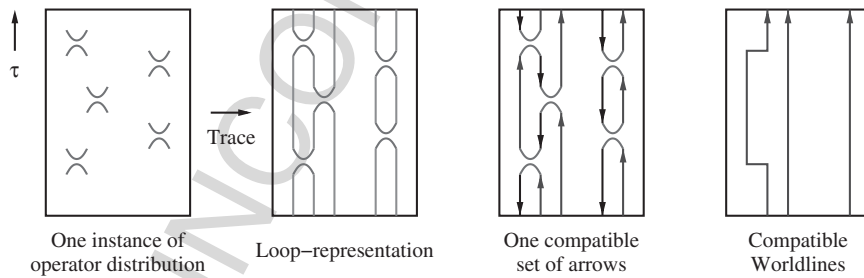


Fig. 10.8. Loop operator representation of the Heisenberg model and of the loop algorithm

compatible world-line configuration by choosing one direction for each loop, see Fig. 10.8 (middle right and right). We get back to a new operator configuration by choosing one with Poisson probability, and with the constraint that it must be compatible to the current world-line configuration (i.e. operators can only appear where world lines are antiferromagnetic, and they must appear where a world-line jumps).

In the SSE representation, loop updates require only the so-called diagonal update, namely a switch between unit operators and breakups. Once the breakups are defined, the loops just have to be found and flipped. Since there is no second stochastic non-diagonal update step, this has been called, somewhat misleading, a deterministic loop update [45, 46].

10.4.1 Single Loop Updates

An alternative to the multi-loop method just sketched is to construct and flip only a single loop at a time. This is also a valid Monte Carlo method. One could imagine that all breakups and thus all loops were actually constructed, but only a single one of them flipped, see also Sect. 10.3.1. For each update, one starts with a randomly chosen space-time site and follows the spin arrow direction from there. One then constructs just the one loop to which this spin belongs, performing the breakup-decisions on the fly, i.e. the decisions on whether to move vertically in time or to put a horizontal breakup on a neighboring bond and to move there. During this construction, or afterwards, all spins on the loop are flipped. Note that the insertion of a horizontal breakup (Heisenberg spin singlet projection operator) at some place (plaquette in case of discrete time) already determines the path of the loop when and if it should return to the same place again: Either it completes then, or it will take the other half-circle of the horizontal breakup. This behavior is different from the worms and directed loops discussed later.

On average, a single loop constructed this way will be bigger than in the multi-loop variant, since the initial site will on average be more likely on a big loop than on a small one. This usually results in smaller autocorrelation times.

10.4.2 Projector Monte Carlo in Valence Bond Basis

The fact that a horizontal breakup is a singlet projection operator is also at the root of a recent efficient Projector Monte Carlo method [47] for the Heisenberg model. Indeed, a cut through a loop configuration, see Fig. 10.8 (middle left) at some imaginary time τ provides a spin state in which each pair of sites that belongs to the same loop is in a spin singlet state.

In the limit of large enough projection time and on a bipartite lattice, all sites will be in such a singlet with probability one. The state is then called an RVB state (resonating valence bond). This is an alternative way to see the famous Lieb-Mattis theorem, namely that the ground state of the Heisenberg antiferromagnet is a global spin singlet.

When one wants to investigate only the ground state, it is sufficient to restrict configurations to an RVB basis, also called valence bond basis [47].

10.4.3 Improved Estimators

The spin directions on different loops are independent. Therefore the contribution of a given loop configuration to the spin Greens function $\langle S^z(x, t) S^z(x', t') \rangle$ averages to zero when (x, t) and (x', t') are on different loops, whereas it gets four identical contributions when they are on the same loop [4]. Thus this Greens function can be measured within the loop representation, and it is particularly simple there. At momentum π , this Greens function only takes the values zero and one: It is one when (x, t) and (x', t') are on the same loop, and zero otherwise. Thus its variance is smaller than that of $S^z(x, t) S^z(x', t')$ in spin representation, which takes values $+1$ and -1 . Observables in loop representation such as this Greens function are therefore called improved estimators.

We also see that the Greens function corresponds directly to the space-time size of the loops: These are the physically correlated objects of the model, in the same sense that Fortuin-Kasteleyn clusters are the physically correlated objects of the Ising model [39, 40, 42].

In the loop representation one can also easily measure the off-diagonal Greens function $\langle S^+(x, t) S^-(x', t') \rangle$. It is virtually inaccessible in the spin world-line representation with standard local updates, since contributing configurations would require partial world lines, which do not occur there. However, in loop representation, $S^+(x, t) S^-(x', t')$ does get a contribution whenever (x, t) and (x', t') are located on the same loop [4]. For the spin-isotropic Heisenberg model, the estimator in loop representation is identical to that of the diagonal correlation function $\langle S^z(x, t) S^z(x', t') \rangle$.

10.4.4 Simulations on Infinite Size Lattice

One intriguing application of improved estimators is the possibility to do simulations on an *infinite* size lattice and/or at zero temperature whenever $\langle S(x, t) S^z(x', t') \rangle$ goes to zero at infinite distance in space and/or imaginary time, i.e. in an unbroken phase [48].

The idea is to perform single-loop-updates, all starting at the same space-time site (the origin) instead of at a random point. The lattice of spins is assumed to be infinite in size, but only a finite portion will be needed.

Since the correlation functions go to zero, the size of each single loop will be finite. For a correlation length ξ and gap Δ it will reach spatial distances r with probability $\sim \exp(-r/\xi)$ and temporal distances τ with probability $\sim \exp(-\tau\Delta)$. The maximum distance reached will therefore be finite for any finite number of loops constructed. With each loop flip, the spin configuration is updated. It will eventually equilibrate in the region of space-time that was visited by loops often enough. The updated region is sketched schematically in Fig. 10.9. Since there is no boundary to this region, the physics of the infinite size lattice is simulated. Its properties can be measured in this region, especially the two-point Greens function, which is directly available from the loops.

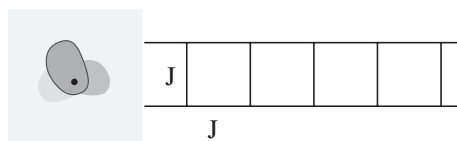


Fig. 10.9. **Left:** Sketch of regions updated with subsequent loops on an infinite lattice. **Right:** Heisenberg spin ladder with two legs

As an example, let us look at simulations of a Heisenberg spin ladder with $N = 2$ and with $N = 4$ legs, illustrated in Fig. 10.9. The behavior of the infinite size system usually has to be extracted by finite-size scaling from results like those for $L = 10$ and $L = 20$ in Fig. 10.10. Here they result directly, with an effort that here amounted to a few hours on a workstation, similar to a finite lattice simulation at $L = 40$. The asymptotic behavior is exponential, with a correlation length that can directly be measured from the Greens function with high precision.

Similarly, one can measure Greens functions in imaginary time, illustrated in Fig. 10.11, and directly extract the spin gap with high precision from a linear fit to $\log G(q = \pi, \tau)$. The Greens function can be translated to real frequency with the Maximum Entropy technique, resulting in the spectrum shown in Fig. 10.11 on the right.

10.4.5 Worms and Directed Loops

A generalization of single loop updates is provided by worms and directed loops [5, 14, 15, 16, 17, 35]. They are applicable to any model with a world-line like representation. At the same time, they are not cluster algorithms, so that objects like improved estimators are not available.

A single loop (or worm) is constructed iteratively in space-time. The worm-head is a priori allowed to move in any direction, including back-tracking. Each proposal for such a move is accepted or rejected with (e.g.) Metropolis probability. Thus only local updates are needed.

In contrast to the single-loop update of the loop-algorithm, the movement of the worm-head is not determined by previous decisions when it crosses its own track.

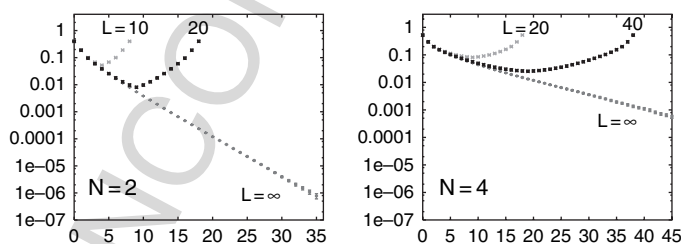


Fig. 10.10. Spatial correlation function of Heisenberg ladders at $\beta = \infty$, for finite systems of finite L and, independently, of $L = \infty$

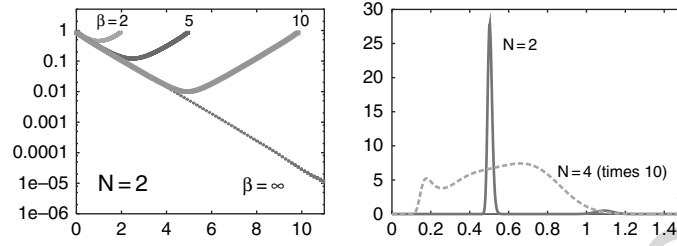


Fig. 10.11. **Left:** Temporal correlation function (Greens function) of Heisenberg ladders at $L = \infty$, at finite inverse temperatures $\beta = 2, 5, 10$ and, independently, at $\beta = \infty$. **Right:** Real frequency spectrum obtained by Maximum Entropy continuation

The worm algorithm and directed loops differ in details of the updates. Note that, like the loop-algorithm, they also allow the measurement of off-diagonal two-point functions and the change of topological quantum numbers like the number of particles or the spatial winding. In a suitably chosen version of directed loops, single-loop updates of the loop algorithm become a special case. For more information on worms and directed loops we refer to [5, 14, 15, 16, 17, 35].

10.5 Spin-Phonon Simulations

As an example of world-line Monte Carlo calculations we shall discuss recent investigations of the spin-Peierls transition in 1D [7]. Our discussion will also include a new way to simulate phonons which is suitable for any bare phonon dispersion $\omega(q)$.

The model consists of an 1D Heisenberg chain coupled to phonons

$$\begin{aligned}
 H = J \sum_{i=1}^N \mathbf{S}_i \mathbf{S}_{i+1} & \underbrace{\left\{ \begin{array}{l} 1+g \quad x_i \quad \text{bond phonons} \\ 1+g(x_i - x_{i+1}) \quad \text{site phonons} \end{array} \right\}}_{f(\{x_i\})} \\
 + \underbrace{\frac{1}{2} \sum_q p_q^2 + \omega^2(q) x_q^2}_{H_{\text{ph}}} . & \quad (10.84)
 \end{aligned}$$

At $T = 0$ there is a quantum phase transition of the Kosterlitz-Thouless type at a critical coupling g_c to a dimerized phase. In this phase the spin-interaction $\mathbf{S}_i \mathbf{S}_{i+1}$ as well as the phonon coordinate x_i (resp. $x_i - x_{i+1}$) is larger on every second lattice bond, and a spin-gap develops, initially exponentially small [36, 37, 49].

Some of the interesting issues are, see Fig. 10.12:

- (i) Does g_c depend on the bare phonon dispersion $\omega(q)$?
- (ii) Is the phonon spectrum beyond the transition softened (i.e. the bare phonon spectrum moves to lower frequency, down to zero at momentum π), or does it have a separate central peak?

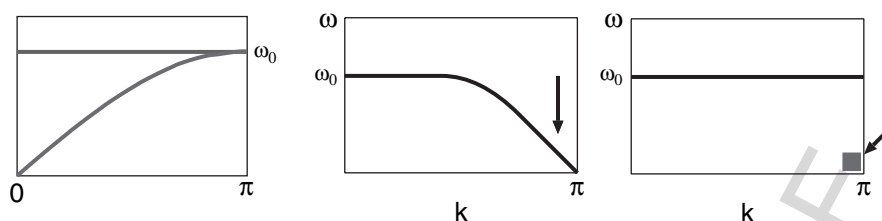


Fig. 10.12. Issues for the spin-Peierls transition. **Left:** Einstein (optical) and acoustical bare phonon dispersions. **Middle:** Softening scenario. **Right:** Central peak scenario

10.5.1 Bond Phonons with Einstein Dispersion $\omega(q) = \omega_0$

These phonons are the easiest to treat by QMC. In order to make the quantum phonons amenable to numerical treatment, one can express them with the basic Feynman path integral for each x_i (see Chap. 11), by introducing discrete Trotter times τ_j , inserting complete sets of states $x_i(\tau_j)$ and evaluating the resulting matrix elements to $O(\Delta\tau)$. A simple QMC for the phonon degrees of freedom can then be done with local updates of the phonon world lines $x_i(\tau)$.

A similar approach is possible in second quantization, by inserting complete sets of occupation number eigenstates $n_i(\tau_j)$ at the Trotter times τ_j . Again, one can perform QMC with local updates on the occupation number states [36, 37]. The discrete Trotter time can be avoided here, either with continuous time or with SSE [31, 32, 33].

Such local updates suffer from the usual difficulties of long autocorrelation times, which occur especially close to and beyond the phase transition. They can be alleviated by using parallel tempering [50, 51] (or simulated tempering [52]) (see Chap. 4). In this approach, simulations at many different couplings g (originally: at many temperatures) are run in parallel. Occasionally, a swap of configurations at neighboring g is proposed. It is accepted with Metropolis probability. The goal of this strategy is to have approximately a random walk of configurations in the space of couplings g . Configurations at high g can then equilibrate by first moving to low g , where the Monte Carlo is efficient, and then back to high g . The proper choice of couplings (and of re-weighting factors in case of simulated tempering) depends on the physics of the system and is sometimes cumbersome. It can, however, be automated [7] efficiently by measuring the distributions of energies during an initial run.

The results discussed below were obtained using loop updates for spins and local updates in second quantization for phonons, in SSE representation, similar to [36, 37], with additional automated tempering. Spectra were obtained by mapping the SSE configurations to continuous imaginary time, as explained in Sect. 10.3.3, and measuring Greens functions there using FFT.

The location of the phase transition is best determined through the finite size dependence of a staggered susceptibility, of spins, spin-dimers, of phonons. For spins it reads

$$\chi_S(\pi) = \frac{1}{N} \sum_{n,m} (-1)^m \int_0^\beta d\tau \langle S_n^z(\tau) S_{n+m}^z(0) \rangle . \quad (10.85)$$

At the phase transition, $\chi_S(\pi)$ is directly proportional to the system size N , whereas above g_c there are additional logarithmic corrections. Below g_c it is proportional to $\ln N$ for any $g > 0$, i.e. there is a non-extensive central peak in the phonon spectrum for any finite spin-phonon coupling.

The phonon spectra exhibit drastic changes at the phase transition. Figure 10.13 shows that the value of ω_0 determines their qualitative behavior: At $\omega_0 = J$ the central peak becomes extensive and develops a linear branch at the phase transition, which shows the spin-wave velocity. At $\omega_0 = 0.25J$ the behavior is completely different: The bare Einstein dispersion has softened and has joined the previously non-extensive central peak. Thus both the central peak scenario and the softening scenario occur, depending on the size of ω_0 .

Note that large system sizes and low temperature are essential to get the correct spectra. The finite size gap of a finite system is of order $1/N$. When $1/N$ is larger than about $\omega_0/10$ (!), then there are drastic finite size effects in the phonon spectrum [7].

At very large values of g , the spin gap Δ_S becomes sizeable. The system enters an adiabatic regime when $\Delta_S > O(\omega_0)$ [49]. For the couplings investigated here, it is always diabatic.

AU: We have deleted “check?” at the end of the sentence “For the couplings ...”. Please check it is ok.

10.5.2 Phonons with arbitrary dispersion $\omega(q)$

Phonons other than those treated in Sect. 10.5.1 have in the past posed great difficulties for QMC. Site phonons have a coupling

$$(1 + g(x_i - x_{i+1})) S_i S_{i+1} , \quad (10.86)$$

which implies a zero-mode at momentum $q = 0$. Simulations with local updates for such phonons are extremely slow. In second quantization, simulations appear

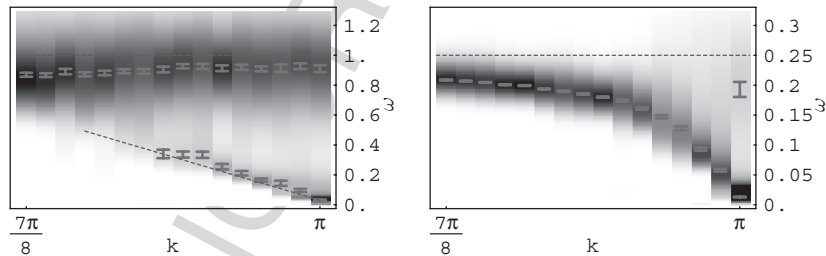


Fig. 10.13. Spectra of phonon coordinates x_i above the phase transition for bond phonons. **Left:** $\omega_0 = 1 J$, just above the phase transition. **Right:** $\omega_0 = 0.25 J$ at $g = 0.3 > g_c \simeq 0.23$. Lattice size $L = 256$ and $\beta = 512$

impossible, since the difference-coupling induces a sign problem! For arbitrary dispersions, there has been a lack of efficient methods.

Let us now discuss a new method [7] which overcomes all these difficulties. We use the interaction representation with the pure phonon Hamiltonian as the diagonal part and the spin interaction (10.86) as the interaction part which is expanded. The partition function then reads

$$Z = \text{Tr}_s \sum_{n=0}^{\infty} \sum_S \int_0^{\beta} d\tau_n \dots \int_0^{\tau_2} d\tau_1 \int \mathcal{D}x \underbrace{\prod_{l=0}^n f(\{x_l\}) S[l]}_{\text{spin operator sequence}} \underbrace{e^{-\int_0^{\beta} d\tau H_{\text{ph}}(\{x(\tau)\})}}_{\text{phonon path integral}}. \quad (10.87)$$

Here $S[l]$ is a spin operator like $\mathbf{S}_i \mathbf{S}_{i+1}$. The spin-phonon coupling $f(\{x(\tau)\})$ is to be evaluated at the space-time location where the spin operators act.

For a given sequence of spin operators we now construct a Monte Carlo phonon update. The effective action S_{eff} for the phonons contains $\log(f(\{x(\tau)\}))$. It is therefore not bilinear and cannot be integrated directly. However, for purposes of a Monte Carlo update, we can pretend for a moment that the coupling was $f^{\text{prop}}(x) := \exp(gx)$ instead of $f(x) = 1 + gx$. Then $S_{\text{eff}}^{\text{prop}}$ is bilinear. For a given sequence of spin operators, we can diagonalize $S_{\text{eff}}^{\text{prop}}$ in momentum space and Matsubara frequencies. The result are independent Gaussian distributions of phonon coordinates in the diagonalized basis. We can then generate a new, completely independent phonon configuration by taking one sample from this distribution. In order to achieve a correct Monte Carlo update for the actual model, we take this sample as a Monte Carlo proposal and accept or reject it with Metropolis probability for the actual model, see (10.87).

The acceptance probability will depend on the difference between S_{eff} and $S_{\text{eff}}^{\text{prop}}$, and thus on the typical phonon extensions. In order to achieve high acceptance rates it is advantageous to change phonon configurations only in part of the complete (q, ω_n) space for each update proposal. These parts need to be smaller close to the physically important region ($q = \pi, \omega = 0$).

Given a phonon-configuration, the effective model for the spins is a Heisenberg antiferromagnet with couplings that vary in space-time. It can be simulated efficiently with the loop-algorithm, modified for the fact that probabilities are now not constant in imaginary time, but depend on the phonon coordinates.

The approach just sketched works for site phonons as well as for bond phonons. Remarkably, any bare phonon dispersion $\omega(q)$ can be used, since it just appears in the Gaussian effective phonon action. Measurements of phonon properties are easy, since the configurations are directly available in (q, ω_n) space.

Let us now briefly discuss some recent results [7] for site phonons. Their bare dispersion is acoustical, i.e. gapless at $q = 0$. In a recent letter [53] it was concluded that for this model, the critical coupling is $g_c = 0$, i.e. the system supposedly orders at any finite coupling. However, it turns out that this conclusion was based on an incorrect scaling assumption [7].

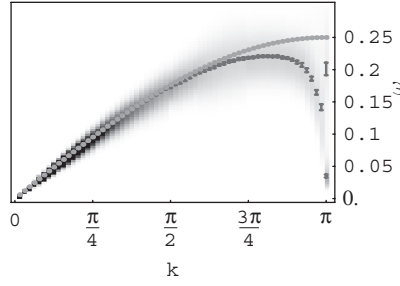


Fig. 10.14. Spectrum of phonon coordinates x_i for acoustical site phonons, at the phase transition

QMC examination of the spin susceptibility $\chi_S(\pi)$ on lattices up to length 256 revealed that the critical coupling is actually finite, and almost identical to that of dispersionless bond phonons with the same $\omega_0(\pi)$.

The phonon dispersion slightly above the phase transition is shown, together with the bare dispersion, in Fig. 10.14.

One can see clearly that in this case of small $\omega_0(\pi) = 0.25J$ there is again phonon softening. The spin-Peierls phase transition only affects phonons with momenta close to π . The soft bare dispersion at $q = 0$ is not affected at all. Indeed, the bare dispersion at small momenta has no influence on the phase transition [7].

10.6 Auxiliary Field Quantum Monte Carlo Methods

In the present and following sections, we will review the basic concepts involved in the formulation of various forms of auxiliary field QMC algorithms for fermionic systems. Auxiliary field methods are based on a Hubbard-Stratonovich (HS) decomposition of the two-body interaction term thereby yielding a functional integral expression

$$\text{Tr} \left[e^{-\beta(H-\mu N)} \right] = \int d\Phi(i, \tau) e^{-S[\Phi(i, \tau)]} \quad (10.88)$$

for the partition function. Here, i runs over all lattice sites and τ from 0 to β . For a fixed HS field $\Phi(i, \tau)$, one has to compute the action $S[\Phi(i, \tau)]$, corresponding to a problem of non-interacting electrons in an external space and imaginary time dependent field. The required computational effort depends on the formulation of the algorithm. In the Blankenbecler-Scalapino-Sugar (BSS) [6] approach for lattice models such as the Hubbard Hamiltonian, it scales as βN^3 where N corresponds to the number of lattice sites. In the Hirsch-Fye approach [54], appropriate for impurity problems it scales as $(\beta N_{\text{imp}})^3$ where N_{imp} corresponds to the number of correlated sites. Having solved for a fixed HS field, we have to sum over all possible fields. This is done stochastically with the Monte Carlo method.

In comparison to the loop and SSE approaches, auxiliary field methods are slow. Recall that the computational effort for loop and SSE approaches – in the absence

of a sign problem – scales as $N\beta$. However, the attractive point of the auxiliary field approach lies in the fact that the sign problem is absent in many non-trivial cases where the loop and SSE methods fail.

10.6.1 Basic Formulation

For simplicity, we will concentrate on the Hubbard model. Applications to different models such as the Kondo lattice or $SU(N)$ Hubbard Heisenberg models can be found in [55, 56]. The Hubbard model we consider reads

$$H = H_t + H_U \quad (10.89)$$

with $H_t = -t \sum_{\langle i,j \rangle, \sigma} c_{i,\sigma}^\dagger c_{j,\sigma}$ and $H_U = U \sum_i (n_{i,\uparrow} - 1/2)(n_{i,\downarrow} - 1/2)$.

If one is interested in ground-state properties, it is convenient to use the projector quantum Monte Carlo (PQMC) algorithm [57, 58, 59]. The ground-state expectation value of an observable O is obtained by projecting a trial wave function $|\Psi_T\rangle$ along the imaginary time axis

$$\frac{\langle \Psi_0 | O | \Psi_0 \rangle}{\langle \Psi_0 | \Psi_0 \rangle} = \lim_{\Theta \rightarrow \infty} \frac{\langle \Psi_T | e^{-\Theta H} O e^{-\Theta H} | \Psi_T \rangle}{\langle \Psi_T | e^{-2\Theta H} | \Psi_T \rangle}. \quad (10.90)$$

The above equation is readily verified by writing $|\Psi_T\rangle = \sum_n |\Psi_n\rangle \langle \Psi_n | \Psi_0 \rangle$ with $H |\Psi_n\rangle = E_n |\Psi_n\rangle$. Under the assumptions that $\langle \Psi_T | \Psi_0 \rangle \neq 0$ and that the ground state is non-degenerate the right hand side of the above equation reads:

$$\lim_{\Theta \rightarrow \infty} \frac{\sum_{n,m} \langle \Psi_T | \Psi_n \rangle \langle \Psi_m | \Psi_T \rangle e^{-\Theta(E_n - E_m - 2E_0)} \langle \Psi_n | O | \Psi_m \rangle}{\sum_n |\langle \Psi_T | \Psi_n \rangle|^2 e^{-2\Theta(E_n - E_0)}} = \frac{\langle \Psi_0 | O | \Psi_0 \rangle}{\langle \Psi_0 | \Psi_0 \rangle}. \quad (10.91)$$

Finite-temperature properties in the grand-canonical ensemble are obtained by evaluating

$$\langle O \rangle = \frac{\text{Tr} [e^{-\beta(H - \mu N)} O]}{\text{Tr} [e^{-\beta(H - \mu N)}]}, \quad (10.92)$$

where the trace runs over the Fock space and μ is the chemical potential. The algorithm based on (10.92) will be referred to as finite-temperature QMC (FTQMC) method [60, 61]. Comparison of both algorithms is shown in Fig. 10.15 for the Hubbard model. At half-filling, the ground state is insulating so that charge fluctuations are absent in the low temperature limit on finite lattices. Hence, in this limit both grand-canonical and canonical approaches yield identical results. It is however clear that if one is interested solely in ground-state properties the PQMC is more efficient. This lies in the choice of the trial wave function which is chosen to be a spin singlet.

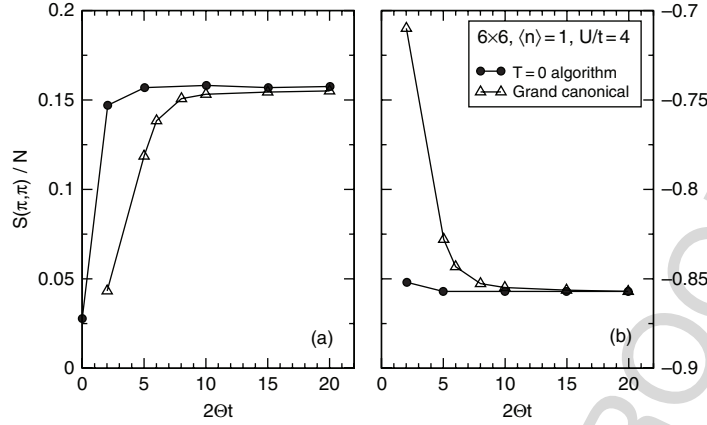


Fig. 10.15. Fourier transform of the spin-spin correlation functions at $Q = (\pi, \pi)$ (a) and energy (b) for the half-filled Hubbard model (10.89). \bullet : PQMC algorithm. \triangle : FTQMC algorithm at $\beta = 2\Theta$

10.6.2 Formulation of the Partition Function

In the world-line approach, one uses the Trotter decomposition (see App. 10.A) to split the Hamiltonian into a set of two-site problems. In the auxiliary field approach, we use the Trotter decomposition to separate the single-body Hamiltonian H_0 from the two-body interaction term in the imaginary time propagation

$$Z = \text{Tr} \left[e^{-\beta(H-\mu N)} \right] = \text{Tr} \left[\left(e^{-\Delta_\tau H_U} e^{-\Delta_\tau H_t} \right)^m \right] + \mathcal{O}(\Delta_\tau^2), \quad (10.93)$$

where we have included the chemical potential in a redefinition of H_t . In the above $m\Delta_\tau = \beta$, and the systematic error of order Δ_τ^2 will be omitted in the following. At each infinitesimal time step, we use the HS decomposition of (10.235) (see App. 10.B) to decouple the Hubbard interaction

$$e^{-\Delta_\tau U \sum_i (n_{i,\uparrow} - 1/2)(n_{i,\downarrow} - 1/2)} = C \sum_{s_1, \dots, s_N = \pm 1} e^{\alpha \sum_i s_i (n_{i,\uparrow} - n_{i,\downarrow})}. \quad (10.94)$$

where $\cosh(\alpha) = \exp(\Delta_\tau U/2)$ and on an N -site lattice, the constant $C = \exp(\Delta_\tau U N/4) / 2^N$.

To simplify the notation we introduce the index $x = (i, \sigma)$ to define

$$\begin{aligned} H_t &= \sum_{x,y} c_x^\dagger T_{x,y} c_y \equiv \mathbf{c}^\dagger T \mathbf{c}, \\ \alpha \sum_i s_i (n_{i,\uparrow} - n_{i,\downarrow}) &= \sum_{x,y} c_x^\dagger V(\mathbf{s})_{x,y} c_y \equiv \mathbf{c}^\dagger V(\mathbf{s}) \mathbf{c}. \end{aligned} \quad (10.95)$$

We will furthermore define the imaginary time propagators

$$\begin{aligned} U_{\mathbf{s}}(\tau_2, \tau_1) &= \prod_{n=n_1+1}^{n_2} e^{c^\dagger V(s_n) c} e^{-\Delta_\tau c^\dagger T c}, \\ B_{\mathbf{s}}(\tau_2, \tau_1) &= \prod_{n=n_1+1}^{n_2} e^{V(s_n)} e^{-\Delta_\tau T}, \end{aligned} \quad (10.96)$$

where $n_1 \Delta_\tau = \tau_1$ and $n_2 \Delta_\tau = \tau_2$.

Using the results of App. 10.C we can now write the partition function as

$$Z = C^m \sum_{\mathbf{s}_1, \dots, \mathbf{s}_m} \text{Tr} [U_{\mathbf{s}}(\beta, 0)] = C^m \sum_{\mathbf{s}_1, \dots, \mathbf{s}_m} \det [1 + B_{\mathbf{s}}(\beta, 0)]. \quad (10.97)$$

For the PQMC algorithm, we will require the trial wave function to be a Slater determinant characterized by the rectangular matrix P (see App. 10.C)

$$|\Psi_T\rangle = \prod_{y=1}^{N_p} \left(\sum_x c_x^\dagger P_{x,y} \right) |0\rangle = \prod_{y=1}^{N_p} (c^\dagger P)_y |0\rangle. \quad (10.98)$$

Hence,

$$\langle \Psi_T | e^{-2\Theta H} | \Psi_T \rangle = C^m \sum_{\mathbf{s}_1, \dots, \mathbf{s}_m} \det [P^\dagger B_{\mathbf{s}}(2\Theta, 0) P], \quad (10.99)$$

where for the PQMC $m \Delta_\tau = 2\Theta$.

10.6.3 Observables and Wick's Theorem

One of the big advantages of the auxiliary field approach is the ability of measuring arbitrary observables. This is based on the fact that for a given Hubbard-Stratonovich field we have to solve a problem of non-interacting fermions subject to this time and space dependent field. This leads to the validity of Wick's theorem. In this section, we will concentrate on equal-time observables, show how to compute Green functions, and finally demonstrate the validity of Wick's theorem.

10.6.3.1 PQMC

In the PQMC algorithm we compute

$$\frac{\langle \Psi_T | e^{-\Theta H} O e^{-\Theta H} | \Psi_T \rangle}{\langle \Psi_T | e^{-2\Theta H} | \Psi_T \rangle} = \sum_{\mathbf{s}} P_{\mathbf{s}} \langle O \rangle_{\mathbf{s}} + O(\Delta_\tau^2). \quad (10.100)$$

For each lattice site i , time slice n , we have introduced an independent HS field $\mathbf{s} = \{s_{i,n}\}$ and

$$P_s = \frac{\det(P^\dagger B_s(2\theta, 0)P)}{\sum_s \det(P^\dagger B_s(2\theta, 0)P)},$$

$$\langle O \rangle_s = \frac{\langle \Psi_T | U_s(2\theta, \theta) O U_s(\theta, 0) | \Psi_T \rangle}{\langle \Psi_T | U_s(2\theta, 0) | \Psi_T \rangle}. \quad (10.101)$$

We start by computing the equal-time Green function $O = c_x c_y^\dagger = \delta_{x,y} - c^\dagger A^{(y,x)} c$ with $A_{x_1, x_2}^{(y,x)} = \delta_{x_1, y} \delta_{x_2, x}$. Inserting a source term, we obtain

$$\begin{aligned} \langle c_x c_y^\dagger \rangle_s &= \delta_{x,y} - \frac{\partial}{\partial \eta} \ln \langle \Psi_T | U_s(2\theta, \theta) e^{\eta c^\dagger A^{(y,x)} c} U_s(\theta, 0) | \Psi_T \rangle \Big|_{\eta=0} \\ &= \delta_{x,y} - \frac{\partial}{\partial \eta} \ln \det \left(P^\dagger B_s(2\theta, \theta) e^{\eta A^{(y,x)}} B_s(\theta, 0) P \right) \Big|_{\eta=0} \\ &= \delta_{x,y} - \frac{\partial}{\partial \eta} \text{Tr} \ln \left(P^\dagger B_s(2\theta, \theta) e^{\eta A^{(y,x)}} B_s(\theta, 0) P \right) \Big|_{\eta=0} \\ &= \delta_{x,y} - \text{Tr} \left[(P^\dagger B_s(2\theta, 0)P)^{-1} P^\dagger B_s(2\theta, \theta) A^{(y,x)} B_s(\theta, 0) P \right], \quad (10.102) \end{aligned}$$

$$\left(1 - B_s(\theta, 0)P (P^\dagger B_s(2\theta, 0)P)^{-1} P^\dagger B_s(2\theta, \theta) \right)_{x,y} \equiv (G_s(\theta))_{x,y}. \quad (10.103)$$

We have used (10.244), (10.247) to derive the third equality. The attentive reader will have noticed that (10.244) was shown to be valid only in the case of Hermitian or anti-Hermitian matrices which is certainly not the case of $A^{(y,x)}$. However, since only terms of order η are relevant in the calculation, we may replace $\exp(\eta A)$ by $\exp(\eta(A + A^\dagger)/2) \exp(\eta(A - A^\dagger)/2)$ which is exact up to order η^2 . For the latter form, one may use (10.244). To obtain the fourth equality we have used the relation $\det A = \exp(\text{Tr} \ln A)$.

We now show that any multi-point correlation function decouples into a sum of products of the above defined Green functions. First, we define the cumulants

$$\begin{aligned} \langle\langle O_n \dots O_1 \rangle\rangle_s &= \frac{\partial^n \ln \langle \Psi_T | U_s(2\theta, \theta) e^{\eta_n O_n} \dots e^{\eta_1 O_1} U_s(\theta, 0) | \Psi_T \rangle}{\partial \eta_n \dots \partial \eta_1} \Big|_{\eta_1 \dots \eta_n = 0} \quad (10.104) \end{aligned}$$

with $O_i = c^\dagger A^{(i)} c$. Differentiating the above definition we obtain

$$\begin{aligned} \langle\langle O_1 \rangle\rangle_s &= \langle O_1 \rangle_s \\ \langle\langle O_2 O_1 \rangle\rangle_s &= \langle O_2 O_1 \rangle_s - \langle O_2 \rangle_s \langle O_1 \rangle_s \\ \langle\langle O_3 O_2 O_1 \rangle\rangle_s &= \langle O_3 O_2 O_1 \rangle_s \\ &\quad - \langle O_3 \rangle_s \langle\langle O_2 O_1 \rangle\rangle_s - \langle O_2 \rangle_s \langle\langle O_3 O_1 \rangle\rangle_s \\ &\quad - \langle O_1 \rangle_s \langle\langle O_3 O_2 \rangle\rangle_s - \langle O_1 \rangle_s \langle O_2 \rangle_s \langle O_3 \rangle_s. \quad (10.105) \end{aligned}$$

The following rule, which may be proven by induction, emerges

$$\begin{aligned} \langle\langle O_n \dots O_1 \rangle\rangle_{\mathbf{s}} &= \langle\langle O_n \dots O_1 \rangle\rangle_{\mathbf{s}} + \sum_{j=1}^n \langle\langle O_n \dots \widehat{O}_j \dots O_1 \rangle\rangle_{\mathbf{s}} \langle\langle O_j \rangle\rangle_{\mathbf{s}} \\ &\quad + \sum_{j>i} \langle\langle O_n \dots \widehat{O}_j \dots \widehat{O}_i \dots O_1 \rangle\rangle_{\mathbf{s}} \\ &\quad \langle\langle O_j O_i \rangle\rangle_{\mathbf{s}} + \dots + \langle\langle O_n \rangle\rangle_{\mathbf{s}} \dots \langle\langle O_1 \rangle\rangle_{\mathbf{s}} , \end{aligned} \quad (10.106)$$

where \widehat{O}_j means that the operator O_j has been omitted from the product [62].

The cumulant may now be computed order by order. We concentrate on the form $\langle\langle c_{x_n}^\dagger c_{y_n} \dots c_{x_1}^\dagger c_{y_1} \rangle\rangle$ so that $A_{x,y}^{(i)} = \delta_{x,x_i} \delta_{y,y_i}$. To simplify the notation we introduce the quantities

$$\begin{aligned} B^\flat &= B_{\mathbf{s}}(\Theta, 0)P , \\ B^\langle &= P^\dagger B_{\mathbf{s}}(2\Theta, \Theta) . \end{aligned} \quad (10.107)$$

We have already computed $\langle\langle O_1 \rangle\rangle_{\mathbf{s}}$, see (10.102),

$$\langle\langle O_1 \rangle\rangle_{\mathbf{s}} = \langle\langle c_{x_1}^\dagger c_{y_1} \rangle\rangle = \text{Tr} \left((1 - G_{\mathbf{s}}(\Theta)) A^{(1)} \right) = (1 - G_{\mathbf{s}}(\Theta))_{y_1, x_1} . \quad (10.108)$$

For $n = 2$ we have

$$\begin{aligned} \langle\langle O_2 O_1 \rangle\rangle_{\mathbf{s}} &= \langle\langle c_{x_2}^\dagger c_{y_2} c_{x_1}^\dagger c_{y_1} \rangle\rangle_{\mathbf{s}} \\ &= \frac{\partial^2}{\partial \eta_2 \partial \eta_1} \text{Tr} \ln \left(P^\dagger B_{\mathbf{s}}(2\Theta, \Theta) e^{\eta_2 A^{(2)}} e^{\eta_1 A^{(1)}} B_{\mathbf{s}}(\Theta, 0) P \right) \Big|_{\eta_2, \eta_1=0} \\ &= \frac{\partial}{\partial \eta_2} \text{Tr} \left[\left(B^\langle e^{\eta_2 A^{(2)}} B^\flat \right)^{-1} B^\langle e^{\eta_2 A^{(2)}} A^{(1)} B^\flat \right] \Big|_{\eta_2=0} \\ &= -\text{Tr} \left[\left(B^\langle B^\flat \right)^{-1} B^\langle A^{(2)} B^\flat \right] \left(B^\langle B^\flat \right)^{-1} B^\langle A^{(1)} B^\flat \right] \\ &\quad + \text{Tr} \left[\left(B^\langle B^\flat \right)^{-1} B^\langle A^{(2)} A^{(1)} B^\flat \right] \\ &= \text{Tr} \left(\overline{G_{\mathbf{s}}(\Theta)} A^{(2)} G_{\mathbf{s}}(\Theta) A^{(1)} \right) \\ &= \langle\langle c_{x_2}^\dagger c_{y_1} \rangle\rangle_{\mathbf{s}} \langle\langle c_{y_2} c_{x_1}^\dagger \rangle\rangle_{\mathbf{s}} \end{aligned} \quad (10.109)$$

with $\overline{G} = 1 - G$. To derive the above, we have used the cyclic properties of the trace as well as the relation $G = 1 - B^\flat (B^\langle B^\flat \rangle)^{-1} B^\langle$. Note that for a matrix $A(\eta)$, $(\partial/\partial \eta) A^{-1}(\eta) = -A^{-1}(\eta) [(\partial/\partial \eta) A(\eta)] A^{-1}(\eta)$. There is a simple rule to obtain the third cumulant given the second. In the above expression for the second cumulant, one replaces B^\langle with $B^\langle \exp(\eta_3 A^{(3)})$. This amounts in redefining the Green function as $G(\eta_3) = 1 - B^\flat (B^\langle \exp(\eta_3 A^{(3)}) B^\flat)^{-1} B^\langle \exp(\eta_3 A^{(3)})$. Thus,

$$\begin{aligned}
\langle\langle O_3 O_2 O_1 \rangle\rangle_{\mathbf{s}} &= \langle\langle c_{x_3}^\dagger c_{y_3} c_{x_2}^\dagger c_{y_2} c_{x_1}^\dagger c_{y_1} \rangle\rangle_{\mathbf{s}} \\
&= \frac{\partial}{\partial \eta_3} \text{Tr} \left(\overline{G_{\mathbf{s}}(\Theta, \eta_3)} A^{(2)} G_{\mathbf{s}}(\Theta, \eta_3) A^{(1)} \right) \Big|_{\eta_3=0} \\
&= \text{Tr} \left(\overline{G_{\mathbf{s}}(\Theta)} A^{(3)} G_{\mathbf{s}}(\Theta) A^{(2)} G_{\mathbf{s}}(\Theta) A^{(1)} \right) \\
&\quad - \text{Tr} \left(\overline{G_{\mathbf{s}}(\Theta)} A^{(3)} G_{\mathbf{s}}(\Theta) A^{(1)} \overline{G_{\mathbf{s}}(\Theta)} A^{(2)} \right) \\
&= \langle c_{x_3}^\dagger c_{y_1} \rangle_{\mathbf{s}} \langle c_{y_3} c_{x_2}^\dagger \rangle_{\mathbf{s}} \langle c_{y_2} c_{x_1}^\dagger \rangle_{\mathbf{s}} \\
&\quad - \langle c_{x_3}^\dagger c_{y_2} \rangle_{\mathbf{s}} \langle c_{y_3} c_{x_1}^\dagger \rangle_{\mathbf{s}} \langle c_{x_2}^\dagger c_{y_1} \rangle_{\mathbf{s}} \quad (10.110)
\end{aligned}$$

since

$$\frac{\partial}{\partial \eta_3} G_{\mathbf{s}}(\Theta, \eta_3) \Big|_{\eta_3=0} = -\overline{G_{\mathbf{s}}(\Theta)} A^{(3)} G_{\mathbf{s}}(\Theta) = -\frac{\partial}{\partial \eta_3} \overline{G_{\mathbf{s}}(\Theta, \eta_3)} \Big|_{\eta_3=0}. \quad (10.111)$$

Clearly the same procedure may be applied to obtain the $n+1^{\text{th}}$ cumulant given the n^{th} one. It is also clear that the n^{th} cumulant is a sum of products of Green functions. Thus with (10.106) we have shown that any multi-point correlation function may be reduced into a sum of products of Green functions: **Wicks theorem**. Useful relations include

$$\langle c_{x_2}^\dagger c_{y_2} c_{x_1}^\dagger c_{y_1} \rangle_{\mathbf{s}} = \langle c_{x_2}^\dagger c_{y_1} \rangle_{\mathbf{s}} \langle c_{y_2} c_{x_1}^\dagger \rangle_{\mathbf{s}} + \langle c_{x_2}^\dagger c_{y_2} \rangle_{\mathbf{s}} \langle c_{x_1}^\dagger c_{y_1} \rangle_{\mathbf{s}}. \quad (10.112)$$

10.6.3.2 FTQMC

For the FTQMC we wish to evaluate

$$\frac{\text{Tr} [e^{-\beta H} O]}{\text{Tr} [e^{-\beta H}]} = \sum_{\mathbf{s}} P_{\mathbf{s}} \langle O \rangle_{\mathbf{s}} + O(\Delta_{\tau}^2). \quad (10.113)$$

where

$$\begin{aligned}
P_{\mathbf{s}} &= \frac{\det(1 + B_{\mathbf{s}}(\beta, 0))}{\sum_{\mathbf{s}} \det(1 + B_{\mathbf{s}}(\beta, 0))}, \\
\langle O \rangle_{\mathbf{s}} &= \frac{\text{Tr} [U_{\mathbf{s}}(\beta, \tau) O U_{\mathbf{s}}(\tau, 0)]}{\text{Tr} [U_{\mathbf{s}}(\beta, 0)]}. \quad (10.114)
\end{aligned}$$

Here, we measure the observable on time slice τ . Single-body observables, $O = c^\dagger A c$ are evaluated as

$$\begin{aligned}
\langle O \rangle_{\mathbf{s}} &= \frac{\partial}{\partial \eta} \ln \text{Tr} [U_{\mathbf{s}}(\beta, \tau) e^{\eta O} U_{\mathbf{s}}(\tau, 0)] \Big|_{\eta=0} \\
&= \frac{\partial}{\partial \eta} \ln \det [1 + B_{\mathbf{s}}(\beta, \tau) e^{\eta A} B_{\mathbf{s}}(\tau, 0)] \Big|_{\eta=0} \\
&= \frac{\partial}{\partial \eta} \text{Tr} \ln [1 + B_{\mathbf{s}}(\beta, \tau) e^{\eta A} B_{\mathbf{s}}(\tau, 0)] \Big|_{\eta=0} \\
&= \text{Tr} [B_{\mathbf{s}}(\tau, 0) (1 + B_{\mathbf{s}}(\beta, 0))^{-1} B_{\mathbf{s}}(\beta, \tau) A] \\
&= \text{Tr} \left[\left(1 - (1 + B_{\mathbf{s}}(\tau, 0) B_{\mathbf{s}}(\beta, \tau))^{-1} \right) A \right]. \quad (10.115)
\end{aligned}$$

In particular the Green function is given by

$$\langle c_x c_y^\dagger \rangle_{\mathbf{s}} = (1 + B_{\mathbf{s}}(\tau, 0) B_{\mathbf{s}}(\beta, \tau))_{x,y}^{-1}. \quad (10.116)$$

Defining the cumulants as

$$\langle \langle O_n \dots O_1 \rangle \rangle_{\mathbf{s}} = \frac{\partial^n \ln \text{Tr} [U_{\mathbf{s}}(\beta, \tau) e^{\eta_n O_n} \dots e^{\eta_1 O_1} U_{\mathbf{s}}(\tau, 0)]}{\partial \eta_n \dots \partial \eta_1} \Big|_{\eta_1 \dots \eta_n = 0} \quad (10.117)$$

with $O_i = \mathbf{c}^\dagger A^{(i)} \mathbf{c}$, one can derive Wick's theorem in precisely the same manner as shown for the PQMC. Thus both in the PQMC and FTQMC, it suffices to compute the equal-time Green functions to evaluate any equal-time observable.

10.6.4 Imaginary Time Displaced Green Functions

Imaginary time displaced correlation yield important information. On one hand they may be used to obtain spin and charge gaps [63, 64], as well quasiparticle weights [23]. On the other hand, with the use of the Maximum Entropy method [65, 66] and generalizations thereof [67], dynamical properties such as spin and charge dynamical structure factors, optical conductivity, and single-particle spectral functions may be computed. Those quantities offer the possibility of direct comparison with experiments, such as photoemission, neutron scattering and optical measurements.

Since there is again a Wick's theorem for time displaced correlation functions, it suffices to compute the single-particle Green function for a given HS configuration. We will first start with the FTQMC and then concentrate on the PQMC.

10.6.4.1 FTQMC

For a given HS field, we wish to evaluate

$$G_{\mathbf{s}}(\tau_1, \tau_2)_{x,y} = \langle T c_x(\tau_1) c_y^\dagger(\tau_2) \rangle_{\mathbf{s}} = \begin{cases} \langle c_x(\tau_1) c_y^\dagger(\tau_2) \rangle_{\mathbf{s}} & \text{if } \tau_1 \geq \tau_2 \\ -\langle c_y^\dagger(\tau_2) c_x(\tau_1) \rangle_{\mathbf{s}} & \text{if } \tau_1 < \tau_2 \end{cases}, \quad (10.118)$$

where T corresponds to the time ordering. Thus for $\tau_1 > \tau_2$ $G_{\mathbf{s}}(\tau_1, \tau_2)_{x,y}$ reduces to

$$\begin{aligned} \langle c_x(\tau_1) c_y^\dagger(\tau_2) \rangle_{\mathbf{s}} &= \frac{\text{Tr} [U_{\mathbf{s}}(\beta, \tau_1) c_x U_{\mathbf{s}}(\tau_1, \tau_2) c_y^\dagger U_{\mathbf{s}}(\tau_2, 0)]}{\text{Tr} [U_{\mathbf{s}}(\beta, 0)]} \\ &= \frac{\text{Tr} [U_{\mathbf{s}}(\beta, \tau_2) U_{\mathbf{s}}^{-1}(\tau_1, \tau_2) c_x U_{\mathbf{s}}(\tau_1, \tau_2) c_y^\dagger U_{\mathbf{s}}(\tau_2, 0)]}{\text{Tr} [U_{\mathbf{s}}(\beta, 0)]} . \end{aligned} \quad (10.119)$$

Evaluating $U^{-1}(\tau_1, \tau_2) c_x U_{\mathbf{s}}(\tau_1, \tau_2)$ boils down to the calculation of

$$c_x(\tau) = e^{\tau \mathbf{c}^\dagger A \mathbf{c}} c_x e^{-\tau \mathbf{c}^\dagger A \mathbf{c}} , \quad (10.120)$$

where A is an arbitrary matrix. Differentiating the above with respect to τ yields

$$\frac{\partial c_x(\tau)}{\partial \tau} = e^{\tau \mathbf{c}^\dagger A \mathbf{c}} [\mathbf{c}^\dagger A \mathbf{c}, c_x] e^{-\tau \mathbf{c}^\dagger A \mathbf{c}} = - \sum_z A_{x,z} c_z(\tau) . \quad (10.121)$$

Thus,

$$c_x(\tau) = (e^{-A} \mathbf{c})_x , \quad \text{and similarly } c_x^\dagger(\tau) = (\mathbf{c}^\dagger e^A)_x . \quad (10.122)$$

We can use the above equation successively to obtain

$$\begin{aligned} U_{\mathbf{s}}^{-1}(\tau_1, \tau_2) c_x U_{\mathbf{s}}(\tau_1, \tau_2) &= (B_{\mathbf{s}}(\tau_1, \tau_2) \mathbf{c})_x \\ U_{\mathbf{s}}^{-1}(\tau_1, \tau_2) c_x^\dagger U_{\mathbf{s}}(\tau_1, \tau_2) &= (\mathbf{c}^\dagger B_{\mathbf{s}}^{-1}(\tau_1, \tau_2))_x . \end{aligned} \quad (10.123)$$

Since B is a matrix and not a second quantized operator, we can pull it out of the trace in (10.119) to obtain

$$G_{\mathbf{s}}(\tau_1, \tau_2)_{x,y} = \langle c_x(\tau_1) c_y^\dagger(\tau_2) \rangle_{\mathbf{s}} = [B_{\mathbf{s}}(\tau_1, \tau_2) G_{\mathbf{s}}(\tau_2, \tau_2)]_{x,y} \quad (10.124)$$

with $\tau_1 > \tau_2$, where $G_{\mathbf{s}}(\tau_2)$ is the equal-time Green function computed previously. A similar calculation will yield for $\tau_2 > \tau_1$

$$\begin{aligned} G_{\mathbf{s}}(\tau_1, \tau_2)_{x,y} &= - \langle c_y^\dagger(\tau_2) c_x(\tau_1) \rangle_{\mathbf{s}} \\ &= - [(1 - G_{\mathbf{s}}(\tau_1, \tau_1)) B_{\mathbf{s}}^{-1}(\tau_2, \tau_1)]_{x,y} . \end{aligned} \quad (10.125)$$

The above equations imply the validity of Wick's theorem for time displaced Green functions. Any n -point correlation function at different imaginary times may be mapped onto an expression containing n -point equal-time correlation functions. The n -point equal-time correlation function may then be decomposed into a sum of products of equal-time Green functions. For example, for $\tau_1 > \tau_2$ let us compute

$$\begin{aligned}
 & \langle c_x^\dagger(\tau_1) c_x(\tau_1) c_y^\dagger(\tau_2) c_y(\tau_2) \rangle \\
 &= \frac{\text{Tr}[U(\beta, \tau_2) U^{-1}(\tau_1, \tau_2) c_x^\dagger U^{-1}(\tau_1, \tau_2) U(\tau_1, \tau_2) c_x U(\tau_1, \tau_2) c_y^\dagger c_y U(\tau_2, 0)]}{\text{Tr}[U(\beta, 0)]} \\
 &= \sum_{z, z_1} B^{-1}(\tau_1, \tau_2)_{z, x} B(\tau_1, \tau_2)_{x, z_1} \langle c_z^\dagger(\tau_2) c_{z_1}(\tau_2) c_y^\dagger(\tau_2) c_y(\tau_2) \rangle \\
 &= \sum_{z, z_1} B^{-1}(\tau_1, \tau_2)_{z, x} B(\tau_1, \tau_2)_{x, z_1} \left[(1 - G(\tau_2, \tau_2))_{z_1, z} (1 - G(\tau_2, \tau_2))_{y, y} \right. \\
 &\quad \left. + (1 - G(\tau_2, \tau_2))_{y, z} G(\tau_2, \tau_2)_{z_1, y} \right] \\
 &= [B(\tau_1, \tau_2) (1 - G(\tau_2, \tau_2)) B^{-1}(\tau_1, \tau_2)]_{x, x} [1 - G(\tau_2, \tau_2)]_{y, y} \\
 &\quad + [(1 - G(\tau_2, \tau_2)) B^{-1}(\tau_1, \tau_2)]_{y, x} [B(\tau_1, \tau_2) G(\tau_2, \tau_2)]_{x, y} \\
 &= [1 - G(\tau_1, \tau_1)]_{x, x} [1 - G(\tau_2, \tau_2)]_{y, y} - G(\tau_2, \tau_1)_{y, x} G(\tau_1, \tau_2)_{x, y}. \quad (10.126)
 \end{aligned}$$

In the above, we have omitted the index s , used (10.125) and (10.124), Wick's theorem for equal-time n -point correlation functions as well as the identity

$$B_s(\tau_1, \tau_2) G_s(\tau_2, \tau_2) B_s^{-1}(\tau_1, \tau_2) = G_s(\tau_1, \tau_1). \quad (10.127)$$

We conclude this Subsection, by a method proposed by Hirsch [68] to compute imaginary time displaced Green functions. This equation provides a means to circumvent numerical instabilities which we will discuss in a subsequent chapter and is the basis of the Hirsch-Fye [54] algorithm. Let β be a multiple of τ_1 and $l\tau_1 = \beta$. Using the definition $\tau_i = i\tau_1$ with $i = 1 \dots l$. Let

$$O = \begin{pmatrix} 1 & 0 & \cdot & 0 & B_s(\tau_1, 0) \\ -B_s(\tau_2, \tau_1) & 1 & 0 & \cdot & 0 \\ 0 & -B_s(\tau_3, \tau_2) & 1 & \cdot & 0 \\ \cdot & 0 & -B_s(\tau_4, \tau_3) & \cdot & \cdot \\ \cdot & \cdot & 0 & \cdot & \cdot \\ \cdot & \cdot & \cdot & \cdot & \cdot \\ 0 & \cdot & 0 & -B_s(\tau_l, \tau_{l-1}) & 1 \end{pmatrix}, \quad (10.128)$$

and

$$G = \begin{pmatrix} G_s(\tau_1, \tau_1) & G_s(\tau_1, \tau_2) & \dots & G_s(\tau_1, \tau_l) \\ G_s(\tau_2, \tau_1) & G_s(\tau_2, \tau_2) & \dots & G_s(\tau_2, \tau_l) \\ \cdot & \cdot & \dots & \cdot \\ G_s(\tau_l, \tau_1) & G_s(\tau_l, \tau_2) & \dots & G_s(\tau_l, \tau_l) \end{pmatrix}, \quad (10.129)$$

then

$$O^{-1} = G. \quad (10.130)$$

The above equation is readily verified by showing that $OG = 1$. Here, we illustrate the validity of the above equation for the case $l = 2$. Using (10.125), (10.124) and (10.127), bearing in mind that in this case $\tau_2 = \beta$ and omitting the index s we have

$$G(\tau_1, \tau_1) + B(\tau_1, 0)G(\tau_2, \tau_1) = \underbrace{[1 + B(\tau_1, 0)B(\tau_2, \tau_1)]}_{G^{-1}(\tau_1, \tau_1)} G(\tau_1, \tau_1) = 1, \quad (10.131)$$

$$\begin{aligned} G(\tau_1, \tau_2) + B(\tau_1, 0)G(\tau_2, \tau_2) &= -(1 - G(\tau_1, \tau_1))B^{-1}(\tau_2, \tau_1) \\ &+ B(\tau_1, 0)B(\tau_2, \tau_1)G(\tau_1, \tau_1)B^{-1}(\tau_2, \tau_1) \\ &= \left[-G^{-1}(\tau_1, \tau_1) + \underbrace{1 + B(\tau_1, 0)B(\tau_2, \tau_1)}_{G^{-1}(\tau_1, \tau_1)} \right] G(\tau_1, \tau_1)B^{-1}(\tau_2, \tau_1) = 0, \end{aligned} \quad (10.132)$$

$$-B(\tau_2, \tau_1)G(\tau_1, \tau_1) + G(\tau_2, \tau_1) = -G(\tau_2, \tau_1) + G(\tau_2, \tau_1) = 0, \quad (10.133)$$

and

$$\begin{aligned} -B(\tau_2, \tau_1)G(\tau_1, \tau_2) + G(\tau_2, \tau_2) \\ &= B(\tau_2, \tau_1)(1 - G(\tau_1, \tau_1))B^{-1}(\tau_2, \tau_1) + G(\tau_2, \tau_2) \\ &= 1 - G(\tau_2, \tau_2) + G(\tau_2, \tau_2) = 1, \end{aligned} \quad (10.134)$$

so that

$$\begin{pmatrix} 1 & B(\tau_1, 0) \\ -B(\tau_2, \tau_1) & 1 \end{pmatrix} \begin{pmatrix} G(\tau_1, \tau_1) & G(\tau_1, \tau_2) \\ G(\tau_2, \tau_1) & G(\tau_2, \tau_2) \end{pmatrix} = \begin{pmatrix} 1 & 0 \\ 0 & 1 \end{pmatrix}. \quad (10.135)$$

10.6.4.2 PQMC

Zero-temperature time displaced Green functions are given by

$$\begin{aligned} G_s \left(\Theta + \frac{\tau}{2}, \Theta - \frac{\tau}{2} \right)_{x,y} \\ &= \frac{\langle \Psi_T | U_s(2\Theta, \Theta + \frac{\tau}{2}) c_x U_s(\Theta + \frac{\tau}{2}, \Theta - \frac{\tau}{2}) c_y^\dagger U_s(\Theta - \frac{\tau}{2}, 0) | \Psi_T \rangle}{\langle \Psi_T | U_s(2\Theta, 0) | \Psi_T \rangle} \\ &= \left[B_s \left(\Theta + \frac{\tau}{2}, \Theta - \frac{\tau}{2} \right) G_s \left(\Theta - \frac{\tau}{2} \right) \right]_{x,y} \end{aligned} \quad (10.136)$$

and

$$\begin{aligned} G_s \left(\Theta - \frac{\tau}{2}, \Theta + \frac{\tau}{2} \right)_{x,y} \\ &= - \frac{\langle \Psi_T | U_s(2\Theta, \Theta + \frac{\tau}{2}) c_y^\dagger U_s(\Theta + \frac{\tau}{2}, \Theta - \frac{\tau}{2}) c_x U_s(\Theta - \frac{\tau}{2}, 0) | \Psi_T \rangle}{\langle \Psi_T | U_s(2\Theta, 0) | \Psi_T \rangle} \\ &= - \left[\left(1 - G_s \left(\Theta - \frac{\tau}{2} \right) \right) B_s^{-1} \left(\Theta + \frac{\tau}{2}, \Theta - \frac{\tau}{2} \right) \right]_{x,y}. \end{aligned} \quad (10.137)$$

Here $\tau > 0$ and we have used (10.123), as well as the equal-time Green function of (10.102). Two comments are in order.

- (i) For a given value of τ the effective projection parameter is $\Theta - \tau$. Thus, before starting a simulation, one has to set the maximal value of τ which will be considered, τ_M and the effective projection parameter $\Theta - \tau_M$ should be large enough to yield the ground state within the desired precision.
- (ii) In a canonical ensemble, the chemical potential is meaningless. However, when single-particle Green functions are computed it is required to set the reference energy with regards to which a particle will be added or removed. In other words, it is the chemical potential which delimits photoemission from inverse photoemission.

Thus, it is useful to have an estimate of this quantity if single-particle or pairing correlations are under investigation. For observables such as spin-spin or charge-charge time displaced correlations this complication does not come into play since they are in the particle-hole channel.

10.6.5 The Sign Problem

One of the big advantages of the auxiliary field method, is that one can use symmetries to show explicitly that the sign problem does not occur. The generic way of showing the absence of sign problem is through the factorization of the determinant. In general, particle-hole symmetry allows one to avoid the sign problem (see for example [55] for the case of the Kondo lattice, Hubbard and Periodic Anderson models). In this case, the weight decouples into the product of two determinants in the spin-up and spin-down sectors. Particle-hole symmetry locks in together the sign of both determinants such that the weight remains positive. Models with attractive interactions which couple independently to an internal symmetry with an even number of states lead to weights, for a given HS configuration, which are an even power of a single determinant. If the determinant itself is real (i.e. absence of magnetic fields), the overall weight will be positive. An example is the attractive Hubbard model. The attractive Hubbard model falls into the above class and is hence free of the sign problem.

Here we will give more general conditions under which the sign problem is absent [69]. The proof is very similar to Kramers degeneracy for time reversal symmetric Hamiltonians [70]. Let us assume the existence of an anti-unitary transformation \mathcal{K} with following properties (we adopt the notation of (10.95))

$$\begin{aligned}
 \mathcal{K}^\dagger T \mathcal{K} &= T, \\
 \mathcal{K}^\dagger V(\mathbf{s}) \mathcal{K} &= V(\mathbf{s}), \\
 \mathcal{K}^\dagger \mathcal{K} &= 1, \\
 \mathcal{K}^2 &= -1.
 \end{aligned}
 \tag{10.138}$$

It then follows that the eigenvalues of the matrix $1 + B_{\mathbf{s}}(\beta, 0)$ occur in complex conjugate pairs. Hence,

$$\det(1 + B(\beta, 0)) = \prod_i |\lambda_i|^2
 \tag{10.139}$$

and no sign problem occurs.

Proof. Let us first remind the reader that an anti-linear operator \mathcal{K} satisfies the property $\mathcal{K}(\alpha\mathbf{v} + \beta\mathbf{u}) = \alpha^\dagger\mathcal{K}\mathbf{v} + \beta^\dagger\mathcal{K}\mathbf{u}$, where α and β are complex numbers. An anti-unitary operator, corresponding to time reversal symmetry for example, is an unitary anti-linear transformation so that the scalar product remains invariant $(\mathcal{K}\mathbf{v}, \mathcal{K}\mathbf{u}) = (\mathbf{v}, \mathbf{u})$. Let us assume that \mathbf{v} is an eigenvector of the matrix $1 + B_{\mathbf{s}}(\beta, 0)$ with eigenvalue λ

$$(1 + B_{\mathbf{s}}(\beta, 0))\mathbf{v} = \lambda\mathbf{v} . \quad (10.140)$$

From (10.138) and (10.96) follows that $\mathcal{K}^\dagger(1 + B_{\mathbf{s}}(\beta, 0))\mathcal{K} = 1 + B_{\mathbf{s}}(\beta, 0)$ such that

$$(1 + B_{\mathbf{s}}(\beta, 0))\mathcal{K}\mathbf{v} = \lambda^\dagger\mathcal{K}\mathbf{v} . \quad (10.141)$$

Hence, $\mathcal{K}\mathbf{v}$ is an eigenvector with eigenvalue λ^\dagger . To complete the proof, we have to show that \mathbf{v} and $\mathcal{K}\mathbf{v}$ are linearly independent

$$(\mathbf{v}, \mathcal{K}\mathbf{v}) = (\mathcal{K}^\dagger\mathbf{v}, \mathbf{v}) = (\mathcal{K}\mathcal{K}^\dagger\mathbf{v}, \mathcal{K}\mathbf{v}) = -(\mathbf{v}, \mathcal{K}\mathbf{v}) . \quad (10.142)$$

In the above, we have used the unitarity of \mathcal{K} and the relation $\mathcal{K}^2 = -1$. Hence, since \mathbf{v} and $\mathcal{K}\mathbf{v}$ are orthogonal, we are guaranteed that λ and λ^\dagger will occur in the spectrum. In particular, if λ is real, it occurs an even number of times in the spectrum.

It is interesting to note that models which show spin-nematic phases can be shown to be free of sign problems due the above symmetry even though the factorization of the determinant is not present [71].

Clearly, the sign problem remains the central issue in Monte Carlo simulations of correlated electrons. It has been argued that there is no general solution to this problem [72]. This does not exclude the possibility of finding novel algorithms which can potentially circumvent the sign problem for a larger class of models than at present. A very interesting novel algorithm, the Gaussian Monte Carlo approach, has recently been introduced by Corney and Drummond [18, 73] and is claimed to solve the negative sign problem for a rather general class of models containing the Hubbard model on arbitrary lattices and at arbitrary dopings. As it stands, this method does not produce accurate results and the interested reader is referred to [19] for a detailed discussion of those problems.

10.6.6 Summary

In principle, we now have all the elements required to carry out a QMC simulation. The space we have to sample is that of Nm Ising spins. Here N is the number of lattice sites and m the number of imaginary time slices. For each configuration of Ising spins \mathbf{s} , we can associate a weight. For the PQMC it reads

$$W_{\mathbf{s}} = C^m \det [P^\dagger B_{\mathbf{s}}(2\theta, 0)P] \quad (10.143)$$

and for the FTQMC

$$W_s = C^m \det [1 + B_s(\beta, 0)] . \quad (10.144)$$

Here we will assume that the weight is positive. A Monte Carlo simulation may now be carried out as follows.

- To generate a Markov chain we can adopt a sequential, or random, single spin flip upgrading scheme. We accept the proposed change from s to s' with probability $\min(1, W_{s'}/W_s)$ corresponding to a Metropolis algorithm. Since we can in principle compute the weight W_s at the expense of a set of matrix multiplications and estimation of a determinant we can compute the quotient $W_{s'}/W_s$. This procedure will be repeated until an independent Ising spin configuration is obtained. That is after the autocorrelation time.
- For a given Ising spin configuration, and with the help of the formulas given in the preceding section, we can compute the time displaced Green functions. Since a Wick's theorem holds for a given Hubbard Stratonovich configuration of Ising spins, we have access to all observables.
- After having measured an observable, we will return to step one so as to generate a new, independent configuration of Ising spins.

The implementation of the above program will not work due to the occurrence of numerical instabilities at low temperatures. It also leads to a very inefficient code. In the next two sections will show first to implement efficiently the algorithm. We will first concentrate on simulations for lattice models and then on the Hirsch-Fye approach which is triggered at solving impurity models.

10.7 Numerical Stabilization Schemes for Lattice Models

This section is organized as follows. We will first show how to compute the equal-time Green functions both in the finite (FTQMC) and projective (PQMC) formalisms. The equal-time Green function is the fundamental quantity on which the whole algorithm relies. On one hand and in conjunction with Wick's theorem, it allows to compute any equal-time observable. On the other hand, it determines the Monte Carlo dynamics, since the ratio of statistical weights under a single spin flip is determined by the equal-time Green function (see Sect. 10.7.2). In Sect. 10.7.3 we will show how to compute imaginary time displaced Green functions in an efficient and numerically stable manner.

10.7.1 Numerical Stabilization and Calculation of the Equal-Time Green Function

The fundamental quantity on which the entire algorithm relies is the equal-time Green function. For a given HS configuration of auxiliary fields, this quantity is given by

$$\langle c_x c_y^\dagger \rangle_s = \left(1 - B_s(\theta, 0) P (P^\dagger B_s(2\theta, 0) P)^{-1} P^\dagger B_s(2\theta, \theta) \right)_{x,y} \quad (10.145)$$

for the PQMC, see (10.102), and by

$$\langle c_x c_y^\dagger \rangle_{\mathbf{s}} = (1 + B_{\mathbf{s}}(\tau, 0) B_{\mathbf{s}}(\beta, \tau))_{x,y}^{-1} \quad (10.146)$$

for the FTQMC, see (10.116). On finite precision machines a straightforward calculation of the Green function leads to numerical instabilities at large values of β or projection parameter Θ . To understand the sources of numerical instabilities, it is convenient to consider the PQMC. The rectangular matrix P accounting for the trial wave function is just a set of column orthonormal vectors. Typically for a Hubbard model, at weak couplings, the extremal scales in the matrix $B_{\mathbf{s}}(2\Theta, 0)$ are determined by the kinetic energy and range from $\exp(8t\Theta)$ to $\exp(-8t\Theta)$ in the 2D case. When the set of orthonormal vectors in P are propagated, the large scales will wash out the small scales yielding a numerically ill defined inversion of the matrix $P^\dagger B_{\mathbf{s}}(2\Theta, 0)P$. To be more precise consider a two-electron problem. The matrix P then consists of two column orthonormal vectors $\mathbf{v}(0)_1$ and $\mathbf{v}(0)_2$, which after propagation along the imaginary time axis will be dominated by the largest scales in $B_{\mathbf{s}}(2\Theta, 0)$ so that $\mathbf{v}(2\Theta)_1 = \mathbf{v}(2\Theta)_2 + \epsilon$, where $\mathbf{v}(2\Theta)_1 = B_{\mathbf{s}}(2\Theta, 0)\mathbf{v}_1$. It is the information contained in ϵ which renders the matrix $P^\dagger B_{\mathbf{s}}(2\Theta, 0)P$ non-singular. For large values of Θ this information is lost in round-off errors.

To circumvent this problem a set of matrix decomposition techniques were developed [58, 59, 61]. Those matrix decomposition techniques are best introduced with the Gram-Schmidt orthonormalization method of N_p linearly independent vectors. At imaginary time τ , $B_{\mathbf{s}}(\tau, 0)P \equiv B^\dagger$ is given by the N_p vectors $\mathbf{v}_1 \dots \mathbf{v}_{N_p}$. Orthogonalizing those vectors yields

$$\begin{aligned} \mathbf{v}'_1 &= \mathbf{v}_1 \\ \mathbf{v}'_2 &= \mathbf{v}_2 - \frac{\mathbf{v}_2 \cdot \mathbf{v}'_1}{\mathbf{v}'_1 \cdot \mathbf{v}'_1} \mathbf{v}'_1 \\ &\vdots \\ \mathbf{v}'_{N_p} &= \mathbf{v}_{N_p} - \sum_{i=1}^{N_p-1} \frac{\mathbf{v}_{N_p} \cdot \mathbf{v}'_i}{\mathbf{v}'_i \cdot \mathbf{v}'_i} \mathbf{v}'_i. \end{aligned} \quad (10.147)$$

Since \mathbf{v}'_n depends only on the vectors $\mathbf{v}_n \dots \mathbf{v}_1$ we can write

$$(\mathbf{v}'_1, \dots, \mathbf{v}'_{N_p}) = (\mathbf{v}_1, \dots, \mathbf{v}_{N_p}) V_R^{-1}, \quad (10.148)$$

where V_R is an upper unit triangular $N_p \times N_p$ matrix, that is the diagonal matrix elements are equal to unity. One can furthermore normalize the vectors $\mathbf{v}'_1, \dots, \mathbf{v}'_{N_p}$ to obtain

$$B^\dagger \equiv (\mathbf{v}_1, \dots, \mathbf{v}_{N_p}) = \underbrace{\left(\frac{\mathbf{v}'_1}{|\mathbf{v}'_1|}, \dots, \frac{\mathbf{v}'_{N_p}}{|\mathbf{v}'_{N_p}|} \right)}_{\equiv U} D_R V_R, \quad (10.149)$$

where D is a diagonal matrix containing the scales. One can repeat the procedure to obtain: $B^\langle \equiv P^\dagger B_s(2\Theta, \tau) = V_L D_L U^\langle$. The Green function for the PQMC is now particularly easy to compute:

$$\begin{aligned}
 1 - G_s(\tau) &= B^\rangle (B^\langle B^\rangle)^{-1} B^\langle \\
 &= U^\rangle D_R V_R (V_L D_L U^\langle U^\rangle D_R V_R)^{-1} V_L D_L U^\langle \\
 &= U^\rangle D_R V_R (D_R V_R)^{-1} (U^\langle U^\rangle)^{-1} (V_L D_L)^{-1} V_L D_L U^\langle \\
 &= U^\rangle (U^\langle U^\rangle)^{-1} U^\langle .
 \end{aligned} \tag{10.150}$$

Thus, in the PQMC, all scales which are at the origin of the numerical instabilities disappear from the problem when computing Green functions. Since the entire algorithm relies solely on the knowledge of the Green function, the above stabilization procedure leaves the physical results invariant. Note that although appealing, the Gram-Schmidt orthonormalization is itself unstable, and hence it is more appropriate to use singular value decompositions based on Housholder's method to obtain the above UDV -form for the B matrices [74]. In practice the frequency at which the stabilization is carried out is problem dependent. Typically, for the Hubbard model with $\Delta_\tau t = 0.125$ stabilization at every 10^{th} time slice produces excellent accuracy.

The stabilization procedure for the finite-temperature algorithm is more subtle since scales do not drop out in the calculation of the Green function. Below, we provide two ways of computing the Green function.

The first approach relies on the identity

$$\begin{pmatrix} A & B \\ C & D \end{pmatrix}^{-1} = \begin{pmatrix} (A - BD^{-1}C)^{-1} & (C - DB^{-1}A)^{-1} \\ (B - AC^{-1}D)^{-1} & (D - CA^{-1}B)^{-1} \end{pmatrix}, \tag{10.151}$$

where A, B, C and D are matrices. Using the above, we obtain

$$\begin{pmatrix} 1 & B_s(\beta, \tau) \\ -B_s(\tau, 0) & 1 \end{pmatrix}^{-1} = \begin{pmatrix} G_s(0) & -(1 - G_s(0))B_s^{-1}(\tau, 0) \\ B_s(\tau, 0)G_s(0) & G_s(\tau) \end{pmatrix}. \tag{10.152}$$

The diagonal terms on the right hand side of the above equation correspond to the desired equal-time Green functions. The off-diagonal terms are nothing but the time displaced Green functions, see (10.124) and (10.125). To evaluate the left hand side of the above equation, we first have to bring $B_s(\tau, 0)$ and $B_s(\beta, \tau)$ in UDV -forms. This has to be done step by step so as to avoid mixing large and small scales. Consider the propagation $B_s(\tau, 0)$, and a time interval τ_1 , with $n\tau_1 = \tau$, for which the different scales in $B_s(n\tau_1, (n-1)\tau_1)$ do not exceed machine precision. Since $B_s(\tau, 0) = B_s(n\tau_1, (n-1)\tau_1) \dots B_s(\tau_1, 0)$ we can evaluate $B_s(\tau, 0)$ for $n = 2$ with

$$B_s(2\tau_1, \tau_1) \underbrace{B_s(\tau_1, 0)}_{U_1 D_1 V_1} = \underbrace{(B_s(2\tau_1, \tau_1) U_1) D_1}_{U_2 D_2 V} V_1 = U_2 D_2 V_2, \tag{10.153}$$

where $V_2 = VV_1$. The parenthesis determine the order in which the matrix multiplication are to be done. In all operations, mixing of scales is avoided. After the multiplication with diagonal matrix D_1 scales are again separated with the use of the singular value decomposition.

Thus, for $B_s(\tau, 0) = U_R D_R V_R$ and $B_s(\beta, \tau) = V_L D_L U_L$ we have to invert

$$\begin{aligned} & \begin{pmatrix} I & V_L D_L U_L \\ -U_R D_R V_R & I \end{pmatrix}^{-1} \\ &= \left[\begin{pmatrix} V_L & 0 \\ 0 & U_R \end{pmatrix} \underbrace{\begin{pmatrix} (V_R V_L)^{-1} & D_L \\ -D_R & (U_L U_R)^{-1} \end{pmatrix}}_{UDV} \begin{pmatrix} V_R & 0 \\ 0 & U_L \end{pmatrix} \right]^{-1} \\ &= \left[\begin{pmatrix} V_R^{-1} & 0 \\ 0 & U_L^{-1} \end{pmatrix} V^{-1} \right] D^{-1} \left[U^{-1} \begin{pmatrix} V_L^{-1} & 0 \\ 0 & U_R^{-1} \end{pmatrix} \right]. \quad (10.154) \end{aligned}$$

In the above, all matrix multiplications are well defined. In particular, the matrix D contains only large scales since the matrices $(V_R V_L)^{-1}$ and $(U_L U_R)^{-1}$ act as a cutoff to the exponentially small scales in D_L and D_R . This method to compute Green functions is very stable and has the advantage of producing time displaced Green functions. However, it is numerically expensive since the matrices involved are twice as big as the B matrices.

Alternative methods to compute $G_s(\tau)$ which involve matrix manipulations only of the size of B include

$$\begin{aligned} & (1 + B_s(\tau, 0) B_s(\beta, \tau))^{-1} \\ &= (1 + U_R D_R V_R V_L D_L U_L)^{-1} \\ &= U_L^{-1} \underbrace{((U_L U_R)^{-1} + D_R (V_R V_L) D_L)}_{UDV}^{-1} U_R^{-1} \\ &= (V U_L)^{-1} D^{-1} (U_R U^{-1}). \quad (10.155) \end{aligned}$$

Again, $(U_L U_R)^{-1}$ acts as a cutoff to the small scales in $D_R (V_R V_L) D_L$ so that D contains only large scales.

The accuracy of both presented methods may be tested by in the following way. Given the Green function at time τ we can upgrade and wrap, see (10.127), this Green function to time slice $\tau + \tau_1$. Of course, for the time interval τ_1 the involved scales should lie within the accuracy of the computer $\sim 10^{-12}$ for double precision numbers. The Green function at time $\tau + \tau_1$ obtained thereby may be compared to the one computed from scratch using (10.154) or (10.155). For a 4×4 half-filled Hubbard model at $U/t = 4$, $\beta t = 20$, $\Delta_\tau t = 0.1$ and $\tau_1 = 10 \Delta_\tau$ we obtain an average (maximal) difference between the matrix elements of both Green functions of 10^{-10} (10^{-6}) which is orders of magnitude smaller than the statistical uncertainty. Had we chosen $\tau_1 = 50 \Delta_\tau$ the accuracy drops to 0.01 and 100.0 for the average and maximal differences.

10.7.2 The Monte Carlo Sampling

The Monte Carlo sampling used in the auxiliary field approach is based on a single spin-flip algorithm. Acceptance or rejection of this spin flip requires the knowledge of the ratio

$$R = \frac{P_{s'}}{P_s}, \quad (10.156)$$

where s and s' differ only at one point in space i , and imaginary time n . For the Ising field required to decouple the Hubbard interaction, (10.235) and (10.238)

$$s'_{i',n'} = \begin{cases} s_{i',n'} & \text{if } i' \neq i \text{ and } n' \neq n \\ -s_{i,n} & \text{if } i' = i \text{ and } n' = n \end{cases}. \quad (10.157)$$

The calculation of R boils down to computing the ratio of two determinants

$$R = \begin{cases} \frac{\det [1 + B_{s'}(\beta, 0)]}{\det [1 + B_s(\beta, 0)]} & \text{for the FTQMC} \\ \frac{\det [P^\dagger B_{s'}(2\Theta, 0)P]}{\det [P^\dagger B_s(2\Theta, 0)P]} & \text{for the PQMC} \end{cases}. \quad (10.158)$$

For the Hubbard interaction with HS transformation of (10.235) only the matrix $V(s_n)$ will be effected by the move. Hence, with

$$e^{V(s'_n)} = \left[1 + \underbrace{\left(e^{V(s'_n)} e^{-V(s_n)} - 1 \right)}_{\Delta} \right] e^{V(s_n)} \quad (10.159)$$

we have

$$B_{s'}(\bullet, 0) = B_s(\bullet, \tau) (1 + \Delta) B_s(\tau, 0), \quad (10.160)$$

where the \bullet stands for 2Θ or β and $\tau = n\Delta$.

For the FTQMC, the ratio is given by

$$\begin{aligned} & \frac{\det [1 + B_s(\beta, \tau)(1 + \Delta)B_s(\tau, 0)]}{\det [1 + B_s(\beta, 0)]} \\ &= \det \left[1 + \Delta B_s(\tau, 0) (1 + B_s(\beta, 0))^{-1} B_s(\beta, \tau) \right] \\ &= \det \left[1 + \Delta \left(1 - (1 + B_s(\tau, 0)B_s(\beta, \tau))^{-1} \right) \right] \\ &= \det [1 + \Delta (1 - G_s(\tau))] . \end{aligned} \quad (10.161)$$

Where the last line follows from the fact that the equal-time Green function reads $G_s(\tau) = (1 + B_s(\tau, 0)B_s(\beta, \tau))^{-1}$. Hence the ratio is uniquely determined from the knowledge of the equal-time Green function.

Let us now compute the ratio for the PQMC. Introducing the notation $B_s^{\langle} = P^\dagger B_s(2\Theta, \tau)$ and $B_s^{\rangle} = B_s(\tau, 0)P$, again we have to evaluate

$$\begin{aligned}
\frac{\det \left[B_s^{\langle} (1 + \Delta^{(i)}) B_s^{\rangle} \right]}{\det \left[B_s^{\langle} B_s^{\rangle} \right]} &= \det \left[B_s^{\langle} (1 + \Delta^{(i)}) B_s^{\rangle} (B_s^{\langle} B_s^{\rangle})^{-1} \right] \\
&= \det \left[1 + B_s^{\langle} \Delta^{(i)} B_s^{\rangle} (B_s^{\langle} B_s^{\rangle})^{-1} \right] \\
&= \det \left[1 + \Delta^{(i)} B_s^{\rangle} (B_s^{\langle} B_s^{\rangle})^{-1} B_s^{\langle} \right], \quad (10.162)
\end{aligned}$$

where the last equation follows from the identity $\det [1 + AB] = \det [1 + BA]$ for arbitrary rectangular matrices³. We can recognize the Green function of the PQMC $B_s^{\rangle} (B_s^{\langle} B_s^{\rangle})^{-1} B_s^{\langle} = 1 - G_s(\tau)$. The result is thus identical to that of the FTQMC provided that we replace the finite-temperature equal-time Green function with the zero-temperature one. Hence, in both algorithms, the ratio is essentially given by the equal-time Green function which, at this point, we know how to compute in a numerically stable manner.

Having calculated the ratio R for a single spin flip one may now decide stochastically within, for example, a Metropolis scheme if the move is accepted or not. In case of acceptance, we have to update the Green function since this quantity is required at the next step.

Since in general the matrix Δ has only a few non-zero entries, it is convenient to use the Sherman-Morrison formula [74] which states that

$$\begin{aligned}
(A + \mathbf{u} \otimes \mathbf{v})^{-1} &= (1 + A^{-1} \mathbf{u} \otimes \mathbf{v})^{-1} A^{-1} \\
&= [1 - A^{-1} \mathbf{u} \otimes \mathbf{v} + A^{-1} \mathbf{u} \otimes \underbrace{\mathbf{v} A^{-1} \mathbf{u}}_{\equiv \lambda} \otimes \mathbf{v} + A^{-1} \mathbf{u} \otimes \lambda^2 \mathbf{v} - \dots] A^{-1} \\
&= [1 - A^{-1} \mathbf{u} \otimes \mathbf{v} (1 - \lambda + \lambda^2 - \dots)] A^{-1} \\
&= A^{-1} - \frac{(A^{-1} \mathbf{u}) \otimes (\mathbf{v} A^{-1})}{1 + \mathbf{v} \bullet A^{-1} \mathbf{u}}, \quad (10.163)
\end{aligned}$$

where A is an $N \times N$ matrix, \mathbf{u}, \mathbf{v} N -dimensional vectors with tensor product defined as $(\mathbf{u} \otimes \mathbf{v})_{x,y} = \mathbf{u}_x \mathbf{v}_y$.

To show how to use this formula for the updating of the Green function, let us first assume that matrix Δ has only one non-vanishing entry $\Delta_{x,y} = \delta_{x,z} \delta_{y,z'} \eta^{(z,z')}$. In the case of the FTQMC we will then have to compute

$$\begin{aligned}
G_{s'}(\tau) &= [1 + (1 + \Delta) B_s(\tau, 0) B_s(\beta, \tau)]^{-1} \\
&= B_s^{-1}(\beta, \tau) [1 + B_s(\beta, \tau) (1 + \Delta) B_s(\tau, 0)]^{-1} B_s(\beta, \tau) \\
&= B_s^{-1}(\beta, \tau) [1 + B_s(\beta, \tau) B_s(\tau, 0) + \mathbf{u} \otimes \mathbf{v}]^{-1} B_s(\beta, \tau) \quad (10.164)
\end{aligned}$$

where $\mathbf{u}_x = [B_s(\beta, \tau)]_{x,z} \eta^{(z,z')}$ and $\mathbf{v}_x = [B_s(\tau, 0)]_{z',x}$.

³ This identity may be formally proven by using the relation $\det(1 + AB) = \exp(\text{Tr} \log(1 + AB))$, expanding the logarithm and using the cyclic properties of the trace.

Using the Sherman-Morrison formula for inverting $1 + B_s(\beta, \tau)B_s(\tau, 0) + \mathbf{u} \otimes \mathbf{v}$ yields

$$[G_{s'}(\tau)]_{x,y} = [G_s(\tau)]_{x,y} - \frac{[G_s(\tau)]_{x,z} \eta^{(z,z')} [1 - G_s(\tau)]_{z',y}}{1 + \eta^{(z,z')} [1 - G_s(\tau)]_{z',z}}. \quad (10.165)$$

Precisely the same equation holds for the PQMC provided that one replaces the finite-temperature Green function by the zero-temperature one. To show this, one will first compute

$$\begin{aligned} (B_s^{\langle} B_s^{\rangle})^{-1} &= (B_s^{\langle} (1 + \Delta) B_s^{\rangle})^{-1} = (B_s^{\langle} B_s^{\rangle} + \mathbf{u} \otimes \mathbf{v})^{-1} \\ &= (B_s^{\langle} B_s^{\rangle})^{-1} - \frac{(B_s^{\langle} B_s^{\rangle})^{-1} \mathbf{u} \otimes \mathbf{v} (B_s^{\langle} B_s^{\rangle})^{-1}}{1 + \eta^{(z,z')} [1 - G_s^0(\tau)]_{z',z}} \end{aligned} \quad (10.166)$$

with $\mathbf{u}_x = [B_s^{\langle}]_{x,z} \eta^{(z,z')}$ and $\mathbf{v}_x = [B_s^{\rangle}]_{z',x}$. Here x runs from $1 \dots N_p$ where N_p corresponds to the number of particles contained in the trial wave function and the zero-temperature Green function reads $G_s^0(\tau) = 1 - B_s^{\langle} (B_s^{\langle} B_s^{\rangle})^{-1} B_s^{\rangle}$. After some straightforward algebra, one obtains

$$\begin{aligned} [G_{s'}^0(\tau)]_{x,y} &= [1 - (1 + \Delta) B_s^{\langle} (B_s^{\langle} (1 + \Delta) B_s^{\rangle})^{-1} B_s^{\rangle}]_{x,y} \\ &= [G_s^0(\tau)]_{x,y} - \frac{[G_s^0(\tau)]_{x,z} \eta^{(z,z')} [1 - G_s^0(\tau)]_{z',y}}{1 + \eta^{(z,z')} [1 - G_s^0(\tau)]_{z',z}} \end{aligned} \quad (10.167)$$

In the above, we have assumed that the matrix Δ has only a single non-zero entry. In general, it is convenient to work in a basis where Δ is diagonal with n non-vanishing eigenvalues. One will then iterate the above procedure n -times to upgrade the Green function.

10.7.3 Numerical Calculation of Imaginary Time Displaced Green Functions

In Sect. 10.6.4 we introduced the time displaced Green functions both within the ground-state and finite-temperature formulations. Our aim here is to show how to compute them in a numerically stable manner. We will first start with the FTQMC and then concentrate on the PQMC.

10.7.3.1 FTQMC

For a given HS field, we wish to evaluate

$$G_s(\tau_1, \tau_2)_{x,y} = \langle c_x(\tau_1) c_y^\dagger(\tau_2) \rangle_s = B_s(\tau_1, \tau_2) G_s(\tau_2) \quad \tau_1 > \tau_2, \quad (10.168)$$

where $G_s(\tau_1)$ is the equal-time Green function computed previously and

$$\begin{aligned}
G_{\mathbf{s}}(\tau_1, \tau_2)_{x,y} &= -\langle c_y^\dagger(\tau_2) c_x(\tau_1) \rangle_{\mathbf{s}} \\
&= -(1 - G_{\mathbf{s}}(\tau_1)) B_{\mathbf{s}}^{-1}(\tau_2, \tau_1) \quad \tau_2 > \tau_1, \quad (10.169)
\end{aligned}$$

see (10.125) and (10.124).

Returning to (10.152) we see that we have already computed the time displaced Green functions $G_{\mathbf{s}}(0, \tau)$ and $G_{\mathbf{s}}(\tau, 0)$ when discussing a stabilization scheme for the equal-time Green functions. However, this calculation is expensive and is done only at times $\tau = n\tau_1$ where τ_1 is time scale on which all energy scales fit well on finite precision machines. To obtain the Green functions for arbitrary values of τ one uses the relations

$$\begin{aligned}
G_{\mathbf{s}}(0, \tau + \tau_2) &= G_{\mathbf{s}}(0, \tau) B_{\mathbf{s}}^{-1}(\tau_2, \tau), \\
G_{\mathbf{s}}(\tau + \tau_2, 0) &= B_{\mathbf{s}}(\tau_2, \tau) G_{\mathbf{s}}(\tau, 0), \quad (10.170)
\end{aligned}$$

where $\tau_2 < \tau_1$.

With the above method, we have access to all time displaced Green functions $G_{\mathbf{s}}(0, \tau)$ and $G_{\mathbf{s}}(\tau, 0)$. However, we do not use translation invariance in imaginary time. Clearly, using this symmetry in the calculation of time displaced quantities will reduce the fluctuations which may sometimes be desirable. A numerically expensive but elegant way of producing all time displaced Green functions relies on the inversion of the matrix O given in (10.128). Here, provided the τ_1 is small enough so that the scales involved in $B_{\mathbf{s}}(\tau + \tau_1, \tau)$ fit on finite precision machines, the matrix inversion of O^{-1} is numerically stable and yields the Green functions between arbitrary time slices $n\tau_1$ and $m\tau_1$. For $\beta/\tau_1 = l$, the matrix to inverse has the dimension l times the size of the B matrices, and is hence expensive to compute. It is worth noting that on vector machines the performance grows with growing vector size so that the above method can become attractive. Having computed the Green functions $G_{\mathbf{s}}(n\tau_1, m\tau_1)$ we can obtain Green functions on any two time slices by using equations of the type (10.170).

10.7.3.2 PQMC

Zero-temperature time displaced Green functions are given by

$$\begin{aligned}
G_{\mathbf{s}}\left(\theta + \frac{\tau}{2}, \theta - \frac{\tau}{2}\right)_{x,y} &= \left[B_{\mathbf{s}}\left(\theta + \frac{\tau}{2}, \theta - \frac{\tau}{2}\right) G_{\mathbf{s}}\left(\theta - \frac{\tau}{2}\right) \right]_{x,y} \\
G_{\mathbf{s}}\left(\theta - \frac{\tau}{2}, \theta + \frac{\tau}{2}\right)_{x,y} &= - \left[\left(1 - G_{\mathbf{s}}\left(\theta - \frac{\tau}{2}\right)\right) B_{\mathbf{s}}^{-1}\left(\theta + \frac{\tau}{2}, \theta - \frac{\tau}{2}\right) \right]_{x,y} \quad (10.171)
\end{aligned}$$

with $\tau > 0$, see (10.137).

Before showing how to compute imaginary time displaced Green functions, we first note that a direct multiplication of the equal-time Green function with B matrices is unstable for larger values of τ . This can be understood in the framework of free electrons on a 2D square lattice

$$H = -t \sum_{\langle i,j \rangle} c_i^\dagger c_j, \quad (10.172)$$

where the sum runs over nearest neighbors. For this Hamiltonian one has

$$\langle \Psi_0 | c_{\mathbf{k}}^\dagger(\tau) c_{\mathbf{k}} | \Psi_0 \rangle = e^{\tau(\epsilon_{\mathbf{k}} - \mu)} \langle \Psi_0 | c_{\mathbf{k}}^\dagger c_{\mathbf{k}} | \Psi_0 \rangle, \quad (10.173)$$

where $\epsilon_{\mathbf{k}} = -2t(\cos(\mathbf{k}a_x) + \cos(\mathbf{k}a_y))$, a_x, a_y being the lattice constants. We will assume $|\Psi_0\rangle$ to be non-degenerate. In a numerical calculation the eigenvalues and eigenvectors of the above Hamiltonian will be known up to machine precision ϵ . In the case $\epsilon_{\mathbf{k}} - \mu > 0$ is $\langle \Psi_0 | c_{\mathbf{k}}^\dagger c_{\mathbf{k}} | \Psi_0 \rangle \equiv 0$. However, on a finite precision machine the later quantity will take a value of the order of ϵ . When calculating $\langle \Psi_0 | c_{\mathbf{k}}^\dagger(\tau) c_{\mathbf{k}} | \Psi_0 \rangle$ this roundoff error will be blown up exponentially and the result for large values of τ will be unreliable. In (10.137) the B matrices play the role of the exponential factor $\exp(\tau(\epsilon_{\mathbf{k}} - \mu))$ and the equal-time Green functions correspond to $\langle \Psi_0 | c_{\mathbf{k}}^\dagger c_{\mathbf{k}} | \Psi_0 \rangle$. In the PQMC, the stability problem is much more severe than for free electrons since the presence of the time dependent HS field mixes different scales.

An elegant and efficient method [75] to alleviate this problem rests on the observation that in the PQMC the Green function is a projector. Consider again the free electron case. For a non-degenerate ground state $\langle \Psi_0 | c_{\mathbf{k}}^\dagger c_{\mathbf{k}} | \Psi_0 \rangle = 0, 1$ so that

$$\langle \Psi_0 | c_{\mathbf{k}}^\dagger(\tau) c_{\mathbf{k}} | \Psi_0 \rangle = \left(\langle \Psi_0 | c_{\mathbf{k}}^\dagger c_{\mathbf{k}} | \Psi_0 \rangle e^{\epsilon_{\mathbf{k}} - \mu} \right)^\tau. \quad (10.174)$$

The above involves only well defined numerical manipulations even in the large τ limit provided that all scales fit onto finite precision machines for a unit time interval.

The implementation of this idea in the QMC algorithm is as follows. First, one has to notice that the Green function $G_{\mathbf{s}}(\tau)$ is a projector

$$G_{\mathbf{s}}(\tau)^2 = G_{\mathbf{s}}(\tau). \quad (10.175)$$

We have already seen that for $P^\dagger B_{\mathbf{s}}(2\theta, \tau) = V_L D_L U^\dagger$ and $B_{\mathbf{s}}(\tau, 0) = U^\dagger D_R U_R$, $G_{\mathbf{s}}(\tau) = 1 - U^\dagger (U^\dagger U) \tau^{-1} U^\dagger$. Since $[U^\dagger (U^\dagger U) \tau^{-1} U^\dagger]^2 = U^\dagger (U^\dagger U) \tau^{-1} U^\dagger$ we have

$$\begin{aligned} G_{\mathbf{s}}^2(\tau) &= G_{\mathbf{s}}(\tau), \\ (1 - G_{\mathbf{s}}(\tau))^2 &= 1 - G_{\mathbf{s}}(\tau). \end{aligned} \quad (10.176)$$

This property implies that $G_{\mathbf{s}}(\tau_1, \tau_3)$ obeys a simple composition identity

$$G_{\mathbf{s}}(\tau_1, \tau_3) = G_{\mathbf{s}}(\tau_1, \tau_2) G_{\mathbf{s}}(\tau_2, \tau_1). \quad (10.177)$$

In particular for $\tau_1 > \tau_2 > \tau_3$

$$\begin{aligned} G_{\mathbf{s}}(\tau_1, \tau_3) &= B_{\mathbf{s}}(\tau_1, \tau_3) G_{\mathbf{s}}^2(\tau_3) = G_{\mathbf{s}}(\tau_1, \tau_3) G_{\mathbf{s}}(\tau_3) \\ &= \underbrace{G_{\mathbf{s}}(\tau_1, \tau_3) B_{\mathbf{s}}^{-1}(\tau_2, \tau_3)}_{G_{\mathbf{s}}(\tau_1, \tau_2)} \underbrace{B_{\mathbf{s}}(\tau_2, \tau_3) G_{\mathbf{s}}(\tau_3)}_{G_{\mathbf{s}}(\tau_2, \tau_3)}. \end{aligned} \quad (10.178)$$

A similar proof is valid for $\tau_3 > \tau_2 > \tau_1$.

Using this composition property (10.177) we can break up a large τ interval into a set of smaller intervals of length $\tau = N\tau_1$ so that

$$G_s \left(\Theta + \frac{\tau}{2}, \Theta - \frac{\tau}{2} \right) = \prod_{n=0}^{N-1} G_s \left(\Theta - \frac{\tau}{2} + [n+1]\tau_1, \Theta - \frac{\tau}{2} + n\tau_1 \right). \quad (10.179)$$

The above equation is the generalization of (10.174). If τ_1 is small enough each Green function in the above product is accurate and has matrix elements bounded by order unity. The matrix multiplication is then numerically well defined.

We conclude this section by comparing with a different approach to computed imaginary time correlation functions in the framework of the QMC [63]. We consider the special case of the Kondo lattice model (see Fig. 10.16). As apparent the results are identical within error-bars. The important point however, is that the method based on (10.179) is for the considered case an order of magnitude quicker in CPU time than the method of [63].

10.7.4 Practical Implementation

In this section we first describe in detail a possible efficient implementation of the finite-temperature algorithm and then comment on the differences required for the

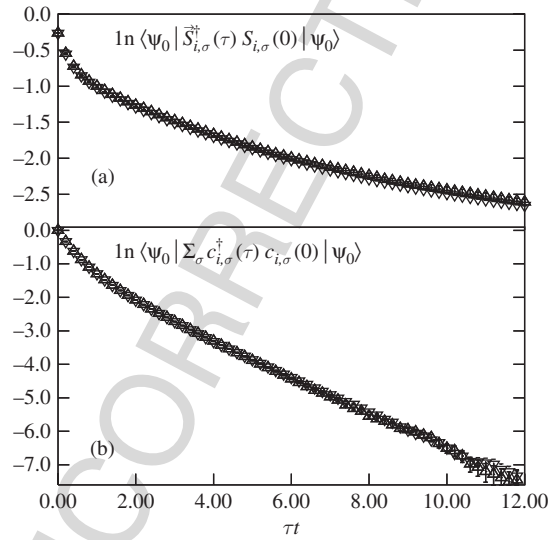


Fig. 10.16. Imaginary time displaced on-site spin-spin correlation function (a) and Green function (b). We consider a 6×6 lattice at half-filling and $J/t = 1.2$. In both (a) and (b) results obtained from (10.179) (\triangle) and from an alternative approach presented in [63] (∇) are plotted

implementation of the projector formalism. It is convenient to split the total imaginary time propagation β , into intervals of length τ_1 such that $n\tau_1 = \beta$. We require τ_1 to be small enough such that all scales in the matrices $B_s(\tau_1, 0)$ fit into say 64 bit reals. The organization of the time slices is shown schematically in Fig. 10.17. To save computer time, we will need enough memory to store $n + 1$ orthogonal matrices U , $n + 1$ triangular matrices V and $n + 1$ diagonal matrices D .

At the onset, we start from a randomly chosen Hubbard-Stratonovich configuration of fields s . We then compute $B_s(\tau_1, 0)$ carry out a singular value decomposition and store the result in U_1, D_1 and V_1 . Given the UDV -decomposition of $B_s(n\tau_1, 0)$, where $(1 \leq n_\tau < n)$, we compute the UDV -decomposition of $B_s[(n_\tau + 1)\tau_1, 0]$ using (10.153) and store the results in $U_{n_\tau+1}, D_{n_\tau+1}$ and $D_{n_\tau+1}$. Hence, our storage now contains

$$U_{n_\tau} D_{n_\tau} V_{n_\tau} = B_s(n_\tau \tau_1, 0) \tag{10.180}$$

with $1 \leq n_\tau \leq n$.

At this stage we can sequentially upgrade the Hubbard Stratonovich fields from $\tau = \beta$ to $\tau = \Delta_\tau$. In doing so, we will take care of storing information to subsequently carry out a sweep from $\tau = \Delta_\tau$ to $\tau = \beta$.

10.7.4.1 From $\tau = \beta$ to $\tau = \Delta_\tau$

From the UDV -decomposition of $B_s(\beta = n\tau_1, 0)$ which we read out of the storage (U_n, D_n, V_n) , we compute in a numerically stable way the equal-time Green function on time slice $\tau = \beta$. Having freed the arrays U_n, D_n and V_n we set them to unity such that $B_s(\beta, n\tau_1 = \beta) \equiv 1 = V_n D_n U_n$. We can now sweep down from time slice $\tau = \beta$ to time slice $\tau = \Delta_\tau$.

Given the Green function at time $\tau = n_\tau \tau_1$ we sequentially upgrade all the Hubbard Stratonovich fields on this time slice. Each time a move is accepted, we will have to update the equal-time Green function. To move to the next time slice $\tau - \Delta_\tau$, we make use of the equation

$$G_s(\tau - \Delta_\tau) = B_s^{-1}(\tau, \tau - \Delta_\tau) G_s(\tau) B_s(\tau, \tau - \Delta_\tau) . \tag{10.181}$$

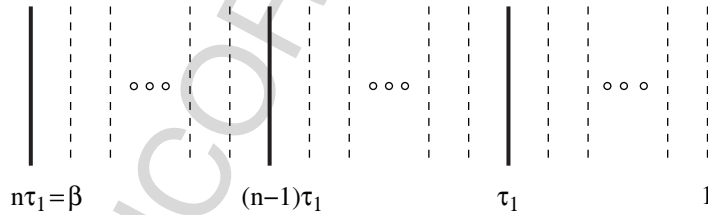


Fig. 10.17. Each line (solid or dashed) denotes a time slice separated by an imaginary time propagation Δ_τ . The solid lines correspond to time slices where we store the UDV -decomposition of the matrices $B_s(\beta, n\tau_1)$ or $B_s(n\tau_1, 0)$ depending upon the direction of the propagation ($1 \leq n_\tau \leq n$)

We will repeat the above procedure till we arrive at time slice $\tau = (n_\tau - 1)\tau_1$. At this stage, we have to recompute the equal-time Green function due to the accumulation of round-off errors and hence loss of precision. To do so, we read from the storage $U_R = U_{n_\tau-1}$, $D_R = U_{n_\tau-1}$ and $V_R = U_{n_\tau-1}$ such that $B_s((n_\tau - 1)\tau_1, 0) = U_R D_R V_R$. Note that we have not yet upgraded the Hubbard Stratonovich fields involved in $B_s((n_\tau - 1)\tau_1, 0)$ so that this storage slot is still up to date. We then compute the matrix $B_s(n_\tau\tau_1, (n_\tau - 1)\tau_1)$ and read from the storage $\tilde{V}_L = V_{n_\tau}$, $\tilde{D}_L = V_{n_\tau}$ and $\tilde{U}_L = V_{n_\tau}$ such that $B_s(\beta, n_\tau\tau_1) = \tilde{V}_L \tilde{D}_L \tilde{U}_L$. With this information and the computed matrix $B_s(n_\tau\tau_1, (n_\tau - 1)\tau_1)$ we will calculate $B_s(\beta, (n_\tau - 1)\tau_1) = V_L D_L U_L$, see (10.153). We now store this result as $V_{n_\tau-1} = V_L$, $D_{n_\tau-1} = D_L$ and $U_{n_\tau-1} = U_L$, and recompute the Green function. Note that as a cross check, one can compare both Green functions to test the numerical accuracy. Hence, we now have a fresh estimate of the Green function at time slice $\tau = (n_\tau - 1)\tau_1$ and we can iterate the procedure till we arrive at time slice Δ_τ .

Hence, in this manner, we sweep down from time slice β to time slice Δ_τ , upgrade sequentially all the Hubbard Stratonovich fields and have stored

$$B_s(\beta, n_\tau\tau_1) = V_{n_\tau} D_{n_\tau} U_{n_\tau} \quad (10.182)$$

with $0 \leq n_\tau \leq n$. We can now carry out a sweep from Δ_τ to β and take care of storing the information required for the sweep from β to Δ_τ .

10.7.4.2 From $\tau = \Delta_\tau$ to β

We initially set $n_\tau = 0$, read out from the storage $B_s(\beta, 0) = V_0 D_0 U_0$ and compute the Green function on time slice $\tau = 0$. This storage slot is then set to unity such that $B_s(0, 0) = U_0 D_0 V_0 \equiv 1$.

Assuming that we are on time slice $\tau = n_\tau\tau_1$, we propagate the Green function to time slice $\tau + \Delta_\tau$ with

$$G_s(\tau + \Delta_\tau) = B_s(\tau + \Delta_\tau, \tau) G_s(\tau) B_s^{-1}(\tau + \Delta_\tau, \tau) \quad (10.183)$$

and upgrade the Hubbard Stratonovich fields on time slice $\tau + \Delta_\tau$. The above procedure is repeated till we reach time slice $(n_\tau + 1)\tau_1$, where we have to recompute the Green function. To do so, we read from the storage $V_L = V_{n_\tau+1}$, $D_L = D_{n_\tau+1}$ and $U_L = U_{n_\tau+1}$ such that $B_s(\beta, (n_\tau + 1)\tau_1) = V_L D_L U_L$. We then compute $B_s((n_\tau + 1)\tau_1, n_\tau\tau_1)$ and from the UDV -form of $B_s(n_\tau\tau_1, 0)$ which we obtain from the storage slot n_τ , we calculate $B_s((n_\tau + 1)\tau_1, 0) = U_R D_R V_R$. The result of the calculation is stored in slot $n_\tau + 1$, and we recompute the Green function on time slice $(n_\tau + 1)\tau_1$. We can now proceed till we reach time slice β and we will have accumulated all the information required for carrying out a sweep from β to Δ_τ .

This completes a possible implementation of the finite-temperature method. The zero-temperature method follows exactly the same logic. However, it turns out that it is more efficient to keep track of $(P^\dagger B_s(2\Theta, 0)P)^{-1}$ since (i) it is of dimension $N_p \times N_p$ in contrast to the Green function which is a $N \times N$ matrix, and (ii) it is τ independent. When Green functions are required they are computed from scratch.

10.8 The Hirsch-Fye Impurity Algorithm

As its name suggests, this algorithm is triggered at solving impurity problems such as the Kondo and Anderson models. The strong point of the algorithm is that the CPU time is independent on the volume of the system thus allowing one to carry out simulations directly in the thermodynamic limit. The price however is a β^3 scaling of the CPU time where β is the inverse temperature. Diagrammatic determinantal methods, provide an alternative approach [8, 9] to solve impurity problems. Those algorithms are formulated in continuous time and hence do not suffer from Trotter errors. The computational effort equally scales as β^3 , but there is a prefactor which renders them more efficient. We will nevertheless concentrate here on the Hirsch-Fye algorithm since it is extensively used in the framework of dynamical mean-field theories [76, 77], see Chap. 16.

We will concentrate on the Anderson model defined as

$$H - \mu N = H_0 + H_U \quad (10.184)$$

with

$$\begin{aligned} H_0 &= \sum_{\mathbf{k}, \sigma} (\epsilon(\mathbf{k}) - \mu) c_{\mathbf{k}, \sigma}^\dagger c_{\mathbf{k}, \sigma} + \frac{V}{\sqrt{N}} \sum_{\mathbf{k}, \sigma} (c_{\mathbf{k}, \sigma}^\dagger f_\sigma + f_\sigma^\dagger c_{\mathbf{k}, \sigma}) \\ &\quad + \epsilon_f \sum_{\sigma} f_\sigma^\dagger f_\sigma, \\ H_U &= U(f_\uparrow^\dagger f_\uparrow - 1/2)(f_\downarrow^\dagger f_\downarrow - 1/2). \end{aligned} \quad (10.185)$$

For an extensive overview of the Anderson and related Kondo model, we refer the reader to [78].

In the next section, we will review the finite-temperature formalism. Since the CPU time scales as β^3 it is expensive to obtain ground state properties, and projective formulations of Hirsch-Fye algorithm become attractive. This corresponds to the topic of Sect. 10.8.2.

10.8.1 The Finite-Temperature Hirsch-Fye Method

In Sect. 10.6 we have shown that the grand-canonical partition function may be written as

$$Z \equiv \text{Tr} \left[e^{-\beta(H - \mu N)} \right] = \sum_{\mathbf{s}} \left[\prod_{\sigma} \det [1 + B_m^\sigma B_{m-1}^\sigma \dots B_1^\sigma] \right] \quad (10.186)$$

with $m\Delta_\tau = \beta$.

To define the matrices B_n^σ , we will label all the orbitals (conduction and impurity) with the index i and use the convention that $i = 0$ denotes the f -orbital and $i = 1 \dots N$ the conduction orbitals. We will furthermore define the fermionic operators

$$a_{i,\sigma}^\dagger = \begin{cases} f_\sigma^\dagger & \text{if } i = 0 \\ c_{i,\sigma}^\dagger & \text{otherwise} \end{cases}, \quad (10.187)$$

such that the non-interacting term of the Anderson takes the form

$$H_0 = \sum_\sigma H_0^\sigma, \quad H_0^\sigma = \sum_{i,j} a_{i,\sigma}^\dagger (h_0)_{i,j} a_{j,\sigma}. \quad (10.188)$$

Using the HS transformation of (10.235), the B matrices read

$$\begin{aligned} B_n^\sigma &= e^{V_n^\sigma} e^{-\Delta_\tau h_0}, \\ (V_n^\sigma)_{i,j} &= \delta_{i,j} \delta_{i,0} \alpha \sigma s_n, \\ \cosh(\alpha) &= e^{\Delta_\tau U/2}. \end{aligned} \quad (10.189)$$

The determinant in a given spin sector may be written as

$$\det [1 + B_m^\sigma B_{m-1}^\sigma \dots B_1^\sigma] = \det O^\sigma \quad (10.190)$$

with

$$O^\sigma = \begin{pmatrix} 1 & 0 & \cdot & \cdot & 0 & B_1^\sigma \\ -B_2^\sigma & 1 & 0 & \cdot & \cdot & 0 \\ 0 & -B_3^\sigma & 1 & \cdot & \cdot & 0 \\ \cdot & 0 & -B_4^\sigma & \cdot & \cdot & \cdot \\ \cdot & \cdot & 0 & \cdot & \cdot & \cdot \\ \cdot & \cdot & \cdot & \cdot & \cdot & \cdot \\ 0 & \cdot & \cdot & 0 & -B_m^\sigma & 1 \end{pmatrix}. \quad (10.191)$$

The above identity, follows by considering – omitting spin indices – the matrix $A = O - 1$. Since

$$\text{Tr}[A^n] = \sum_r \delta_{n,rm} (-1)^{r(m+1)} m \text{Tr}[(B_m \dots B_1)^r] \quad (10.192)$$

we obtain:

$$\begin{aligned} \det O &= e^{\text{Tr} \ln(1+A)} = e^{\sum_{n=1}^\infty \frac{(-1)^{n+1}}{n} \text{Tr}[A^n]} \\ &= e^{\sum_{r=1}^\infty \frac{(-1)^{r+1}}{r} \text{Tr}[(B_m \dots B_1)^r]} \\ &= e^{\text{Tr} \ln(1+B_m \dots B_1)} = \det(1 + B_m \dots B_1). \end{aligned} \quad (10.193)$$

From (10.128) we identify

$$(O^\sigma)^{-1} \equiv g^\sigma = \begin{pmatrix} G^\sigma(1,1) & G^\sigma(1,2) & \dots & G^\sigma(1,m) \\ G^\sigma(2,1) & G^\sigma(2,2) & \dots & G^\sigma(2,m) \\ \vdots & \vdots & \dots & \vdots \\ G^\sigma(m,1) & G^\sigma(m,2) & \dots & G^\sigma(m,m) \end{pmatrix}, \quad (10.194)$$

where $G^\sigma(n_1, n_2)$ are the time displaced Green functions

$$[G^\sigma(n_1, n_2)]_{i,j} = \begin{cases} \frac{\text{Tr}[B_m^\sigma \dots B_{n_1+1}^{a_{i,\sigma}} B_{n_1}^\sigma \dots B_{n_2+1}^{a_{j,\sigma}^\dagger} B_{n_2}^\sigma \dots B_1^\sigma]}{\text{Tr}[B_m^\sigma \dots B_1^\sigma]} & \text{if } n_1 \geq n_2 \\ -\frac{\text{Tr}[B_m^\sigma \dots B_{n_2+1}^{a_{j,\sigma}^\dagger} B_{n_2}^\sigma \dots B_{n_1+1}^{a_{i,\sigma}} B_{n_1}^\sigma \dots B_1^\sigma]}{\text{Tr}[B_m^\sigma \dots B_1^\sigma]} & \text{if } n_1 < n_2 \end{cases} \quad (10.195)$$

(see (10.124) and (10.125)). The operators B_n^σ are given by

$$B_n^\sigma = e^{\alpha \sigma s_n f_\sigma^\dagger f_\sigma} e^{-\Delta_\tau H_0^\sigma} . \quad (10.196)$$

Given an HS configuration s and s' and associated matrices

$$V^\sigma = \begin{pmatrix} V_1^\sigma & 0 & \dots & \dots & 0 \\ 0 & V_2^\sigma & 0 & \dots & 0 \\ 0 & 0 & V_3^\sigma & 0 & \dots \\ \vdots & \vdots & \vdots & \vdots & \vdots \\ 0 & \dots & \dots & \dots & 0 & V_m^\sigma \end{pmatrix} \quad (10.197)$$

and V'^σ the Green functions g^σ and g'^σ satisfy the following Dyson equation

$$g^\sigma = g'^\sigma + g'^\sigma \Delta (1 - g^\sigma) \quad \text{with } \Delta^\sigma = (e^{V'^\sigma} e^{-V^\sigma} - 1) . \quad (10.198)$$

To demonstrate the above, we consider

$$\begin{aligned} \tilde{O}^\sigma &= e^{-V^\sigma} O^\sigma \\ &= \begin{pmatrix} e^{-V_1^\sigma} & 0 & \dots & \dots & 0 & e^{-\Delta_\tau h_0} \\ -e^{-\Delta_\tau h_0} & e^{-V_2^\sigma} & 0 & \dots & \dots & 0 \\ 0 & -e^{-\Delta_\tau h_0} & e^{-V_3^\sigma} & \dots & \dots & 0 \\ \vdots & \vdots & -e^{-\Delta_\tau h_0} & \dots & \dots & \vdots \\ \vdots & \vdots & \vdots & \dots & \dots & \vdots \\ 0 & \vdots & \vdots & \dots & 0 & -e^{-\Delta_\tau h_0} & e^{-V_m^\sigma} \end{pmatrix} , \end{aligned} \quad (10.199)$$

so that (omitting the spin index σ)

$$\tilde{g} \equiv \tilde{O}^{-1} = [\tilde{O}' + \underbrace{\tilde{O} - \tilde{O}'}_{\equiv e^{-V} - e^{-V'}}]^{-1} = \tilde{g}' - \tilde{g}' (e^{-V} - e^{-V'}) \tilde{g} . \quad (10.200)$$

The above equation follows from the identity

$$\frac{1}{(A+B)} = \frac{1}{A} - \frac{1}{A} B \frac{1}{A+B} . \quad (10.201)$$

Substitution, $\tilde{g} = g \exp(V)$, leads to the Dyson equation (10.198).

The above Dyson equation is the central identity in the Hirsch-Fye algorithm: All quantities required for the algorithm may be derived directly from this equality. An implementation of the algorithm involves two steps:

10.8.1.0.1 Calculation of the impurity Green function for a given HS configuration

The starting point of the algorithm is to compute the green function for a random HS configuration of Ising spins s' . We will only need the Green function for the impurity f -site. Let $x = (\tau_x, \dot{i}_x)$ with Trotter index τ_x and orbital \dot{i}_x . Since

$$(e^{V'} e^{-V} - 1)_{x,y} = (e^{V'} e^{-V} - 1)_{x,x} \delta_{x,y} \delta_{\dot{i}_x,0} \quad (10.202)$$

we can use the Dyson equation only for the impurity Green function

$$g_{f,f'}^\sigma = g_{f,f'}^{I,\sigma} + \sum_{f''} g_{f,f''}^{I,\sigma} \Delta_{f'',f'}^\sigma (1 - g^\sigma)_{f'',f'} \quad (10.203)$$

with indices $f \equiv (\tau, 0)$ running from $1 \dots m$. Hence, the $m \times m$ impurity Green function matrix,

$$g_{f,f'}^{I,\sigma} = g_{f,f'}^\sigma \quad (10.204)$$

satisfies the Dyson equation

$$g^{I,\sigma} = g^{I,\sigma} + g^{I,\sigma} \Delta^{I,\sigma} (1 - g^{I,\sigma}) \quad \text{with} \quad \Delta_{f,f'}^{I,\sigma} = \Delta_{f,f'}^\sigma. \quad (10.205)$$

For $V = 0$, g^I is nothing but the impurity Green function of the non-interacting Anderson model which may readily be computed. Thus using the Dyson equation, we can compute the Green function $g^{I,\sigma}$ for an arbitrary HS configuration s' at the cost of an $m \times m$ matrix inversion. This involves a CPU cost scaling as m^3 or equivalently β^3 .

10.8.1.0.2 Upgrading

At this point we have computed the impurity Green function for a given HS configuration s . Adopting a single spin flip algorithm we will propose the configuration

$$s'_f = \begin{cases} -s_f & \text{if } f = f_1 \\ s_f & \text{otherwise} \end{cases} \quad (10.206)$$

and accept it with probability

$$R = \prod_{\sigma} R^\sigma \quad (10.207)$$

with

$$\begin{aligned} R^\sigma &= \frac{\det [1 + B_m^{I,\sigma} B_{m-1}^{I,\sigma} \dots B_1^{I,\sigma}]}{\det [1 + B_m^\sigma B_{m-1}^\sigma \dots B_1^\sigma]} = \det [g^\sigma (g^{I,\sigma})^{-1}] \\ &= \det [1 + \Delta^\sigma (1 - g^\sigma)] . \end{aligned} \quad (10.208)$$

The last identity follows from the Dyson equation to express g^σ as $g^\sigma = g'^\sigma [1 + \Delta^\sigma (1 - g^\sigma)]$. Since s and s' differ only by one entry the matrix Δ^σ has one non-zero matrix element: Δ_{f_1, f_1}^σ . Hence, $R^\sigma = 1 + \Delta_{f_1, f_1}^\sigma (1 - g_{f_1, f_1}^\sigma)$. Since the impurity Green function $g^{I, \sigma}$ is at hand, we can readily compute R .

If the move (spin flip) is accepted, we will have to recalculate (upgrade) the impurity Green function. From the Dyson equation (10.205), we have

$$g^{I, \sigma} = g^{I, \sigma} [1 + \Delta^{I, \sigma} (1 - g^{I, \sigma})]^{-1}. \quad (10.209)$$

To compute $[1 + \Delta^{I, \sigma} (1 - g^{I, \sigma})]^{-1}$ we can use the Sherman-Morrison formula of (10.163). Setting $A = 1$, $\mathbf{u}_f = \Delta_{f_1, f_1}^{I, \sigma} \delta_{f_1, f}$ and $\mathbf{v}_f = (1 - g^{I, \sigma})_{f_1, f}$ we obtain

$$g_{f, f'}^{I, \sigma} = g_{f, f'}^{I, \sigma} + \frac{g_{f, f_1}^{I, \sigma} \Delta_{f_1, f_1}^\sigma (g^{I, \sigma} - 1)_{f_1, f'}}{1 + (1 - g^{I, \sigma})_{f_1, f_1} \Delta_{f_1, f_1}^\sigma}. \quad (10.210)$$

Thus, the upgrading of the Green function under a single spin flip is an operation which scales as m^2 . Since for a single sweep we have to visit all spins, the computational cost of a single sweep scales as m^3 .

By construction, the Hirsch-Fye algorithm is free from numerical stabilization problems. For the here considered Anderson model, it has recently been shown that there is no sign problem irrespective of the conduction band electron density [79]. Clearly the attractive feature of the Hirsch-Fye impurity algorithm is that the algorithm may be formulated directly in the thermodynamic limit. This is not possible within the lattice formulation of the auxiliary field QMC method. Within this approach the dimension of the matrices scale as the total number of orbitals N , and the CPU time for a single sweep as $N^3 \beta$. The Hirsch-Fye algorithm is not limited to impurity models. However, when applied to lattice models, such as the Hubbard model, it is not efficient since the CPU time will scale as $(\beta N)^3$.

To conclude this section we show a typical example of the use of the Hirsch-Fye algorithm for the Kondo model

$$H = \sum_{\mathbf{k}, \sigma} \varepsilon(\mathbf{k}) c_{\mathbf{k}, \sigma}^\dagger c_{\mathbf{k}, \sigma} + J \mathbf{S}_c^I \cdot \mathbf{S}_f^I. \quad (10.211)$$

For the Monte Carlo formulation, the same ideas as for the lattice problem may be used for the HS decoupling of the interaction as well as to impose the constraint of no charge fluctuations on the f -sites. Figure 10.18 plots the impurity spin susceptibility

$$\chi^I = \int_0^\beta d\tau \langle \mathbf{S}_f^I(\tau) \cdot \mathbf{S}_f^I \rangle \quad (10.212)$$

for various values of J/t for a half-filled conduction band. As apparent, at low energies the data collapse to the universal form $\chi^I = f(T/T_K^I)/T$ where T_K^I is the Kondo temperature [78].

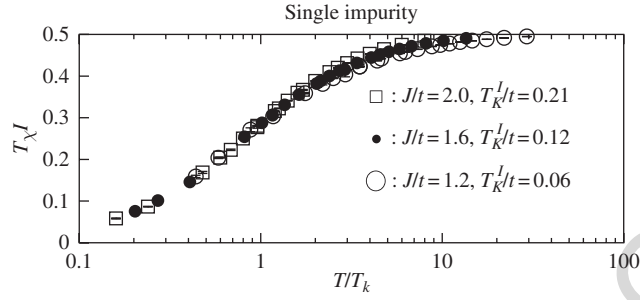


Fig. 10.18. Impurity spin susceptibility of the Kondo model as computed with the Hirsch-Fye impurity algorithm [80]

10.8.2 Ground-State Formulation

In the above finite-temperature formulation of the Hirsch-Fye algorithm, the CPU time scales as β^3 thus rendering it hard to reach the low temperature limit. Here we show how to formulate a projector version of the Hirsch-Fye algorithm. Although the CPU time will still scale as β^3 a good choice of the trial wave function may provide quicker convergence to the ground state than the finite temperature algorithm.

In the projector approach, the trial wave function $|\Psi_T\rangle$ is required to be a Slater determinant non-orthogonal to the ground state wave function. Hence, we can find an one body Hamiltonian

$$H_T = \sum_{i,j,\sigma} a_{i,\sigma}^\dagger (h_T)_{i,j} a_{j,\sigma}, \quad (10.213)$$

which has $|\Psi_T\rangle$ as a non-degenerate ground state. In the above, and in the context of the Anderson model, $a_{j,\sigma}$ denotes c - or f -fermionic operators. Our aim is to compute

$$\frac{\langle \Psi_T | e^{-\frac{\Theta}{2} H} O e^{-\frac{\Theta}{2} H} | \Psi_T \rangle}{\langle \Psi_T | e^{-\Theta H} | \Psi_T \rangle} \equiv \lim_{\beta \rightarrow \infty} \frac{\text{Tr} \left[e^{-\frac{\Theta}{2} H} O e^{-\frac{\Theta}{2} H} e^{-\beta H_T} \right]}{\text{Tr} \left[e^{-\Theta H} e^{-\beta H_T} \right]} \quad (10.214)$$

and subsequently take the limit $\Theta \rightarrow \infty$. As apparent, the above equation provides a link between the finite temperature and projection approaches. To proceed, we will consider the right hand side of the above equation and retrace the steps carried out for the standard finite-temperature formulation of the Hirsch-Fye algorithm. After Trotter decomposition and discrete Hubbard Stratonovich transformation we obtain

$$\langle \Psi_T | e^{-\Theta H} | \Psi_T \rangle = \lim_{\beta \rightarrow \infty} \sum_s \left[\prod_{\sigma} \det \left[1 + B_m^\sigma B_{m-1}^\sigma \dots B_1^\sigma e^{-\beta h_T} \right] \right] \quad (10.215)$$

with $m\Delta_\tau = \Theta$. Replacing B_1^σ by $B_1^\sigma \exp(-\beta h_T)$ in (10.191) and following the steps described for the finite-temperature version, we derive a Dyson equation (omitting spin indices) for the ground-state Green function matrix g_0

$$g_0^\sigma = g_0^{\prime\sigma} + g_0^{\prime\sigma} \Delta(1 - g_0^\sigma), \quad \Delta^\sigma = (e^{V'\sigma} e^{-V^\sigma} - 1), \quad (10.216)$$

with

$$g_0 = \begin{pmatrix} G_0(1,1) & G_0(1,2) & \dots & G_0(1,m) \\ G_0(2,1) & G_0(2,2) & \dots & G_0(2,m) \\ \vdots & \vdots & \ddots & \vdots \\ G_0(m,1) & G_0(m,2) & \dots & G_0(m,m) \end{pmatrix} \quad (10.217)$$

and

$$\begin{aligned} & [G_0(n_1, n_2)]_{i,j} \\ &= \lim_{\beta \rightarrow \infty} \begin{cases} \frac{\text{Tr}[B_m \dots B_{n_1+1} a_{i,\sigma} B_{n_1} \dots B_{n_2+1} a_{j,\sigma}^\dagger B_{n_2} \dots B_1 e^{-\beta H_T}]}{\text{Tr}[B_m \dots B_1 e^{-\beta H_T}]} & \text{if } n_1 \geq n_2 \\ -\frac{\text{Tr}[B_m \dots B_{n_2+1} a_{j,\sigma}^\dagger B_{n_2} \dots B_{n_1+1} a_{i,\sigma} B_{n_1} \dots B_1 e^{-\beta H_T}]}{\text{Tr}[B_m \dots B_1 e^{-\beta H_T}]} & \text{if } n_1 < n_2 \end{cases} \\ &= \begin{cases} \frac{\langle \Psi_T | B_m \dots B_{n_1+1} a_{i,\sigma} B_{n_1} \dots B_{n_2+1} a_{j,\sigma}^\dagger B_{n_2} \dots B_1 | \Psi_T \rangle}{\langle \Psi_T | B_m \dots B_1 | \Psi_T \rangle} & \text{if } n_1 \geq n_2 \\ -\frac{\langle \Psi_T | B_m \dots B_{n_2+1} a_{j,\sigma}^\dagger B_{n_2} \dots B_{n_1+1} a_{i,\sigma} B_{n_1} \dots B_1 | \Psi_T \rangle}{\langle \Psi_T | B_m \dots B_1 | \Psi_T \rangle} & \text{if } n_1 < n_2 \end{cases} \end{aligned} \quad (10.218)$$

As shown for the finite-temperature formulation, the simulation is entirely based on the Dyson equation. Since this equation also holds for the zero-temperature formulation precisely the same algorithm as in the finite-temperature case can be used.

In Fig. 10.19 we compare both algorithms and consider the double occupancy on the impurity site. As apparent, the ground-state formulation converges more quickly to the ground-state expectation value than the finite-temperature formulation.

The projector formulation of the Hirsch-Fye algorithm has been efficiently incorporated in the DMFT self-consistent cycle thus offering a route to compute $T = 0$ quantities within this framework [81]. Finally we note that diagrammatic determinantal methods can be extended very easily to projective schemes [82].

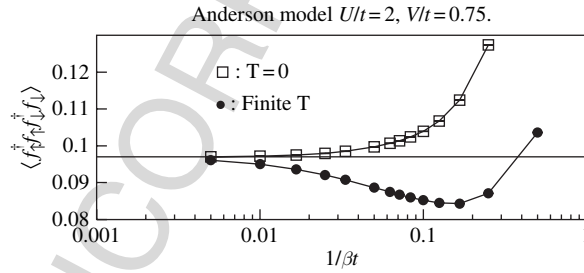


Fig. 10.19. Comparison between the zero and finite-temperature Hirsch-Fye algorithms for the symmetric Anderson model, with an 1D density of states

10.9 Selected Applications of the Auxiliary Field Method

The applications of the auxiliary field algorithms to correlated electron systems are numerous. Here we will only mention a few.

Let us start with the attractive Hubbard model. This model essentially describes the electron-phonon problem in terms of the Holstein model which in the anti-adiabatic limit maps onto the attractive Hubbard model [83]. Both models are free of sign problems in arbitrary dimensions and on arbitrary lattice topologies. The salient features of those models have been investigated in detail. For instance, the crossover from long coherence length (BCS) to short coherence length superconductors. In the short coherence length limit, a liquid of preformed pairs with non-Fermi liquid character is apparent above the transition temperature [84, 85]. Furthermore, the disorder driven superfluid to insulator transition has been studied in the framework of the attractive Hubbard model [86].

Recently, a new class of models of correlated electron models showing no sign problem has been investigated [69, 87, 88, 89]. Those models have exotic ground states including phases with circulating currents [56, 89], striped phases [87] as well as possible realizations of gapless spin liquid phases [56].

A lot of the work using the BSS algorithm is centered around the repulsive Hubbard model in two dimensions, as well as the three-band Hubbard model of the CuO_2 planes in the cuprates. On the basis of Monte Carlo simulations, it is now accepted that at half band-filling those models are Mott (charge transfer for the three-band model) insulators with long-range antiferromagnetic order [61, 90, 91]. In the case of the three band Hubbard model, a minimal set of parameters were found so as to reproduce experimental findings [92]. The issue of superconductivity at low doping away from half-filling is still open. General concepts – independent on the symmetry of the pair wave function and including possible retardation effects – such as flux quantization and superfluid density have been used to attempt to answer the above question [93, 94]. Within the algorithmic limitations, no convincing sign of superconductivity has been found to date.

The nature of the doping induced metal-insulator transition in the 2D Hubbard model, has attracted considerable interest [95, 96, 97]. In particular it has been argued that the transition is driven by the divergence of the effective mass rather than by the vanishing of the number of charge carriers. The origin of such a metal insulator transition is to be found in a very flat dispersion relation around the $(\pi, 0)$ and $(0, \pi)$ points in the Brillouin zone [98, 99]. An extensive review of this topic as well as a consistent interpretation of the numerical data in terms of a hyper-scaling Ansatz may be found in [100].

Aspects of the physics of heavy fermion systems have been investigated in the framework of the 2D periodic Anderson model (PAM) [101] and of the Kondo lattice model (KLM) [55]. It is only recently that a sign free formulation of the KLM for particle-hole symmetric conduction bands has been put forward [64]. Extensive calculations both at $T = 0$ and at finite T allow to investigate the magnetic order-disorder transition triggered by the competition between the RKKY interaction and the Kondo effect [55]. Across this quantum phase transition single-hole dynamics

as well as spin excitations were investigated in detail. One can show numerically that the quasiparticle residue in the vicinity of $\mathbf{k} = (\pi, \pi)$ tracks the Kondo scale of the corresponding single impurity problem. This statement is valid both in the magnetically ordered and disordered phases [102]. This suggests that the coherence temperature tracks the Kondo scale. Furthermore, the effect of a magnetic field on the Kondo insulating state was investigated. For the particle-hole symmetric conduction band, results show a transition from the Kondo insulator to a canted antiferromagnet [103, 104]. Finally, models with regular depletion of localized spins can be investigated [80]. Within the framework of those models, the typical form of the resistivity versus temperature can be reproduced.

The most common application of the Hirsch-Fye algorithm is in the framework of dynamical mean-field theories [77] which map the Hubbard model onto an Anderson impurity problem supplemented by a self-consistency loop. At each iteration, the Hirsch-Fye algorithm is used to solve the impurity problem at finite temperature [76] or at $T = 0$ [81]. For this particular problem, many competing methods such as DMRG [105] and NRG [106] are available. In the dynamical mean-field approximation spatial fluctuations are frozen out. To reintroduce them, one has to generalize to cluster methods such as the dynamical cluster approximation (DCA) [107] or cellular-DMFT (CDMFT) [108]. Within those approaches, the complexity of the problem to solve at each iteration is that of an N -impurity Anderson model (N corresponds to the cluster size). Generalizations of DMRG and NRG to solve this problem are difficult. On the other hand, as a function of cluster size the sign problem in the Hirsch-Fye approach becomes more and more severe but is, in many instances, still tractable. It however proves to be one of the limiting factors in achieving large cluster sizes.

10.10 Conclusion

We have discussed in details a variety of algorithms which can broadly be classified as world-line based or determinantal algorithms. For fermionic models, such as the Hubbard model, the determinantal QMC algorithm should be employed because of the reduced sign problem in this formulation. For purely 1D fermion systems and for spin models the world-line algorithms are available, which have lower autocorrelations, and better scaling because of their almost linear scaling with system size, in contrast to the cubic scaling of the determinantal algorithms.

Appendix 10.A The Trotter Decomposition

Given a Hamiltonian of the form

$$H = H_1 + H_2 , \quad (10.219)$$

the Trotter decomposition states that the imaginary time propagator can be split into a product of infinitesimal time propagations such that

$$e^{-\beta H} = \lim_{\Delta\tau \rightarrow 0} [e^{-\Delta\tau H_1} e^{-\Delta\tau H_2}]^m, \quad (10.220)$$

where $m\Delta\tau = \beta$. For $[H_1, H_2] \neq 0$ and finite values of the time step $\Delta\tau$ this introduces a systematic error. In many QMC algorithms we will not take the limit $\Delta\tau \rightarrow 0$, and it is important to understand the order of the systematic error produced by the above decomposition⁴. A priori, it is of the order $\Delta\tau$. However, in many non-trivial cases, the prefactor of the error of order $\Delta\tau$ vanishes [109].

For a time step $\Delta\tau$

$$e^{-\Delta\tau(H_1+H_2)} = e^{-\Delta\tau H_1} e^{-\Delta\tau H_2} - \frac{\Delta\tau^2}{2} [H_1, H_2] + \mathcal{O}(\Delta\tau^3), \quad (10.221)$$

such that

$$e^{-\Delta\tau(H-\Delta\tau/2[H_1, H_2])} = e^{-\Delta\tau H_1} e^{-\Delta\tau H_2} + \mathcal{O}(\Delta\tau^3). \quad (10.222)$$

We can now exponentiate both sides of the former equation to the power m

$$e^{-\beta(H-\Delta\tau/2[H_1, H_2])} = [e^{-\Delta\tau H_1} e^{-\Delta\tau H_2}]^m + \mathcal{O}(\Delta\tau^2). \quad (10.223)$$

The systematic error is now of order $\Delta\tau^2$ since in the exponentiation, the systematic error of order $\Delta\tau^3$ occurs m times and $m\Delta\tau = \beta$.

To evaluate the left hand side of the above equation we use time dependent perturbation theory. Let $h = h_0 + h_1$, where h_1 is small in comparison to h_0 . The imaginary time propagation in the interacting picture reads

$$U_I(\tau) = e^{\tau h_0} e^{-\tau h} \quad (10.224)$$

such that

$$\begin{aligned} \frac{\partial}{\partial\tau} U_I(\tau) &= e^{\tau h_0} (h_0 - h) e^{-\tau h} = - \underbrace{e^{\tau h_0} h_1 e^{-\tau h_0}}_{\equiv h_1^I(\tau)} U_I(\tau) \\ &= -h_1^I(\tau) U_I(\tau). \end{aligned} \quad (10.225)$$

Since $U_I(0) = 1$ we can transform the differential equation to an integral one

$$U_I(\tau) = 1 - \int_0^\tau d\tau' h_1^I(\tau') U_I(\tau') = 1 - \int_0^\tau d\tau' h_1^I(\tau') + \mathcal{O}(h_1^2). \quad (10.226)$$

Returning to (10.223) we can set $h_0 = H$, $h_1 = -\Delta\tau [H_1, H_2] / 2$ and $\tau = \beta$ to obtain

$$\begin{aligned} (e^{-\Delta\tau H_1} e^{-\Delta\tau H_2})^m &= e^{-\beta(H-\Delta\tau[H_1, H_2]/2)} + \mathcal{O}(\Delta\tau^2) \\ &= e^{-\beta H} + \underbrace{\frac{\Delta\tau}{2} \int_0^\beta d\tau e^{-(\beta-\tau)H} [H_1, H_2] e^{-\tau H}}_{\equiv A} + \mathcal{O}(\Delta\tau^2). \end{aligned} \quad (10.227)$$

⁴ For cases where a continuous time formulation is possible see Sect. 10.3.

In the QMC approaches with finite time steps we will compute:

$$\frac{\text{Tr}[(e^{-\Delta\tau H_1} e^{-\Delta\tau H_2})^m O]}{\text{Tr}[(e^{-\Delta\tau H_1} e^{-\Delta\tau H_2})^m]} = \frac{\text{Tr}[e^{-\beta H} O] + \frac{\Delta\tau}{2} \text{Tr}[AO]}{\text{Tr}[e^{-\beta H}] + \frac{\Delta\tau}{2} \text{Tr}[A]} + O(\Delta\tau^2), \quad (10.228)$$

where $O = O^\dagger$ is an observable. We now show that A is an anti-Hermitian operator

$$\begin{aligned} A^\dagger &= - \int_0^\beta d\tau e^{-\tau H} [H_1, H_2] e^{-(\beta-\tau)H} \\ &= \int_\beta^0 d\tau' e^{-(\beta-\tau')H} [H_1, H_2] e^{-\tau'H} = -A, \end{aligned} \quad (10.229)$$

where we have carried out the substitution $\tau' = \beta - \tau$. Since A is an anti-Hermitian operator it follows that $\overline{\text{Tr}[A]} = \text{Tr}[A^\dagger] = -\text{Tr}[A]$ as well as $\overline{\text{Tr}[AO]} = -\text{Tr}[AO]$. Recall that the observable O is a Hermitian operator. Thus, if O , H_1 and H_2 are simultaneously real representable in a given basis, the systematic error proportional to $\Delta\tau$ vanishes since in this case the trace is real. Hence the systematic error is of order $\Delta\tau^2$.

Clearly there are other choices of the Trotter decomposition which irrespective of the properties of H_1 , H_2 and O yield systematic errors of the order $\Delta\tau^2$. For example we mention the symmetric decomposition

$$e^{-\Delta\tau(H_1+H_2)} = e^{-\Delta\tau H_1/2} e^{-\Delta\tau H_1} e^{-\Delta\tau H_2/2} + O(\Delta\tau^3). \quad (10.230)$$

However, in many cases higher order decompositions are cumbersome and numerically expensive to implement.

Appendix 10.B The Hubbard-Stratonovich Decomposition

Auxiliary field QMC methods are based on various forms of the Hubbard-Stratonovich (HS) decomposition. This transformation is not unique. The efficiency of the algorithm as well as of the sampling scheme depends substantially on the type of HS transformation one uses. In this appendix we will review some aspects of the HS transformation with emphasis on its application to the auxiliary field QMC method.

The generic HS transformation is based on the Gaussian integral

$$\int_{-\infty}^{+\infty} d\phi e^{-(\phi+A)^2/2} = \sqrt{2\pi}, \quad (10.231)$$

which may be rewritten as

$$e^{A^2/2} = \frac{1}{\sqrt{2\pi}} \int_{-\infty}^{+\infty} d\phi e^{-\phi^2/2 - \phi A}. \quad (10.232)$$

Hence, if A is a one-body operator, the two-body operator $\exp(A^2/2)$, can be transformed into the integral of single-body operators interacting with a bosonic field ϕ . The importance of this identity in the Monte Carlo approach lies in the fact that for a fixed field ϕ the one-body problem is exactly solvable. The integral over the field ϕ can then be carried out with Monte Carlo methods. However, the Monte Carlo integration over a continuous field is much more cumbersome than the sum over a discrete field.

Let us consider for example the Hubbard interaction for a single site

$$H_U = U(n_\uparrow - \frac{1}{2})(n_\downarrow - \frac{1}{2}). \quad (10.233)$$

Here, $n_\sigma = c_\sigma^\dagger c_\sigma$ where c_σ^\dagger are spin 1/2 fermionic operators. In the Monte Carlo approach after Trotter decomposition of the kinetic and interaction term, we will have to compute $\exp(-\Delta\tau H_U)$. Since,

$$H_U = -\frac{U}{2} (n_\uparrow - n_\downarrow)^2 + \frac{U}{4} \quad (10.234)$$

we can set $A^2 = \Delta\tau U (n_\uparrow - n_\downarrow)^2$ and use (10.232) to compute $\exp(-\Delta\tau H_U)$. There are, however, more efficient ways of carrying out the transformation which are based on the fact that the Hilbert space for a single site consists of four states $|0\rangle, |\uparrow\rangle, |\downarrow\rangle$ and $|\uparrow, \downarrow\rangle$. Let us propose the identity

$$e^{-\Delta\tau H_U} = \gamma \sum_{s=\pm 1} e^{\alpha s (n_\uparrow - n_\downarrow)} \quad (10.235)$$

and see if it is possible to find values of α and γ to satisfy it on the single site Hilbert space. Applying each state vector on both sides of the equation yields

$$\begin{aligned} e^{-\Delta\tau U/4} |0\rangle &= 2\gamma |0\rangle \\ e^{-\Delta\tau U/4} |\uparrow\downarrow\rangle &= 2\gamma |\uparrow\downarrow\rangle \\ e^{\Delta\tau U/4} |\uparrow\rangle &= 2\gamma \cosh(\alpha) |\uparrow\rangle \\ e^{\Delta\tau U/4} |\downarrow\rangle &= 2\gamma \cosh(\alpha) |\downarrow\rangle. \end{aligned} \quad (10.236)$$

Hence (10.235) is satisfied provided that

$$\begin{aligned} \gamma &= \frac{1}{2} e^{-\Delta\tau U/4}, \\ \cosh(\alpha) &= e^{\Delta\tau U/2}. \end{aligned} \quad (10.237)$$

This choice of HS transformation leads to an efficient Monte Carlo algorithm for Hubbard type models. However, as apparent it breaks $SU(2)$ spin symmetry. Since

the HS field s couples to the z -component of the magnetization the spin symmetry is broken for a fixed value of the field and is restored only after summation over the field. To avoid this symmetry breaking, one can consider alternative HS transformations which couple to the density. In the same manner as above, we can show that

$$e^{-\Delta\tau H_U} = \tilde{\gamma} \sum_{s=\pm 1} e^{i\tilde{\alpha}s(n_\uparrow+n_\downarrow-1)}, \quad (10.238)$$

where $\cos(\tilde{\alpha}) = \exp(-\Delta\tau U/2)$ and $\tilde{\gamma} = \exp(\Delta\tau U/4)/2$. Clearly, this choice of the HS transformation conserves the $SU(2)$ spin symmetry for each realization of the field. However, this comes at the price that one needs to work with complex numbers. It turns out that when the sign problem is absent, the above choice of the HS transformation yields in general more efficient codes.

We conclude this appendix with a general discrete HS transformation which replaces (10.232). For small time steps $\Delta\tau$ we have the identity

$$e^{\Delta\tau\lambda A^2} = \sum_{l=\pm 1, \pm 2} \gamma(l) e^{\sqrt{\Delta\tau\lambda}\eta(l)O} + \mathcal{O}(\Delta\tau^4), \quad (10.239)$$

where the fields η and γ take the values

$$\begin{aligned} \gamma(\pm 1) &= 1 + \sqrt{6}/3, \\ \gamma(\pm 2) &= 1 - \sqrt{6}/3, \\ \eta(\pm 1) &= \pm\sqrt{2(3 - \sqrt{6})}, \\ \eta(\pm 2) &= \pm\sqrt{2(3 + \sqrt{6})}. \end{aligned} \quad (10.240)$$

This transformation is not exact and produces an overall systematic error proportional to $\Delta\tau^3$ in the Monte Carlo estimate of an observable. However, since we already have a systematic error proportional to $\Delta\tau^2$ from the Trotter decomposition, the transformation is as good as exact. It also has the great advantage of being discrete thus allowing efficient sampling.

Appendix 10.C Slater Determinants and their Properties

In this appendix, we review the properties of Slater determinants required for the formulation of auxiliary field QMC algorithms. Consider a single-particle Hamiltonian of the form

$$H_0 = \sum_{x,y} c_x^\dagger [h_0]_{x,y} c_y, \quad (10.241)$$

where h_0 is a Hermitian matrix, $\{c_x^\dagger, c_y\} = \delta_{x,y}$, $\{c_x^\dagger, c_y^\dagger\} = 0$, and x runs over the N_s single-particle states. Since h_0 is Hermitian, we can find an unitary matrix U such that $U^\dagger h_0 U = \lambda$, where λ is a diagonal matrix. Hence,

$$\begin{aligned}
H_0 &= \sum_x \lambda_{x,x} \gamma_x^\dagger \gamma_x, \\
\gamma_x &= \sum_y U_{x,y}^\dagger c_y, \\
\gamma_x^\dagger &= \sum_y c_y^\dagger U_{y,x}.
\end{aligned} \tag{10.242}$$

Since U is an unitary transformation the γ operators satisfy the commutation relations $\{\gamma_x^\dagger, \gamma_y\} = \delta_{x,y}$, and $\{\gamma_x^\dagger, \gamma_y^\dagger\} = 0$. An N_p -particle eigenstate of the Hamiltonian H_0 is characterized by the occupation of N_p single-particle levels, $\alpha_1 \dots \alpha_{N_p}$ and is given by

$$\gamma_{\alpha_1}^\dagger \gamma_{\alpha_2}^\dagger \dots \gamma_{\alpha_{N_p}}^\dagger |0\rangle = \prod_{n=1}^{N_p} \left(\sum_x c_x^\dagger U_{x,\alpha_n} \right) |0\rangle = \prod_{n=1}^{N_p} (c^\dagger P)_n |0\rangle. \tag{10.243}$$

In the last equation P denotes an rectangular matrix with N_s rows and N_p columns. The last equation defines the Slater determinant. The Slater determinant is a solution of a single-particle Hamiltonian, and is completely characterized by the rectangular matrix P .

We will now concentrate on the properties of Slater determinants. The first important property is that

$$e^{c^\dagger T c} \prod_{n=1}^{N_p} (c^\dagger P)_n |0\rangle = \prod_{n=1}^{N_p} (c^\dagger e^T P)_n |0\rangle. \tag{10.244}$$

The propagation of a Slater determinant with a single-particle propagator $\exp[c^\dagger T c]$ is a Slater determinant. We will show the above under the assumption that T is a Hermitian or anti-Hermitian matrix. It is useful to go into a basis where T is diagonal $U^\dagger T U = \lambda$. U is an unitary matrix and λ a real (purely imaginary) diagonal matrix provided that T is Hermitian (anti-Hermitian). Thus we can define the fermionic operators $\gamma^\dagger = c^\dagger U$ to obtain

$$\begin{aligned}
e^{c^\dagger T c} \prod_{n=1}^{N_p} (c^\dagger P)_n |0\rangle &= e^{\gamma^\dagger \lambda \gamma} \prod_{n=1}^{N_p} (\gamma^\dagger U P)_n |0\rangle \\
&= \sum_{y_1, \dots, y_{N_p}} e^{\sum_x \lambda_{x,x} \gamma_x^\dagger \gamma_x} \gamma_{y_1}^\dagger \dots \gamma_{y_{N_p}}^\dagger |0\rangle (UP)_{y_1,1} \dots (UP)_{y_{N_p},N_p} \\
&= \sum_{y_1, \dots, y_{N_p}} e^{\lambda_{y_1,y_1} \gamma_{y_1}^\dagger \dots \lambda_{y_{N_p},y_{N_p}} \gamma_{y_{N_p}}^\dagger} |0\rangle (UP)_{y_1,1} \dots (UP)_{y_{N_p},N_p} \\
&= \prod_{n=1}^{N_p} (\gamma^\dagger e^\lambda U P)_n |0\rangle = \prod_{n=1}^{N_p} (c^\dagger U^\dagger e^\lambda U P)_n |0\rangle = \prod_{n=1}^{N_p} (c^\dagger e^T P)_n |0\rangle.
\end{aligned} \tag{10.245}$$

The second property we will need, is the overlap of two slater determinants. Let

$$\begin{aligned} |\Psi\rangle &= \prod_{n=1}^{N_p} (\mathbf{c}^\dagger P)_n |0\rangle, \\ |\tilde{\Psi}\rangle &= \prod_{n=1}^{N_p} (\mathbf{c}^\dagger \tilde{P})_n |0\rangle, \end{aligned} \quad (10.246)$$

then

$$\langle \Psi | \tilde{\Psi} \rangle = \det [P^\dagger \tilde{P}]. \quad (10.247)$$

The above follows from

$$\begin{aligned} \langle \Psi | \tilde{\Psi} \rangle &= \langle 0 | \prod_{n=N_p}^1 (P^\dagger \mathbf{c})_n \prod_{\tilde{n}=1}^{N_p} (\mathbf{c}^\dagger \tilde{P})_{\tilde{n}} |0\rangle \\ &= \sum_{\substack{y_1, \dots, y_{N_p} \\ \tilde{y}_1, \dots, \tilde{y}_{N_p}}} P_{N_p, y_{N_p}}^\dagger \dots P_{1, y_1}^\dagger \tilde{P}_{\tilde{y}_1, 1} \dots \tilde{P}_{\tilde{y}_{N_p}, N_p} \langle 0 | c_{y_{N_p}}^\dagger \dots c_{y_1}^\dagger c_{\tilde{y}_1}^\dagger \dots c_{\tilde{y}_{N_p}}^\dagger |0\rangle. \end{aligned} \quad (10.248)$$

The matrix element in the above equation does not vanish provided that all the $y_i, i : 1 \dots N_p$ take different values and that there is a permutation π , of N_p numbers such that

$$\tilde{y}_i = y_{\pi(i)}. \quad (10.249)$$

Under those conditions, the matrix element is nothing but the sign of the permutation $(-1)^\pi$. Hence,

$$\begin{aligned} \langle \Psi | \tilde{\Psi} \rangle &= \sum_{y_1, \dots, y_{N_p}} |c_{y_1}^\dagger \dots c_{y_{N_p}}^\dagger |0\rangle|^2 \\ &\quad \times \sum_{\pi \in \mathcal{S}_{N_p}} (-1)^\pi P_{N_p, y_{N_p}}^\dagger \dots P_{1, y_1}^\dagger \tilde{P}_{y_{\pi(1)}, 1} \dots \tilde{P}_{y_{\pi(N_p)}, N_p}. \end{aligned} \quad (10.250)$$

In the above, we have explicitly included the matrix element $|c_{y_1}^\dagger \dots c_{y_{N_p}}^\dagger |0\rangle|^2$ to insure that terms in the sum with $y_i = y_j$ do not contribute since under this assumption the matrix element vanishes due to the Pauli principle. We can however omit this term since the sum over permutations will guarantee that if $y_i = y_j$ for any $i \neq j$ then $\sum_{\pi \in \mathcal{S}_{N_p}} (-1)^\pi P_{N_p, y_{N_p}}^\dagger \dots P_{1, y_1}^\dagger \tilde{P}_{y_{\pi(1)}, 1} \dots \tilde{P}_{y_{\pi(N_p)}, N_p}$ vanishes. Consider for example $N_p = 2$ and $y_1 = y_2 = x$ then the sum reduces to $P_{2,x}^\dagger P_{1,x}^\dagger \tilde{P}_{x,1} \tilde{P}_{x,2} \sum_{\pi \in \mathcal{S}_2} (-1)^\pi = 0$ since the sum over the sign of the permutations vanishes.

With the above observation

$$\begin{aligned}
 \langle \Psi | \tilde{\Psi} \rangle &= \sum_{\substack{y_1, \dots, y_{N_p} \\ \pi \in \mathcal{S}_{N_p}}} (-1)^\pi P_{N_p, y_{N_p}}^\dagger \dots P_{1, y_1}^\dagger \tilde{P}_{y_{\pi(1)}, 1} \dots \tilde{P}_{y_{\pi(N_p)}, N_p} \\
 &= \sum_{\substack{y_1, \dots, y_{N_p} \\ \pi \in \mathcal{S}_{N_p}}} (-1)^{\pi^{-1}} P_{N_p, y_{N_p}}^\dagger \dots P_{1, y_1}^\dagger \tilde{P}_{y_1, \pi^{-1}(1)} \dots \tilde{P}_{y_{N_p}, \pi^{-1}(N_p)} \\
 &= \sum_{\pi \in \mathcal{S}_{N_p}} (-1)^\pi \left(P^\dagger \tilde{P} \right)_{1, \pi(1)} \dots \left(P^\dagger \tilde{P} \right)_{N_p, \pi(N_p)} = \det \left[P^\dagger \tilde{P} \right].
 \end{aligned} \tag{10.251}$$

Finally, we will need to establish the relation

$$\text{Tr} \left[e^{c^\dagger T_1 c} e^{c^\dagger T_2 c} \dots e^{c^\dagger T_n c} \right] = \det \left[1 + e^{T_1} e^{T_2} \dots e^{T_n} \right], \tag{10.252}$$

where the trace is over the Fock space. To verify the validity of the above equation, let us set $B = e^{T_1} e^{T_2} \dots e^{T_n}$ and $U = e^{c^\dagger T_1 c} e^{c^\dagger T_2 c} \dots e^{c^\dagger T_n c}$.

$$\begin{aligned}
 &\det(1 + B) \\
 &= \sum_{\pi \in \mathcal{S}_{N_s}} (-1)^\pi (1 + B_{\pi(1), 1}) \dots (1 + B_{\pi(N_s), N_s}) \\
 &= \sum_{\pi \in \mathcal{S}_{N_s}} (-1)^\pi \delta_{1, \pi(1)} \dots \delta_{N_s, \pi(N_s)} \\
 &\quad + \sum_x \sum_{\pi \in \mathcal{S}_{N_s}} (-1)^\pi B_{\pi(x), x} \delta_{1, \pi(1)} \dots \widehat{\delta_{x, \pi(x)}} \dots \delta_{N_s, \pi(N_s)} \\
 &\quad + \sum_{y > x} \sum_{\pi \in \mathcal{S}_{N_s}} (-1)^\pi B_{\pi(x), x} B_{\pi(y), y} \\
 &\quad \quad \times \delta_{1, \pi(1)} \dots \widehat{\delta_{x, \pi(x)}} \dots \widehat{\delta_{y, \pi(y)}} \dots \delta_{N_s, \pi(N_s)} \\
 &\quad + \sum_{y > x > z} \sum_{\pi \in \mathcal{S}_{N_s}} (-1)^\pi B_{\pi(x), x} B_{\pi(y), y} B_{\pi(z), z} \\
 &\quad \quad \times \delta_{1, \pi(1)} \dots \widehat{\delta_{x, \pi(x)}} \dots \widehat{\delta_{y, \pi(y)}} \dots \widehat{\delta_{z, \pi(z)}} \dots \delta_{N_s, \pi(N_s)} + \dots \tag{10.253}
 \end{aligned}$$

Here, $\widehat{\delta_{y, \pi(y)}}$ means that this term is omitted in the product $\prod_{x=1}^{N_s} \delta_{x, \pi(x)}$. To proceed, let us consider in more details the second term starting with $\sum_{y > x}$ in the last equality. Due to the δ -functions the sum over the permutation of N_s numbers reduces to two terms, namely the unit permutation and the transposition $\pi(x) = x$ and $\pi(y) = y$. Let us define the $P^{(x, y)}$ as a rectangular matrix of dimension $N_s \times 2$, with entries of the first (second) column set to one at row x (y) and zero otherwise. Hence, we can write

$$\begin{aligned}
 &\sum_{\pi \in \mathcal{S}_{N_s}} (-1)^\pi B_{\pi(x), x} B_{\pi(y), y} \delta_{1, \pi(1)} \dots \widehat{\delta_{x, \pi(x)}} \dots \widehat{\delta_{y, \pi(y)}} \dots \delta_{N_s, \pi(N_s)} \\
 &= \det \left[P^{(x, y), \dagger} B P^{(x, y)} \right] = \langle 0 | c_x c_y U c_y^\dagger c_x^\dagger | 0 \rangle, \tag{10.254}
 \end{aligned}$$

where in the last equation we have used the properties of (10.247) and (10.244). Repeating the same argument for different terms we obtain

$$\begin{aligned} & \det(1 + B) \\ &= 1 + \sum_x \langle 0 | c_x U c_x^\dagger | 0 \rangle + \sum_{y>x} \langle 0 | c_x c_y U c_y^\dagger c_x^\dagger | 0 \rangle \\ &+ \sum_{y>x>z} \langle 0 | c_x c_y c_z U c_z^\dagger c_y^\dagger c_x^\dagger | 0 \rangle + \dots = \text{Tr}[U] . \end{aligned} \quad (10.255)$$

This concludes the demonstration of (10.252).

References

1. S.R. White, *Physics Reports* **301**, 187 (1998)
2. U. Schollwöck, *Rev. Mod. Phys.* **77**, 259 (2005)
3. H.G. Evertz, G. Lana, M. Marcu, *Phys. Rev. Lett.* **70**, 875 (1993)
4. H.G. Evertz, *Adv. Phys.* **52**, 1 (1997)
5. O. Syljuasen, A.W. Sandvik, *Phys. Rev. E* **66**, 046701 (2002)
6. R. Blankenbecler, D.J. Scalapino, R.L. Sugar, *Phys. Rev. D* **24**, 2278 (1981)
7. F. Michel, H. Evertz. In preparation
8. A.N. Rubtsov, V.V. Savkin, A.I. Lichtenstein, *Phys. Rev. B* **72**, 035122 (2005)
9. P. Werner, A. Comanac, L.D. Medici, M. Troyer, A. Millis, *Phys. Rev. Lett.* **97**, 076405 (2006)
10. J.E. Hirsch, D.J. Scalapino, R.L. Sugar, R. Blankenbecler, *Phys. Rev. B* **26**, 5033 (1981)
11. M. Barma, B.S. Shastry, *Phys. Rev. B* **18**, 3351 (1978)
12. R.J. Baxter, *Exactly Solved Models in Statistical Mechanics* (Academic Press Limited, London, 1989)
13. M. Troyer, M. Imada, K. Ueda, *J. Phys. Soc. Jpn.* **66**, 2957 (1997)
14. O. Syljuasen, *Phys. Rev. B* **67**, 046701 (2003)
15. A.W. Sandvik, O.F. Syljuåsen, in *THE MONTE CARLO METHOD IN THE PHYSICAL SCIENCES: Celebrating the 50th Anniversary of the Metropolis Algorithm*, *AIP Conference Proceedings*, Vol. 690, ed. by J.E. Gubernatis (2003), pp. 299–308. URL <http://arxiv.org/abs/cond-mat/0306542>
16. M. Troyer, F. Alet, S. Trebst, S. Wessel, in *THE MONTE CARLO METHOD IN THE PHYSICAL SCIENCES: Celebrating the 50th Anniversary of the Metropolis Algorithm*, *AIP Conference Proceedings*, Vol. 690, ed. by J.E. Gubernatis (2003), pp. 156–169. URL <http://arxiv.org/abs/physics/0306128>
17. N. Kawashima, K. Harada, *J. Phys. Soc. Jpn.* **73**, 1379 (2004)
18. J.F. Corney, P.D. Drummond, *Phys. Rev. Lett.* **93**, 260401 (2004)
19. F.F. Assaad, P. Werner, P. Corboz, E. Gull, M. Troyer, *Phys. Rev. B* **72**, 224518 (2005)
20. F.F. Assaad, D. Würtz, *Phys. Rev. B* **44**, 2681 (1991)
21. M. Troyer, F.F. Assaad, D. Würtz, *Helv. Phys. Acta.* **64**, 942 (1991)
22. M. Brunner, F.F. Assaad, A. Muramatsu, *Eur. Phys. J. B* **16**, 209 (2000)
23. M. Brunner, F.F. Assaad, A. Muramatsu, *Phys. Rev. B* **62**, 12395 (2000)
24. C. Brünner, F.F. Assaad, *Phys. Rev. B* **74**, 205107 (2006)
25. N. Prokof'ev, B. Svistunov, *Phys. Rev. Lett.* **81**, 2514 (1998)
26. S. Rombouts, K. Heide, N. Jachowicz, *Phys. Rev. Lett.* **82**, 4155 (1999)

27. E. Burovski, A. Mishchenko, N. Prokof'ev, B. Svistunov, Phys. Rev. Lett. **87**, 186402 (2001)
28. A. Rubtsov, M. Katsnelson, A. Lichtenstein, Dual fermion approach to nonlocal correlations in the hubbard model. URL <http://arxiv.org/abs/cond-mat/0612196>. Preprint
29. M. Boninsegni, N. Prokof'ev, B. Svistunov, Phys. Rev. Lett. **96**, 070601 (2006)
30. B. Beard, U. Wiese, Phys. Rev. Lett. **77**, 5130 (1996)
31. A. Sandvik, J. Kurkijärvi, Phys. Rev. B **43**, 5950 (1991)
32. A.W. Sandvik, J. Phys. A **25**, 3667 (1992)
33. A.W. Sandvik, Phys. Rev. B **56**, 11678 (1997)
34. N. Prokof'ev, B. Svistunov, I. Tupitsyn, Pis'ma Zh. Eks. Teo. Fiz. **64**, 853 (1996). URL <http://arxiv.org/abs/cond-mat/9612091>
35. N. Prokof'ev, B. Svistunov, I. Tupitsyn, Sov. Phys. JETP **87**, 310 (1998)
36. A. Sandvik, R. Singh, D. Campbell, Phys. Rev. B **56**, 14510 (1997)
37. A. Sandvik, D. Campbell, Phys. Rev. Lett. **83**, 195 (1999)
38. A. Dorneich, M. Troyer, Phys. Rev. E **64**, 066701 (2001)
39. P. Kasteleyn, C. Fortuin, J. Phys. Soc. Jpn. Suppl. **26**, 11 (1969)
40. C. Fortuin, P. Kasteleyn, Physica **57**, 536 (1972)
41. R. Swendsen, J. Wang, Phys. Rev. Lett. **58**, 86 (1987)
42. A.D. Sokal, in *Quantum Fields on the Computer*, ed. by M. Creutz (World Scientific, Singapore, 1992), pp. 211–274. Available electronically via www.dbwilson.com/exact
43. M. Aizenman, B. Nachtergaele, Comm. Math. Phys. **164**, 17 (1994)
44. B. Nachtergaele, in *Probability Theory and Mathematical Statistics (Proceedings of the 6th Vilnius Conference)*, ed. by B. Grigelionis, et al. (VSP/TEV, Utrecht Tokyo Vilnius, 1994), pp. 565–590. URL <http://arxiv.org/abs/cond-mat/9312012>
45. A.W. Sandvik, Phys. Rev. B **59**, R14157 (1999)
46. P. Henelius, A. Sandvik, Phys. Rev. B **62**, 1102 (2000)
47. A.W. Sandvik, Phys. Rev. Lett. **95**, 207203 (2005)
48. H. Evertz, W. von der Linden, Phys. Rev. Lett. **86**, 5164 (2001)
49. R. Citro, E. Orignac, T. Giamarchi, Phys. Rev. B **72**, 024434 (2005)
50. K. Hukushima, K. Nemoto, J. Phys. Soc. Japan **65**, 1604 (1996)
51. K. Hukushima, H. Takayama, K. Nemoto, Int. J. Mod. Phys. C **7**, 337 (1996)
52. E. Marinari, G. Parisi, Europhys. Lett. **19**, 451 (1992)
53. W. Barford, R. Bursill, Phys. Rev. Lett. **95**, 137207 (2005)
54. J.E. Hirsch, R.M. Fye, Phys. Rev. Lett. **56**, 2521 (1986)
55. S. Capponi, F.F. Assaad, Phys. Rev. B **63**, 155114 (2001)
56. F.F. Assaad, Phys. Rev. B **71**, 075103 (2005)
57. G. Sugiyama, S. Koonin, Ann. Phys. (N.Y.) **168**, 1 (1986)
58. S. Sorella, S. Baroni, R. Car, M. Parrinello, Europhys. Lett. **8**, 663 (1989)
59. S. Sorella, E. Tosatti, S. Baroni, R. Car, M. Parrinello, Int. J. Mod. Phys. B **1**, 993 (1989)
60. J.E. Hirsch, Phys. Rev. B **31**, 4403 (1985)
61. S.R. White, D.J. Scalapino, R.L. Sugar, E.Y. Loh, J.E. Gubernatis, R.T. Scalettar, Phys. Rev. B **40**, 506 (1989)
62. A.M. Tsvelik, *Quantum Field Theory in Condensed Matter Physics* (Cambridge University press, Cambridge, 1996)
63. F.F. Assaad, M. Imada, J. Phys. Soc. Jpn. **65**, 189 (1996)
64. F.F. Assaad, Phys. Rev. Lett. **83**, 796 (1999)
65. M. Jarréll, J. Gubernatis, Phys. Rep. **269**, 133 (1996)

66. W. von der Linden, *Appl. Phys. A* **60**, 155 (1995)
67. K.S.D. Beach, Identifying the maximum entropy method as a special limit of stochastic analytic continuation. URL <http://arxiv.org/abs/cond-mat/0403055>. Preprint
68. J.E. Hirsch, *Phys. Rev. B* **38**, 12023 (1988)
69. C. Wu, S. Zhang, *Phys. Rev. B* **71**, 155115 (2005)
70. A. Messiah, *Quantum Mechanics*. (Dover publications, INC., Mineola, New-York, 1999)
71. S. Capponi, F.F. Assaad, *Phys. Rev. B* **75**, 045115 (2007)
72. M. Troyer, U. Wiese, *Phys. Rev. Lett.* **94**, 170201 (2005)
73. J.F. Corney, P.D. Drummond, *J. Phys. A: Math. Gen.* **39**, 269 (2006)
74. W.H. Press, S.A. Teukolsky, W.T. Vetterling, B.P. Flannery, *Numerical Recipes in C* (Cambridge University Press, Cambridge, 1992)
75. M. Feldbacher, F.F. Assaad, *Phys. Rev. B* **63**, 073105 (2001)
76. M. Jarrell, *Phys. Rev. Lett.* **69**, 168 (1992)
77. A. Georges, G. Kotliar, W. Krauth, M.J. Rozenberg, *Rev. of. Mod. Phys.* **68**, 13 (1996)
78. A.C. Hewson, *The Kondo Problem to Heavy Fermions*. Cambridge Studies in Magnetism (Cambridge University Press, Cambridge, 1997)
79. J. Yoo, S. Chandrasekharan, R.K. Kaul, D. Ullmo, H.U. Baranger, *J. Phys. A: Math. Gen.* **38**, 10307 (2005)
80. F.F. Assaad, *Phys. Rev. B* **65**, 115104 (2002)
81. M. Feldbacher, F.F. Assaad, K. Held, *Phys. Rev. Lett.* **93**, 136405 (2004)
82. F.F. Assaad. In preparation
83. J.E. Hirsch, Fradkin, *Phys. Rev. B* **27**, 4302 (1983)
84. M. Randeria, N. Trivedi, A. Moreo, R.T. Scalettar, *Phys. Rev. Lett.* **69**, 2001 (1992)
85. N. Trivedi, M. Randeria, *Phys. Rev. Lett.* **75**, 312 (1995)
86. M. Randeria, N. Trivedi, A. Moreo, R.T. Scalettar, *Phys. Rev. D* **54**, R3756 (1996)
87. F.F. Assaad, V. Rousseau, F. Hébert, M. Feldbacher, G. Batrouni, *Europhys. Lett.* **63**, 569 (2003)
88. C. Wu, J.P. Hu, S.C. Zhang, *Phys. Rev. Lett.* **91**, 186402 (2003)
89. S. Capponi, C. Wu, S.C. Zhang, *Phys. Rev. B* **70**, 220505 (2004)
90. J.E. Hirsch, S. Tang, *Phys. Rev. Lett.* **62**, 591 (1989)
91. G. Dopf, A. Muramatsu, W. Hanke, *Europhys. Lett.* **17**, 559 (1992)
92. G. Dopf, A. Muramatsu, W. Hanke, *Phys. Rev. Lett.* **68**, 353 (1992)
93. F.F. Assaad, W. Hanke, D.J. Scalapino, *Phys. Rev. B* **50**, 12835 (1994)
94. D.J. Scalapino, S. White, S. Zhang, *Phys. Rev. B* **47**, 7995 (1993)
95. N. Furukawa, M. Imada, *J. Phys. Soc. Jpn.* **62**, 2557 (1993)
96. F.F. Assaad, M. Imada, *Phys. Rev. Lett* **74**, 3868 (1995)
97. F.F. Assaad, M. Imada, *Phys. Rev. Lett* **76**, 3176 (1996)
98. G. Dopf, J. Wagner, P. Dieterich, A. Muramatsu, W. Hanke, *Phys. Rev. Lett.* **68**, 2082 (1992)
99. C. Gröber, R. Eder, W. Hanke, *Phys. Rev. B* **62**, 4336 (2000)
100. M. Imada, A. Fujimori, Y. Tokura, *Rev. Mod. Phys.* **70**, 1039 (1998)
101. M. Vekic, J.W. Cannon, D.J. Scalapino, R.T. Scalettar, R.L. Sugar, *Phys. Rev. Lett.* **74**, 2367 (1995)
102. F.F. Assaad, *Phys. Rev. B* **70**, 020402 (2004)
103. I. Milat, F. Assaad, M. Sigrist, *Eur. Phys. J. B* **38**, 571 (2004)
104. K.S.D. Beach, P.A. Lee, P. Monthoux, *Phys. Rev. Lett.* **92**, 026401 (2004)

105. S. Nishimoto, F. Gebhard, E. Jeckelmann, *J. Phys.: Condens. Matter* **16**, 7063 (2004)
106. R. Bulla, *Phys. Rev. Lett.* **83**, 136 (1999)
107. M.M. M. H. Hettler, M. Jarrell, H.R. Krishnamurthy, *Phys. Rev. B* **61**, 12739 (2000)
108. G. Kotliar, S.Y. Savrasov, G. Pálsson, G. Biroli, *Phys. Rev. Lett.* **87**, 186401 (2001)
109. R.M. Fye, *Phys. Rev. B* **33**, 6271 (1986)

UNCORRECTED PROOF